Adaptive Sliding Mode Controls with Input-Linearization for Electrohydraulic Systems

Thesis Submitted by

Sibsankar Dasmahapatra

Doctor of Philosophy (Engineering)

DEPARTMENT OF MECHANICAL ENGINEERING
FACULTY COUNCIL OF ENGINEERING AND TECHNOLOGY
JADAVPUR UNIVERSITY
KOLKATA, INDIA

2019

JADAVPUR UNIVERSITY

KOLKATA – 700032, INDIA

INDEX NO. **120/15/E**

1. Title of the thesis:

Adaptive Sliding Mode Controls with Input-Linearization for Electrohydraulic Systems

2. Name, Designation & Institution of the Supervisors:

a. Prof. Dipankar Sanyal

Department of Mechanical Engineering,
Jadavpur University,
Kolkata- 700032, India.

b. Prof. Rana Saha

Department of Mechanical Engineering,
Jadavpur University,
Kolkata- 700032, India

3. List of Publications:

Journal Publications

I. **Dasmahapatra S**, Saha R, Mookherjee S and Sanyal D (2018) **Designing an Input-Linearized Adaptive Sliding Mode Coupled Nonlinear Integral Controller**. *IEEE/ASME Trans. Mechatronics* (23): 2888-2895.

II. **Dasmahapatra S**, Sarkar BK, Saha R, Chatterjee A, Mookherjee S and Sanyal D (2015) **Design of an adaptive-fuzzy-bias-SMC and validation for a rugged electrohydraulic system**. *IEEE/ASME Trans. Mechatronics* (20): 2708-2715.

Book Chapter publication

I. Chaudhuri S, **Dasmahapatra S**, Chatterjee A, Saha R, Mookherjee S and Sanyal D (2016) **Adaptive Fuzzy-Sliding Mode Control with Fixed Bias Compensator for an Electrohydraulic Actuation System with Hard Nonlinearities**. In: Saha AK, Das D, Srivastava R, Panigrahi PK and Muralidhar K (eds) *FMFP – Contemporary Research, Lecture Notes in Mechanical Engineering*. Delhi: Springer, pp. 1223-1232.

International Conference Publications

I. **Dasmahapatra S**, Saha R, Sanyal D, Sengupta A and Bhattacharyya U (2017) **Adaptive PID Control for Angular Motion Tracking by Linear Electrohydraulic Actuation**. In: *IEEE First International Conference on ICPEICES*, Delhi, India, 4-6 July 2016, pp. 1-5. IEEE Publishing.

II. **Dasmahapatra S**, Saha R, Sanyal D, Sengupta A, Bhattacharyya U and Sanyal S (2016) **Designing Low-Chattering Sliding Mode Controller for an Electrohydraulic System**. In: *IEEE First International Conference on CMI*, Jadavpur University, Kolkata, India, 8-10 January 2016, pp. 316-320. IEEE Publishing.

III. **Dasmahapatra S**, Saha D, Saha R, Sanyal D, Lahiri D and Singh JP (2016) **Analysis of 6-DOF motion with PI controller in electrohydraulic Stewart platform**. In: *IEEE First International Conference on CMI*, Jadavpur University, Kolkata, India, 8-10 January 2016, pp. 186-190. IEEE Publishing.

IV. **Dasmahapatra S**, Saha R, Sanyal D, Sengupta A and Sanyal S (2016) **Designing Sliding Mode with Integral Control for Angular Rotation of a Link by Linear Electrohydraulic Actuation**. In: *12th IEEE India International Conference of INDICON*, Jamia Milla Islamia, Delhi, India, 17-20 December 2015, pp. 1-5. IEEE Publishing.

4. List of Patents: Nil

5. List of Presentations in National/International/Conferences/Workshops:

I. **Dasmahapatra S**, Saha R, Sanyal D, Sengupta A and Sanyal S: **Designing Sliding Mode with Integral Control for Angular Rotation of a Link by Linear Electrohydraulic Actuation**. *12th IEEE India International Conference of INDICON*, Jamia Milla Islamia, New Delhi, India, 17-20 December 2015.

II. **Dasmahapatra S**, Mandal P, Saha R, Mookherjee S and Sanyal D: **Comparison of Fuzzy Control and Sliding Mode Control in Real-time tracking of rugged Electrohydraulic System**. *40th National Conference on FMFP*, NIT Hamirpur, Himachal Pradesh, India, 12-14 December 2013.

JADAVPUR UNIVERSITY
FACULTY COUNCIL OF ENGINEERING AND TECHNOLOGY

CERTIFICATE FROM THE SUPERVISORS

This to certify that the thesis entitled "**Adaptive Sliding Mode Controls with Input-Linearization for Electrohydraulic Systems**" submitted by **Shri. Sibsankar Dasmahapatra,** who got his name registered on 2nd July, 2015 for the award of Ph. D. (Engineering) degree of Jadavpur University is absolutely based upon his own work under the supervision of **Prof. Dipankar Sanyal** and **Prof. Rana Saha** and that neither his thesis nor any part of the theis has been submitted for any degree/diploma or any other academic award anywhere before.

1._____

(Prof. Dipankar Sanyal)

Signature of the supervisor
with date and seal

2._____

(Prof. Rana Saha)

Signature of the supervisor
with date and seal

To

Elder Sister (bardi)

Sumana Dasmahapatra (Das).....

ACKNOWLEDGEMENT

I would like to express my sincere gratitude to my supervisors **Prof. Dipankar Sanyal** and **Prof. Rana Saha,** Department of Mechanical Engineering, Jadavpur University, Kolkata for their valuable guidance, advice and encouragement throughout the duration of this thesis work and writing of this thesis. It is a great pleasure for me to work under their supervision. This has been a precious opportunity for me not only to gain knowledge and skill in the fluid power and control areas, but also to learn much more about approaches, attitudes towards work and interpersonal relationship.

I would also like to convey my thanks to all other professors and scholars of Project Neptune Laboratory, Department of Mechanical Engineering, Jadavpur University who helped me to complete this thesis. I am very thankful to all the teachers of Department of Mechanical Engineering, Jadavpur University for their immense co-operation during the thesis work. I am thankful to **Prof. Sadhan Kumar Ghosh, Prof. Sankar Dhar, Prof. Dipankar Sanyal, Prof. Gautam Majumdar** Head of the Department of Mechanical Engineering, Jadavpur University, for their constant help in different academic and non-academic matters. I also like to acknowledge and express my gratitude to CAIR, ERIP, CHESS of DRDO for permitting and encouraging me to carry out the research work.

I would also like to grab this opportunity to express my heart-felt gratitude to my parent, wife, daughter and other family members and also friends whose suggestions and helping attitudes helped my way out to the timely completion of the thesis.

At last but not the least, I can whole-heartedly express my thanks to all of my colleagues of Kalyani Govt. Engineering College and Head of the Department of Mechanical Engineering, **Prof Santanu Das**, who have helped me, directly or indirectly, during the completion of this research work.

Date:

Place: (Sibsankar Dasmahapatra)

Contents

ABSTRACT

Electrohydraulic actuation systems, EHAS has wide range of heavy-duty applications. But, the challenges in the controller development for such systems are nonlinearities, inexact mathematical models, unmodeled dynamics, parameter variations and uncertainties. Nonlinearities of high static friction in industrial cylinders and large deadband of proportional valves in rugged systems are more severe than in precision systems with servovalves and servocylinders. In recent times, Sliding Mode Controller or SMC has been emerged as robust solution against uncertainties. In the present work, two controllers have been developed, which subsequently have been implemented in real time for different EHAS designed and installed in the laboratory. In a controller design with SMC, a fuzzy controller has been coupled to realize an FSMC controller. The other type has been designed by combining a nonlinear integral or I controller with SMC, leading to an SMIC. The proposed controllers have been adapted on-line by minimizing a Lyapunov functional together with constraining the parameter growth by projection operator. Both from theoretical standpoint and through numerical simulation, the design is established as convergent. Experimental setup of EHAS producing linear and angular motion has been developed for the purpose of testing the developed controllers in real time. A real-coded genetic algorithm has been used to determine the parameters for the system and controller settings prior to adaptation. Real-time experiments have clearly shown the SMIC to have high tracking accuracy and bandwidth better than those achievable from some existing controllers. The benefits of lower steady state error of I controller and higher disturbance rejection capability of SMC makes SMIC as the most suitable controller for the linear and angular-motion EHAS under consideration.

For the linear-motion EHAS, using SMIC, satisfactory responses with no chattering have been achieved for standard regulation and tracking demands up to 7.0Hz of 0.02m amplitude of sinusoidal response despite the valve deadband of 10% and bandwidth of 25Hz. The bandwidth of the angular-motion EHAS is 10Hz with 1^0 link motion, which can be attributed for the higher-grade servo proportional valve. Reasonably good performance at reduced amplitude and increased frequency opens up the possibility of the use of a low-cost proportional valve for applications in which servovalves are customarily used.

NOMENCLATURE

Scalar Symbols

Symbol	Description	Unit
a	Amplitude	m
A_{a1}	Flow area in chamber Ch1	m^2
A_{a2}	Flow area in chamber Ch2	m^2
c	Proportionality constant for the friction proportional to linear velocity of the oscillating mass	$Kgms^{-1}$
$\hat{c}_i$	Center of each fuzzy subset	ms^{-1}
c_e	Composite error	ms^{-1}
C_{v1}	Valve coefficients in port A	$m^3/(s.V.\sqrt{Pa})$
C_{v2}	Valve coefficients in port B	$m^3/(s.V.\sqrt{Pa})$
d	System disturbance	ms^{-2}
d_b	Bore diameter of cylinder	m
d_r	Piston rod diameter	m
e	Error	m
$\dot{e}$	1st order error dynamic	ms^{-1}
$\ddot{e}$	2nd order error dynamic	ms^{-2}
f	Frequency	Hz
F_c	Coulomb friction	N
F_b	Maximum boundary lubrication friction	N
F_f	Friction in actuator	N
F_T	External force due to effect of torque	N
F_{0p}	Stiction correspond to the extension	N
F_{0n}	Stiction correspond to the retraction	N
g	Gravitational acceleration	ms^{-2}
I_L	Centroidal mass moment of inertia of the link	kgm^2

k	Stiffness of the spring	Nm^{-1}
l	Distance between the hinge and the center of mass	m
m	Mass of inverted pendulum	kg
m_a	Actuation-system mass	kg
m_L	Mass of link	kg
m_p	Piston mass	kg
m_w	Mass of external load	kg
M	Number of fuzzy rules	.
n_c	Fixed number of controllers	.
n_p	Number of parameters	.
P_1	Pressure in chamber Ch1	Pa
P_2	Pressure in chamber Ch2	Pa
Q_1	Supply flow	lpm
Q_2	Return flow	lpm
s	Sliding surface	ms^{-1}
s_e	Error coefficient	s^{-1}
s_1	1^{st} order SMC	ms^{-1}
$\dot{s}_1$	Time derivative of 1-SMC	ms^{-2}
s_2	2^{nd} order SMC	m
$\dot{s}_2$	Time derivative of s_2	ms^{-1}
$\ddot{s}_2$	Time derivative of $\dot{s}_2$	ms^{-2}
$s_{1,0}$	Initial value of s_1 at time $t = 0$	ms^{-1}
t	Time	s
t_r	Duration of the reaching phase	s
u	Control input to the dynamic system	ms^{-2}
$\hat{u}$	Estimate of input linearized control u	ms^{-2}
u^*	Ideal value of u	ms^{-2}

$\hat{u}_b$	Estimation of Biasing controller	ms^{-2}
$\hat{u}_f$	Estimation of Fuzzy controller	ms^{-2}
$\hat{u}_I$	Estimation of Integral controller	ms^{-2}
u_s	Control input to the dynamic system corresponding to SMC	ms^{-2}
$\hat{u}_{\text{FSMC}}$	Control input of FSMC	ms^{-2}
$\hat{u}_{\text{SMIC}}$	Control input of SMIC	ms^{-2}
$\hat{u}_{s,\text{FSMC}}$	Estimation of Sliding Mode Controller in FSMC	ms^{-2}
$\hat{u}_{s,\text{SMIC}}$	Estimation of Sliding Mode Controller in SMIC	ms^{-2}
v	Velocity of piston	ms^{-1}
v_b	Related velocity in typical friction characteristics	ms^{-1}
v_0	Slip velocity	ms^{-1}
v_s	Stribeck velocity	ms^{-1}
V	Control voltage	V
V_d	Deadband voltage	V
V_0	Minimum voltage required to operate PV (Proportional Valve)	V
V_{fu}	Estimation of an output voltage of fuzzy	V
x	Displacement of piston	m
x_d	Input demand	m
x_0	Initial position of the piston before its motion	m
$\dot{x}$	Velocity of piston	ms^{-1}
$\ddot{x}$	Acceleration of piston	ms^{-2}

Greek Symbols

Symbol	Description	Unit
α_b	Large constant of $\hat{u}_b$	ms^{-2}
$\hat{\alpha}_b$	Estimation of α_b	ms^{-2}
α_I	Large constant of $\hat{u}_I$	ms^{-2}
$\hat{\alpha}_I$	Estimation of α_I	ms^{-2}
α_s	Large constants of SMC	ms^{-2}
α_v	Viscous friction coefficient	kgs^{-1}
α_{fi}	Singleton output of the fuzzy rule base	ms^{-2}
$\hat{\alpha}_{fi}$	Estimation of α_{fi}	ms^{-2}
α_{vn}	Viscous friction coefficient correspond to the retraction	kgs^{-1}
α_{vp}	Viscous friction coefficient correspond to the extension	kgs^{-1}
$\alpha_{s,\mathrm{FSMC}}$	Large constants of $\hat{u}_{s,\mathrm{FSMC}}$	ms^{-2}
$\hat{\alpha}_{s,\mathrm{FSMC}}$	Estimation of $\alpha_{s,\mathrm{FSMC}}$	ms^{-2}
$\alpha_{s,\mathrm{SMIC}}$	Large constants of $\hat{u}_{\mathrm{SMIC}}$	ms^{-2}
$\hat{\alpha}_{s,\mathrm{SMIC}}$	Estimation of $\alpha_{s,\mathrm{SMIC}}$	ms^{-2}
$\hat{\beta}_i$	Inverse radius of each fuzzy subset	sm^{-1}
β_b	Large positive value in $\hat{u}_b$	m^{-1}
β_I	Large positive number in $\hat{u}_I$	m^{-1}
γ_b	Rate parameters for $\dot{\hat{\alpha}}_b$	s^{-2}
γ_c	Rate parameters for $\dot{\hat{c}}_i$	s^2m^{-1}
γ_f	Rate parameters for $\dot{\hat{\alpha}}_{fi}$	s^{-2}
γ_I	Rate parameters for $\dot{\hat{\alpha}}_I$	s^{-2}
γ_β	Rate parameters for $\dot{\hat{\beta}}_i$	s^6m^{-5}
$\gamma_{s,\mathrm{FSMC}}$	Rate parameters for $\dot{\hat{\alpha}}_{s,\mathrm{FSMC}}$	s^{-2}
$\gamma_{s,\mathrm{SMIC}}$	Rate parameters for $\dot{\hat{\alpha}}_{s,\mathrm{SMIC}}$	s^{-2}
θ	Angular motion of the link	degree
θ_d	Demand for angular motion	degree

θ_0	Initial angle made by link to the base	degree
ς	Angle made by the cylinder with the base	degree
ξ_{fi}	Output of the Gaussian membership function	·
$\xi_{s,\mathrm{FSMC}}$	Unknown bound for FSMC	ms^{-2}
$\xi_{s,\mathrm{SMIC}}$	Unknown bound for SMIC	ms^{-2}
λ_0	Coefficient of integral error	s^{-2}
λ_1	Coefficient of error	s^{-1}
μ	Membership function	·

Vector Symbols

Symbol & Formula	**Description**
$\mathbf{q}$	System parameters as $\alpha_{vp}\ \ \alpha_{vn}\ F_{0p}\ F_{0n}\ C_v\ V_0\ \ I_L\ C_v\ V_0$
$\mathbf{r}$	Disturbance parameters as pump pressure, tank pressure, actuated mass, the demand, its first and second derivatives
$\boldsymbol{\psi}$	Control parameters as $\hat{\alpha}_b\ \ \hat{\alpha}_{fi}\ \ \hat{\beta}_i\ \ \hat{c}_i\ \ \hat{\alpha}_{s,\mathrm{FSMC}}\ \hat{\alpha}_I\ \ \hat{\alpha}_{s,\mathrm{SMIC}}$
$\{\mathbf{p}_j\}_{n_c\times 1} \equiv [p_{ij}]_{n_c\times n_p}$	Parameter vectors involving parameters in $\mathbf{q}$ and $\boldsymbol{\psi}$
$\mathbf{b}_u \equiv (b_{ui})_{1\times n_p}$	Upper bound for $\mathbf{p}_j$
$\mathbf{b}_l \equiv (b_{li})_{1\times n_p}$	Lower bound for $\mathbf{p}_j$
$\mathbf{x} = (x_1 \equiv x\ \ldots\ x_n \equiv x^{(n-1)})^T$	n real-valued states
$\mathbf{u} = (u_1\ u_2\ \ldots\ u_p)$	An active control vector of real-valued p inputs
$\dot{\mathbf{x}} = \mathbf{A}\mathbf{x} + \mathbf{B}\mathbf{u}$, $\mathbf{u} = -\mathbf{K}\mathbf{x}$	An input linearized form with state matrix $\mathbf{A}$, state variable $\mathbf{x}$, input matrix $\mathbf{B}$, input $\mathbf{u}$ and gain matrix $\mathbf{K}$

List of Figures

List of Tables

CHAPTER 1: INTRODUCTION

1.1 Introduction to EHAS

Electrohydraulic Actuation System or EHAS causes desired actuation of a member, say a piston in a cylinder, through hydraulic pressurization controlled by an electrical control signal. The signal manipulates the setting of a valve positioned between a pump and an actuator, which involves the interface between the actuated member and an external system for utilizing the motion. Such systems are used in heavy industries and miniature devices due to its high power to weight ratio. The advantages of EHAS are easy maintenance, self lubrication and ruggedness or capability to work in the harsh conditions. Although, in comparison to electrical systems, EHAS has slower speed of response, but it possesses higher fault tolerance and much higher power density. Some applications of EHAS are high-power agricultural tractors for land tilling (Savaresi et al., 2004), efficient power-steering system compare to the traditional hydraulic steering system (Kemmetmuller et al., 2007; Daher and Ivantysynova, 2015), mobile equipment applications for earth moving and construction devices such as wheel loaders, excavators, harvesters (Cetinkunt et al., 2004; Ha et al., 2001), shield tunneling machine by using thrust hydraulic system (Huayong et al., 2009), press machines applied in the heavy industry (Truong and Ahn, 2011), automotive transmission clutch system in automobile sector (Song et al., 2012), actuation system in Smart Unmanned Aerial Vehicle (Lee et al., 2012), electrohydraulic thrust in large aircraft system (Lazic and Ristanovic, 2007; Zhen et al., 2015), multi degree of freedom for Stewart platform in advanced robotic and automation (Su and Duan, 2000; Cheng et al., 2004), parallel robotic machine tools (Zhang, 2010).

In many applications, the demands are simple regulation or simple tracking to be met with moderate precision and speed. Under any such situation, the ideal combination from the sustainability view point would be a proportional valve, or PV, and an industry-grade actuator. In comparison to proportional valves, servo valves and servo cylinders are costlier (Eryilmaz and Wilson, 2006). This is to meet their precision manufacturing requirement of higher tolerance grade. These systems also call for refined oil filtration requiring frequent maintenance that could be difficult to provide in many remote applications. Both proportional and servo valves have nonlinear

features like square root relations at the metering orifices together with changing jet angle (Watton, 2009) against valve opening. The sources of nonlinearities in hydraulic cylinders are friction, oil compressibility, varying oil volume and end cushioning arrangement. Discontinuous nonlinearities due to large deadband (Bessa et al., 2010) have greater challenges in systems with proportional valves. The static friction discontinuities in hydraulic cylinders (Wang et al., 2008; Wang, 2010) are more significant in industry-grade actuators in comparison to servo-actuators. Therefore, improving the performance of low-cost EHAS either by making use of the advancements in the controller design or proposing a new formulation could indeed be a significant research contribution.

A circuit diagram of a simple EHAS has been depicted in Fig. 1.1 which comprises of motor M to drive the hydraulic pump which intakes oil from tank through filter and supply high pressurized oil in the hydraulic circuits. For fixed displacement pump in the system, there is a pressure relief valve PRV to maintain a maximum pressure limit. The non-return valve NRV allows flow from pump to other hydraulic circuits but blocks in the opposite direction. The proportional valve PV is used to regulate the direction as well as the quantity of oil flow from pump to the actuator causing motion of its piston. The actuator in Fig. 1.1 is double-acting with single piston rod separating left chamber Ch1 and right chamber Ch2. The connections between different components are made with oil pipeline. The inset of Fig. 1.1 shows the schematic of internal view of PV. The ports P and T are connected to pump and tank respectively. The ports A and B are connected with ports a1 of chamber Ch1 and a2 of chamber Ch2 respectively. The inset of Fig. 1.1 reveals that PV has spool-land arrangement, which can move parallel to the axis of PV. When solenoid a and b of PV are energized under the action of voltage V, it creates a magnetic force that pulls the armature into coil. This causes the armature to push the spool-land arrangement to control the corresponding connection between the ports P to A and B to T or P to B and T to A. The motions of spool-land arrangement for corresponding voltage $V(+)$ and $V(-)$ have been represented respectively by lines with single and double arrowheads. It can be stated that $V(+)$ causes rightward spool displacement to direct the flow between the ports P to A and B to T to sustain a rightward piston motion which has been defined here as extension of the piston. Similarly, $V(-)$ causes a leftward piston motion to generate the retraction motion of the piston.

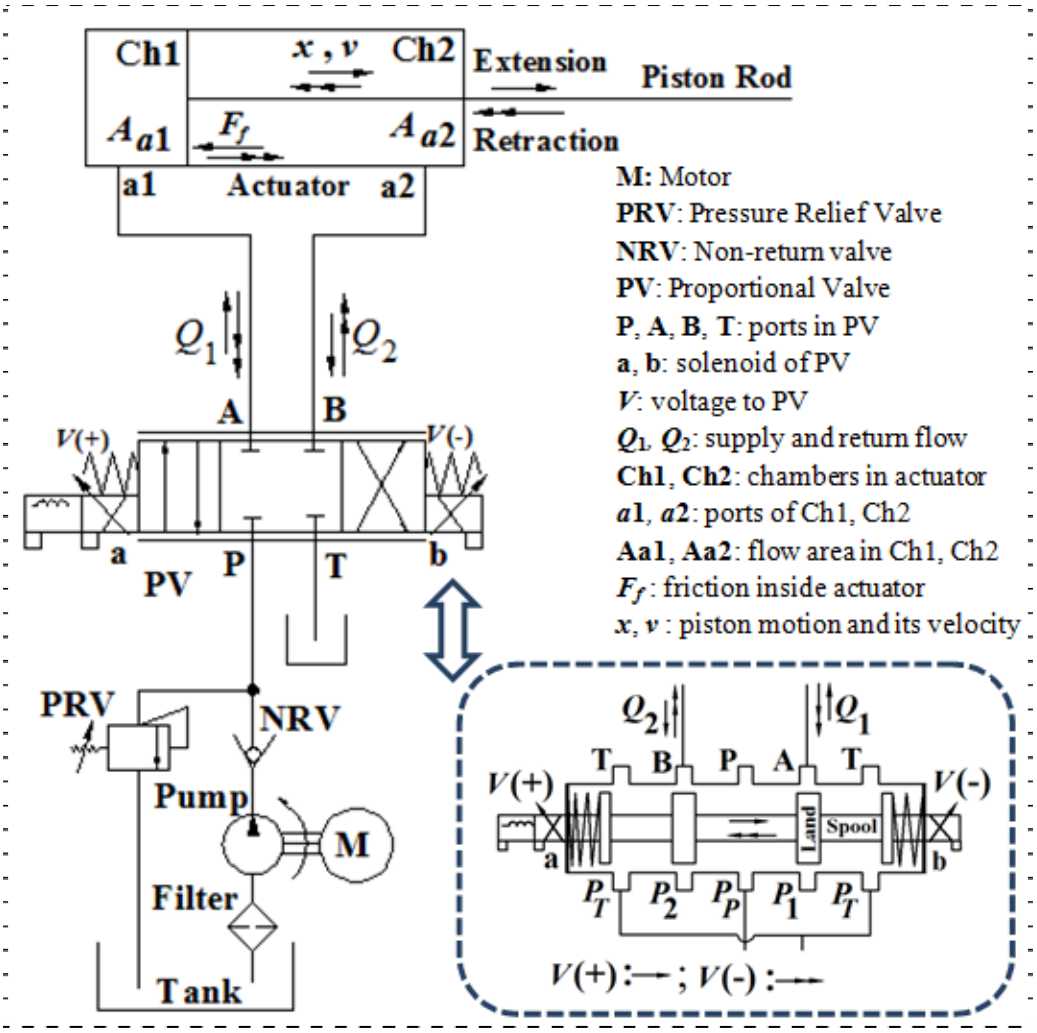

Figure 1.1: A circuit diagram of a simple EHAS with internal view of PV for double-acting actuator – single piston rod.

The arrangement of Fig. 1.1 shown here is without any external load to piston motion x and its corresponding velocity v. The pump pressure P_P has been considered to remain constant throughout the pipeline connected between pump and P port of PV. Similarly the tank pressure P_T has been considered as constant throughout the pipeline connected between tank and T port of PV. The ports A and B meter the supply and return flows Q_1 and Q_2 with pressure P_1 and P_2 respectively between ports a1 and a2 of the actuator. The pressure P_1 and P_2 have been treated as chamber pressures of the actuator.

The motion of the piston in Fig. 1.1 actuating piston mass m_p against friction F_f inside the actuator with flow area A_{a1} in Ch1 and A_{a2} in Ch2 can be expressed as

$$\dot{x} = v, \tag{1.1a}$$

$$\ddot{x} = [P_1 A_{a1} - P_2 A_{a2} - F_f]/m_p \text{ for extension,} \tag{1.1b}$$

$$\text{and } \ddot{x} = [P_2 A_{a2} - P_1 A_{a1} - F_f]/m_p \text{ for retraction,} \tag{1.1c}$$

where A_{a1} and A_{a2} can be represented in terms of the cylinder bore diameter d_b and piston rod diameter d_r as

$$A_{a1} = \pi d_b^2/4, \tag{1.1d}$$

$$\text{and } A_{a2} = \pi(d_b^2 - d_r^2)/4. \tag{1.1e}$$

Now it is necessary to find out the friction model and the modeling for chamber pressures to evaluate the piston motion at any instant from the motion dynamic equations (1.1a-c). Following Sarkar et al. (2013a) and Fig. 1.2, the cylinder friction in (1.1b) and (1.1c) can be modeled as

$$F_f = F_0 \text{ for } |v| \le v_0, \tag{1.2a}$$

$$\text{else } F_f = F_c + (F_b - F_c)\exp\{-(v - v_b)^2/(v_s - v_b)^2\} + \alpha_v(v - v_0), \tag{1.2b}$$

where F_0 is stiction, v_0 is slip velocity, F_c is Coulomb friction, v_s is Stribeck velocity and α_v is viscous friction coefficient, F_b is the maximum boundary lubrication friction and v_b is the related velocity.

With help of Fig. 1.2 and friction model equations (1.2a-b), the simplified form of friction model can be written as

$$F_f = F_{0p} + \alpha_{vp} v \text{ for extension,} \tag{1.2c}$$

$$\text{and } F_f = F_{0n} + \alpha_{vn} v \text{ for retraction,} \tag{1.2d}$$

where the subscripts p and n correspond to the extension and retraction respectively.

A simpler valve modeling adopted from Sarkar et al. (2013a) and Merrit (1967) can be implemented to obtain P_1 and P_2 assuming incompressible flow and negligible leakage. In such a condition, the continuity equation for the flow in the actuator chambers of Fig. 1.1 can be expressed as

$$Q_1 = A_{a1}\dot{x}, \tag{1.3a}$$

$$\text{and } Q_2 = A_{a2}\dot{x}, \tag{1.3b}$$

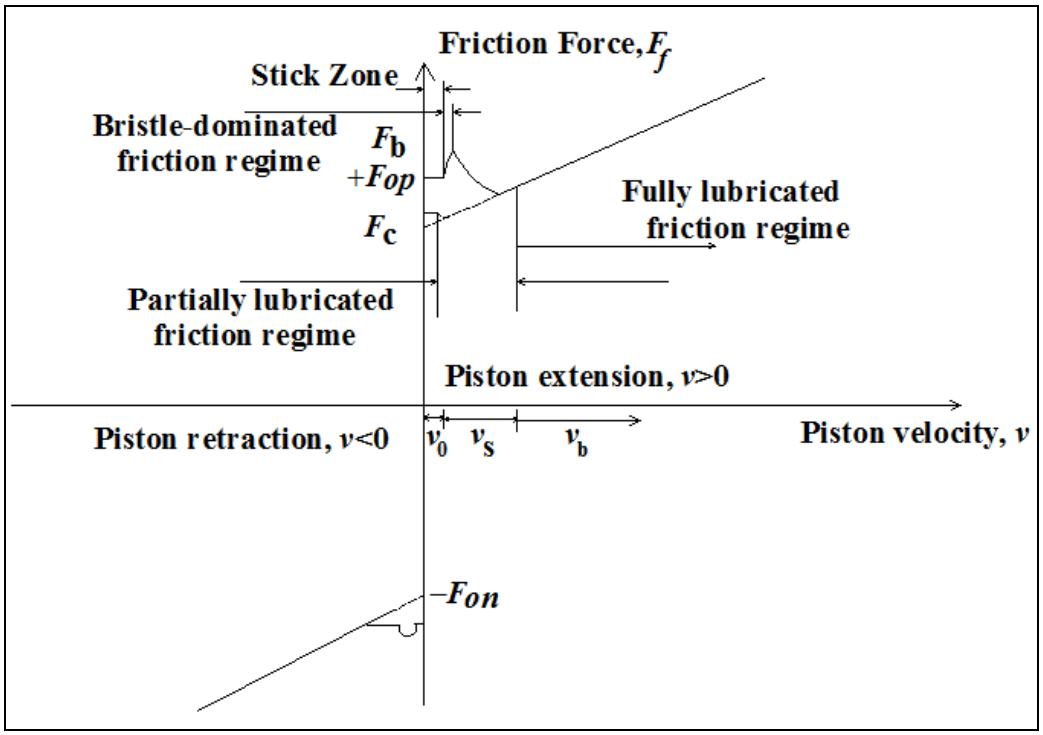

Figure 1.2: Typical Friction Characteristics for single-rod cylinder friction. (adopted from Sarkar et al. 2013a).

with the corresponding flow-pressure relationship for extension as

$$Q_1 = C_{v1} V \sqrt{P_P - P_1}\,, \tag{1.3c}$$

and $$Q_2 = C_{v2} V \sqrt{P_2 - P_T}\,, \tag{1.3d}$$

for retraction

$$Q_1 = C_{v1} V \sqrt{P_1 - P_T}\,, \tag{1.3e}$$

and $$Q_2 = C_{v2} V \sqrt{P_P - P_2}\,, \tag{1.3f}$$

with C_{v1} and C_{v2} as the valve coefficients in ports A and B respectively and V as the control voltage of PV.

By using continuity equations (1.3a-b) and corresponding flow-pressure relationships (1.3c-f), the chamber pressures P_1 and P_2 can be derived for extension as

$$P_1 = P_P - [A_{a1}\dot{x} / C_{v1} V]^2\,, \tag{1.3g}$$

and $$P_2 = P_T + [A_{a2}\dot{x} / C_{v2} V]^2\,, \tag{1.3h}$$

for retraction

$$P_1 = P_T + [A_{a1}\dot{x} / C_{v1} V]^2\,, \tag{1.3i}$$

and $$P_2 = P_P - [A_{a2}\dot{x} / C_{v2} V]^2\,. \tag{1.3j}$$

Now the dynamic equation for the extension motion of (1.1b) can be rewritten with the help of (1.1a), (1.2c), (1.3g) and (1.3h) as

$$\ddot{x} = -\frac{\alpha_{vp}}{m_p}\dot{x} - \frac{1}{m_p}\left[\frac{A_{a1}^3\dot{x}^2}{C_{V1}^2} + \frac{A_{a2}^3\dot{x}^2}{C_{V2}^2}\right]\frac{1}{V^2} + \frac{1}{m_p}(P_p A_{a1} - P_T A_{a2} - F_{0p}), \tag{1.4a}$$

and the corresponding retraction motion of (1.1c) can be rewritten with help of (1.1a), (1.2d), (1.3i) and (1.3j) as

$$\ddot{x} = -\frac{\alpha_{vn}}{m_p}\dot{x} - \frac{1}{m_p}\left[\frac{A_{a1}^3\dot{x}^2}{C_{V1}^2} + \frac{A_{a2}^3\dot{x}^2}{C_{V2}^2}\right]\frac{1}{V^2} + \frac{1}{m_p}(P_p A_{a2} - P_T A_{a1} - F_{0n}). \tag{1.4b}$$

The dynamic equations (1.4a-b) can be represented in a simplified form as

$$\ddot{x} = -\lambda\dot{x} + u + d, \tag{1.4c}$$

where each variable and coefficient can be expressed with help of (1.4a) and (1.4b) as

(i) λ is the coefficient of $\dot{x}$ and the value of this coefficient can be written as

$$\lambda = -\frac{\alpha_{vp}}{m_p} \text{ for extension,} \tag{1.4d}$$

$$\text{and } \lambda = -\frac{\alpha_{vn}}{m_p} \text{ for retraction,} \tag{1.4e}$$

(ii) u can be expressed as $u = -\frac{1}{m_p}\left[\frac{A_{a1}^3\dot{x}^2}{C_{V1}^2} + \frac{A_{a2}^3\dot{x}^2}{C_{V2}^2}\right]\frac{1}{V^2}$, (1.4f)

which has been treated as control input to the dynamic system corresponding to the control voltage V that can be written as

$$V = \dot{x}\sqrt{\{(A_{a1}^3/C_{V1}^2) + (A_{a2}^3/C_{V2}^2)\}/(m_p u)}\ , \tag{1.4g}$$

(iii) d has been considered as the system disturbance related to the friction and this variable can be represented as

$$d = \frac{1}{m_p}(P_p A_{a1} - P_T A_{a2} - F_{0p}) \text{ for extension,} \tag{1.4h}$$

$$d = \frac{1}{m_p}(P_p A_{a2} - P_T A_{a1} - F_{0n}) \text{ for retraction.} \tag{1.4i}$$

It can be revealed from the equations (1.4a) to (1.4i) that the dynamic of EHAS has nonlinear characteristic because it comprises nonlinear features like square root relations in the control input of (1.4f). To control such nonlinear EHAS with the disturbance either of (1.4h) or (1.4i), the controller formulation has to be developed to establish the control input u.

1.2 Basic Control of EHAS and its challenges

A basic control philosophy in terms of a simple block diagram has been depicted in Fig. 1.3. This involves a feedback loop to control the system output by comparing it with a reference input value to estimate the error. The error is used as an input signal to the controller to produce a control input to drive the system with the objective of minimizing the error. The sensor measures the system output and provides the feedback. The disturbance indicated in the block diagram in Fig. 1.3 may involve cylinder friction, valve leakage and some other effects. Controlling of EHAS becomes a challenging task in view of the nonlinearities associated with the system and the disturbances.

Precise control of EHAS becomes an important research work in present scenario. To control such a class of nonlinear system, the conventional PID (Chen et al., 2014) gives the assurance of only local stability but it is not sufficient to tackle the system uncertainty. Herreros et al. (2002) showed the benefit of varying the gains of conventional PID controllers through multi-objective optimization by using some benchmark transfer functions for linear plants. Obtaining transfer function for a nonlinear system is possible only for a limited range of operation. Application range of single set-point PID controllers was extended in the past by gain scheduling through fuzzy logic (Zhao et al., 1993), developing via a genetic searching approach (Lin et al., 2003), learning process using micro genetic algorithm (Yao and Wen, 2013), implementing the incremental method (Wang et al., 2016).

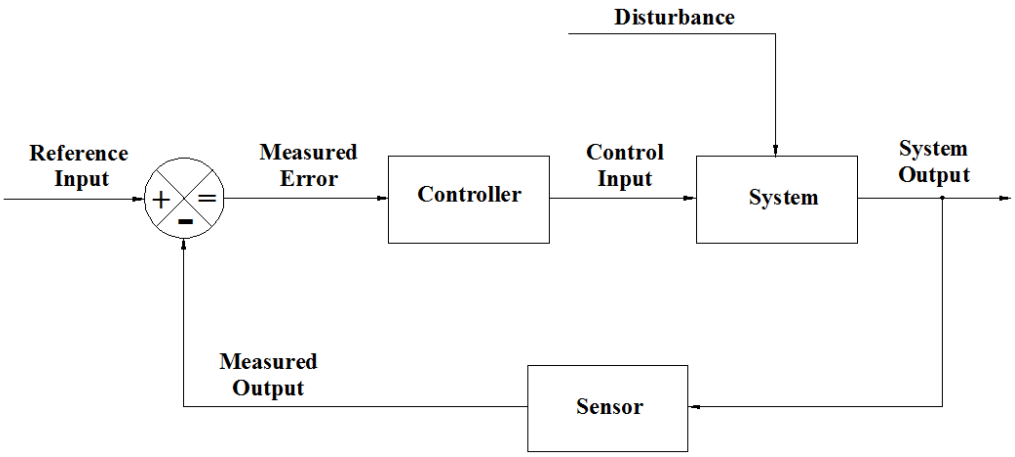

Figure 1.3: A simple block diagram of control philosophy.

The challenge of constructing a nonlinear system model for wide operating range is often by passed by using fuzzy controllers (Qiu et al., 2001). However, this brings in a new challenge of identification and tuning a large number of parameters (Mandal et al., 2015a) to control the motion by EHAS. Initialization and adaptation of these parameters for ensuring robustness against disturbances and uncertainties are often not easy. The disturbances and uncertainties as friction, leakage, noise, mathematical equations (Rahmat et al., 2011) involved in EHAS are nonlinear and unknown in nature. So this type of system cannot be controlled by continuous control method as PID.

A robust controller (Chern and Wu, 1992; Loukianov et al., 2009) can be recommended to get a better performance. The most well-known and best suitable choice of discontinuous control method is Sliding Mode Controller or SMC (Feng et al., 2013; Laghrouche et al., 2015), which has been emerged as robust solution against uncertainties. The SMC is constructed in such a way that can restrain the system uncertainty (Ding et al., 2015) by introducing a nonlinear discontinuous term to govern disturbances. The controller can also restrain some classes of mismatches (Yang et al., 2014) between the actual system and the system model. In view of only a few controller parameters, their identification and on-line adaptation is also relatively easier than a multi-parameter fuzzy controller. But the discontinuous term in SMC triggers undesirable high-frequency control oscillation, or chattering. This could induce fatigue in the mechanical parts and even destroy the system in a short period, as observed by Bartolini et al. (2003).

Brief outline of fuzzy and sliding mode controls along with the discussion on representative identification and adaptation procedures are outlined next.

1.3 Introduction to Fuzzy Control

Fuzzy logic is a rule based decision-making method mimicking the experience of an expert. The basis of fuzzy logic is fuzzy set theory developed by Zadeh (1965). An ordinary set is a collection of objects. Ordinary sets have two membership states: inclusion or exclusion. An object is either in the set or out of the set. Thus the degree of membership is either 0 or 1. Fuzzy set, on the other hand, allows for the partial membership in a set. The degree to which an object is a member of fuzzy set could vary between 0 and 1.

Conventional control algorithms need a mathematical model of the dynamical system to be controlled. However it is not always possible to obtain a reasonable mathematical model of the control system. Fuzzy control is a way of dealing with modeling problems by implementing linguistic, informally expressed control laws derived from the expert knowledge.

A linguistic rule can be defined through fuzzy set quantification, known as membership function. The membership function expresses the degree of belongingness to a particular set. With membership functions defined for controller or expert system inputs and outputs, one can formulate a rule base of IF-THEN type conditional rules. Such a rule base and the corresponding membership functions are employed to analyze controller inputs and determine controller outputs by the process of fuzzy logic inference.

A fuzzy-logic control strategy is developed in the rule-of-thumb line of working of a skilled operator. Therefore, once implemented it controls a process in the manner a human being does it manually with expertise gained from experience. The linguistic control rules that a human expert applies in an intuitive manner are directly translated to a rule base for a fuzzy logic controller. *Linguistic uncertainty* results from the imprecision of language. *High*, *medium* and *low* speeds describe subjective categories with meanings that depend on the context.

One of the basic concepts in fuzzy logic is the mathematical description of linguistic uncertainty using fuzzy sets. People often are forced to make decisions based on imprecise, subjective information. Even when the information does not contain precise quantitative elements, people can use fuzzy sets to manage complex situations successfully. One does not need to have well-defined rules to make decisions. Most often, one can approximate with rules that cover only a few distinct cases and apply them to a given situation. This approximation is possible because of the flexibility of the rules.

A car is *fast* if its speed is greater than 65 kmph and *slow* if its speed is less than 65 kmph. The crisp description of this speed range is illustrated in Fig. 1.4(a). The figure indicates that for any particular speed the membership value (μ_m) has a value either 0 or 1. Fig. 1.4(b) illustrates the fuzzy SLOW and FAST where the membership value varies from 0 to 1. When a car is moving at a speed between 50 and 80 kmph possesses partial membership in slow and partial membership in fast at the same time.

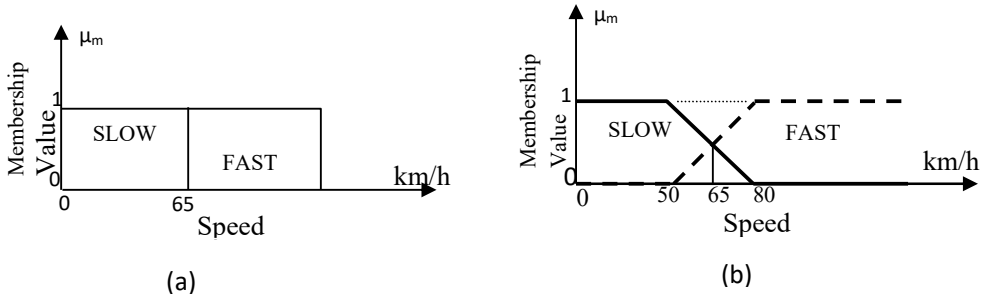

Figure 1.4: Crisp SLOW and FAST.

Another crisp description of speed ranges is given below:

Slow speed 0 to10 m/s

Medium speed 10 to 20 m/s

Fast speed 20 m/s

The crisp set and fuzzy set for slow, medium and fast speeds for the above speed ranges are given in Fig. 1.5(a) and Fig. 1.5(b) respectively and for the velocity of 12.5 m/s the crisp membership and the fuzzy membership values are found below.

Crisp membership value :

SLOW (0.0)

MEDIUM (1.0)

FAST (0.0)

Fuzzy membership value:

SLOW (0.3)

MEDIUM (0.7)

FAST (0.0)

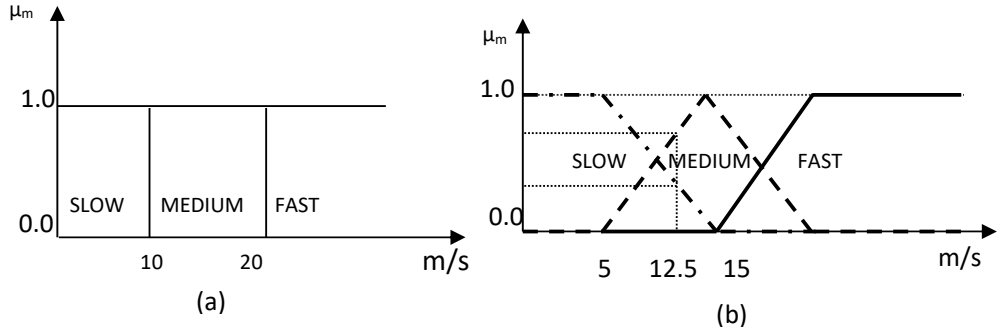

Figure 1.5: Crisp SLOW, MEDIUM and FAST.

The central element of fuzzy control design involves rule-based decision-making processes. A detailed and precise mathematical description is not always necessary for optimal operation of an engineering process. In other words, human operators are often capable of managing complex situations of a plant without knowing anything about differential equations. Their engineering knowledge is perhaps available in a linguistic form such as “if the drum pressure is high, stop feed water pump”.

Because of fully developed nonlinearities, distributed parameters, and time constants that are difficult to determine, it is often impossible for a control engineer to develop a mathematical system model. With fuzzy logic, linguistic representation of engineering knowledge is used to implement a control strategy.

The four basic steps of fuzzy control are stated as:

1) Identification of ranges of input and output,
2) Fuzzyfication of input and output,
3) Constructing fuzzy rule-base that simulates the working rules of an experienced worker in terms of a set **IF**<situation> **THEN** <action> logic.
4) De-fuzzyfication or fuzzy reasoning that is an inference process of exploiting the rule base to obtain a crisp input from the measured crisp output.

The rule format, mentioned in basic steps of fuzzy logic control, describes the necessary reaction, or conclusion to a certain situation or condition. These are linguistic expressions relating the qualitative knowledge of the system so as to ascertain the control from the measured system state. These are illustrated in the subsequent paragraph for the servo- actuation system. Let the velocity error be (VE) = U_d - U_m, acceleration error be (AE) = $\dot{U}_d$ – $\dot{U}_m$ and "OE" be the opening error. The fuzzy rules are given in Table 1.1.

Table 1.1: Fuzzy Rules

IF < VE is zero and AE is zero >	**THEN** <adjust OE to zero>	Z-Z-Z	1
IF < VE is +ve small and AE is –ve >	**THEN** <adjust OE to zero>	PS-N-Z	2
IF < VE is +ve large and AE is zero >	**THEN** <adjust OE to +ve small>	PL-Z-PS	3
IF < VE is +ve large and AE is –ve >	**THEN** <adjust OE to +ve large>	PL-N-PS	4
IF < VE is +ve small and AE is +ve >	**THEN** <adjust OE to -ve small>	PS-P-NS	5
IF < VE is +ve large and AE is +ve	**THEN** <adjust OE to -ve large>	PL-P-NL	6
IF < VE is -ve large and AE is zero >	**THEN** <adjust OE to -ve small>	NL-Z-NS	7
IF < VE is -ve large and AE is +ve >	**THEN** <adjust OE to -ve large>	NL-P-NL	8
IF < VE is -ve small and AE is –ve >	**THEN** <adjust OE to +ve small>	NS-N-PS	9
IF < VE is -ve large and AE is –ve >	**THEN** <adjust OE to +ve large>	NL-N-PL	10
IF <VE is zero and AE is –ve >	**THEN** <adjust OE to zero>	Z-N-Z	11

The membership functions (μ_m) for VE, AE and OE corresponding to the fuzzy rules given in Table 1.1 are illustrated in Figs. 1.6 (a) to (c) respectively. N, Z, P, NS, NL, PS, PL identify the negative, zero, positive, small negative, large negative, small positive and large positive domains respectively. By firing the rules Z-Z-Z, Z-N-Z and NS-N-PS for a given value of VE and AE, which is indicated by the *upward arrows* in the Figs. 1.6 (a) and 1.6 (b), a conservative estimation of opening error (OE) can be composed from Fig. 1.6 (c). The fuzzy estimation of OE according to different possible fuzzy rules has been described in the Figs. 1.7 (a) to (c). Similarly the composition of OE by Mamdani rule has been given in Fig. 1.8.

Two ***simple additive models***, namely the centroidal average rule and the Mamdani rule, the value of OE is composed respectively as

$$OE=\{[\mu_Z/OE]_1[\mu_Z/OE]_2 OE/_Z + [\mu_{PS}/OE]_9 OE/_{PS}\}/\{[\mu_Z/OE]_1[\mu_Z/OE]_2 + [\mu_{PS}/OE]_9\},$$

or $$OE=\{\max[(\mu_Z/OE)_1,(\mu_Z/OE)_2]OE/_Z+[\mu_{PS}/OE]_9 OE/_{PS}\}/$$

$$\{\max[(\mu_Z/OE)_1,(\mu_Z/OE)_2]+[\mu_{PS}/OE]_9\},$$

where $OE/_Z$ and $OE/_{PS}$ are the opening errors corresponding to unity membership value in the zero and positive-small subsets of the fuzzified opening error domain. In Mamdani fuzzy logic, **max**$\{[\mu_Z/OE]_1, [\mu_Z/OE]_2\}$ is accepted since the maximum value includes all other possibilities as a part of it.

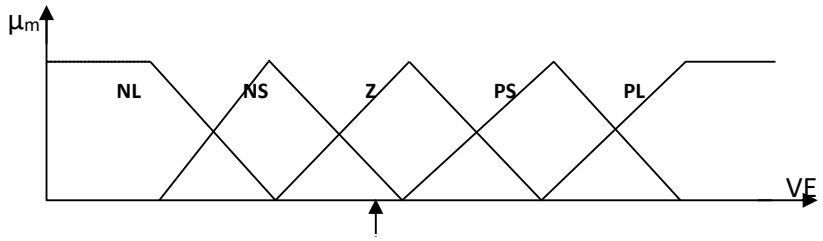

Figure 1.6a: Membership distribution of velocity error.

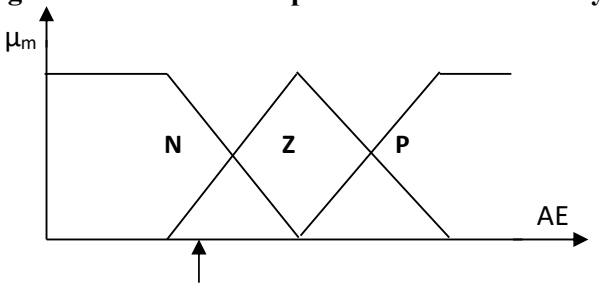

Figure 1.6b: Membership distribution of acceleration error.

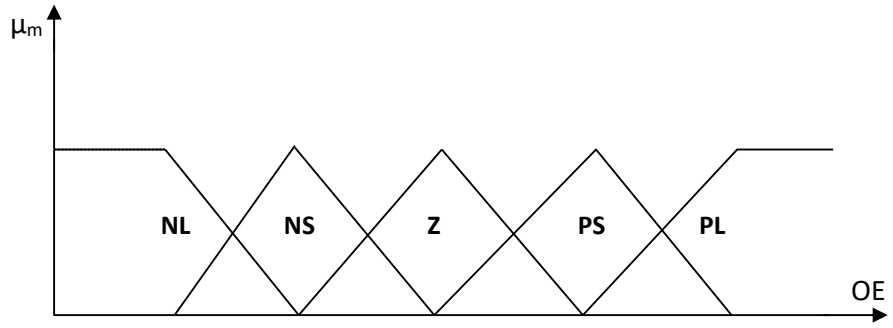

Figure 1.6c: Membership distribution of operating error.

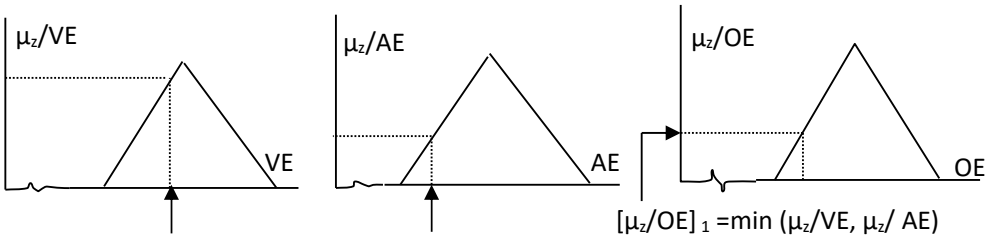

Figure 1.7a: Estimation of operating error by Z-Z-Z rule.

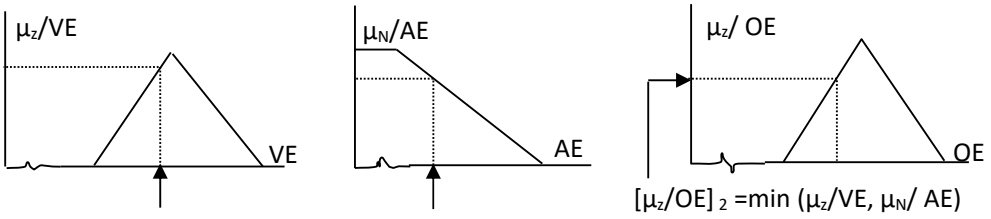

Figure 1.7b: Estimation of operating error by Z-N-Z rule.

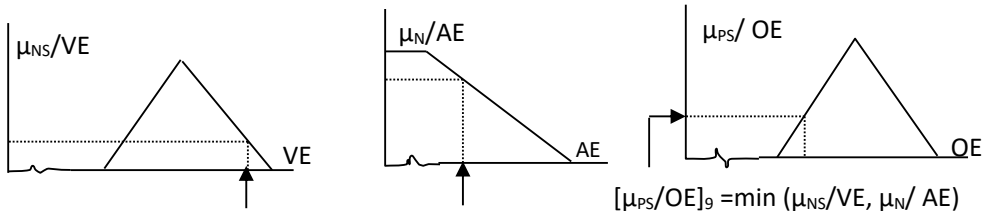

Figure 1.7c: Estimation of operating error by NS-N-PS rule.

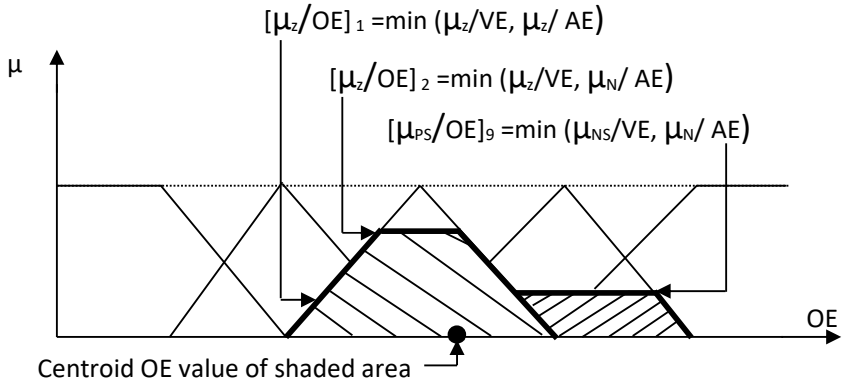

Figure 1.8: Composition of operating error by Mamdani rule.

The purpose of the controller in the context of an EHAS is to minimize the position error e by estimating an output voltage V_{fu} to be fed to the solenoid of the proportional valve, thereby metering the flow in and out of the cylinder for actuating the piston. Different fuzzy architectures (Mandal et al., 2015a, 2015b) considered are shown in Figs. 1.9 to 1.11. The output space is represented in terms of membership function κ by either discrete linear variations in Figs. 1.9 (a) and 1.10 (a) or by a set of singleton values in Figs. 1.9(b), 1.10 (b) and 1.11. Fig. 1.9 represents a single-dimensional input of e, the input space in Fig. 1.10 involves both e and $\dot{e}$.

In Fig. 1.11, the input is a composite error given by

$$c_e = \dot{e} + s_e e, \tag{1.5}$$

where s_e is error coefficient having the dimension of inverse of time that is s^{-1}.

The five fuzzy controller structures are shown in Figs. 1.9 to 1.11, in which the input membership functions MFs are denoted by μ for e in Figs. 1.9 and 1.10 and for c_e in Fig. 1.11 and by λ for $\dot{e}$ in Fig. 1.10. Each of the input and output spaces are represented by $(2q+1)$ fuzzy subsets

$$S \cup (-q, -q+1, ..., 0, ..., q-1, q) \text{ for } q \text{ equal to 2.} \tag{1.6a}$$

Of course, the integer values -2, -1, 0, 1 and 2 stand for NL, N, Z, P and PL linguistic fuzzy subsets. In each input subset, a crisp input has a membership value that is calculated on the basis of the chosen values for the elements of the vector.

Corresponding to the structures shown in Fig. 1.9, this vector is

$$e^{\mathrm{T}} = \{\mathrm{e_i}\}^{\mathrm{T}} = (\mathrm{e_{-q}} \ \ldots \ \mathrm{e_0} \ \ldots \ \mathrm{e_q}) . \tag{1.6b}$$

The structures depicted in Fig. 1.10 involve linear membership functions for both the position and velocity errors described respectively by the vectors in (1.6b) and

$$\dot{\mathrm{e}}^{T} = \{\dot{e}_j\}^{T} = (\dot{e}_{-q} \ \ldots \ \dot{e}_0 \ \ldots \ \dot{e}_q) . \tag{1.6c}$$

Gaussian input membership function shown in Fig. 1.11 is defined for their respective centre point by the vector

$$c^{T} = \{c_i\}^{T} = (c_{-q} \ \ldots \ c_0 \ \ldots \ c_q) . \tag{1.6d}$$

Irrespective of whether the output space is linear or singleton, the vector for describing the membership functions can be written as

$$V^{T} = \{V_k\}^{T} = (V_{-q} \ \ldots \ V_0 \ \ldots \ V_q) . \tag{1.7}$$

The Gaussian membership function shown in Fig. 1.11 is evaluated as

$$\mu_i = \exp\{-\beta_i^2 (c_e - c_i)^2\} , \tag{1.8}$$

where β_i is the inverse radius of each fuzzy subset.

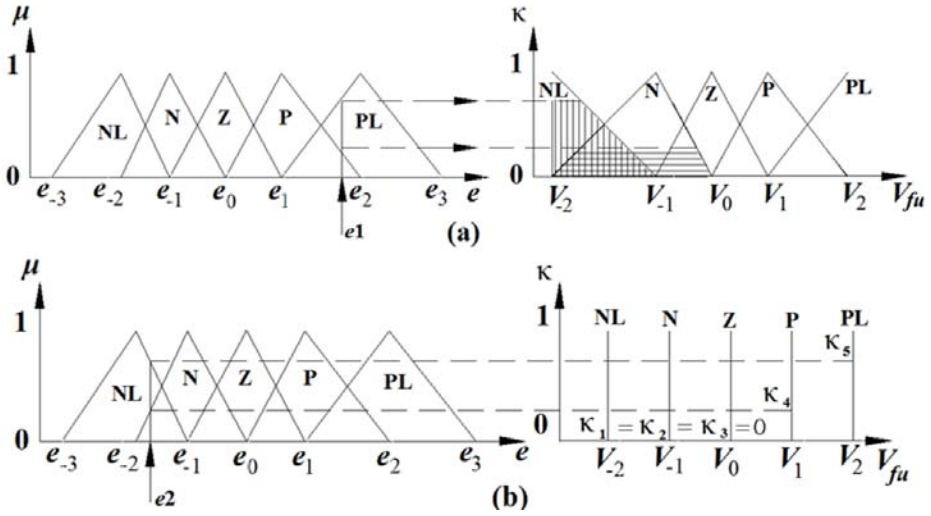

Figure 1.9: Fuzzy structures with single-dimensional input and single output with linear input MFs and output MFs of (a) linear type and (b) singleton type.

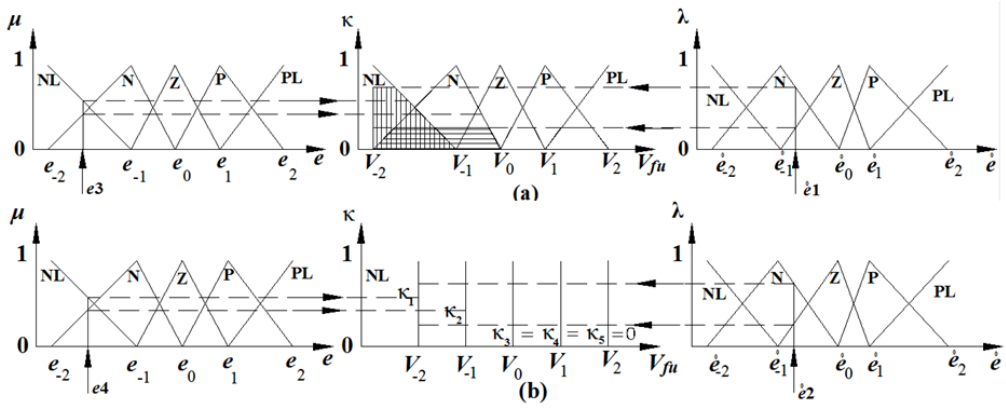

Figure 1.10: Fuzzy structures with two-dimensional input and single output with linear input MFs and output MFs of (a) linear type and (b) singleton type.

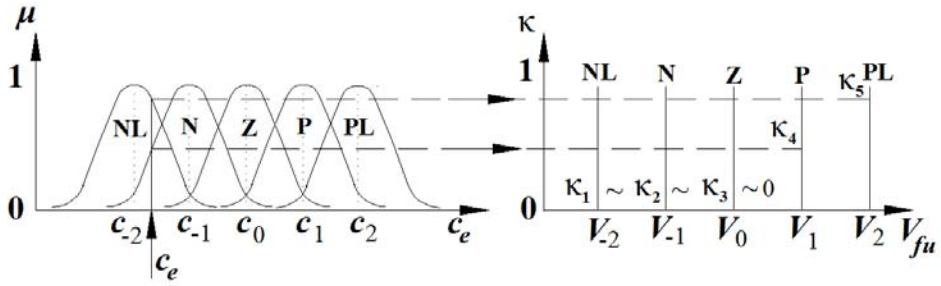

Figure 1.11: Fuzzy structures with single-dimensional Gaussian input MF and single output MF of singleton type.

The rule base is given in Table 1.2 with inputs e and $\dot{e}$ for crisp output voltage V_{fu}.

Table 1.2: Fuzzy rule base with two error inputs

$e \Rightarrow$	NL	N	Z	P	PL
$\dot{e} \Downarrow$	Fuzzy Voltage Subset				
NL	NL	NL	NL	N	Z
N	NL	NL	N	Z	P
Z	NL	N	Z	P	PL
P	N	Z	P	PL	PL
PL	Z	P	PL	PL	PL

Corresponding to the rules in Table 1.2, V_{fu} can be obtained as follows

Structure (a) in Fig. 1.9:

$$V_{fu} = \sum_i [(2-\mu_i)(V_{i+1} - V_{i-1})\mu_i V_i] / \sum_i [(2-\mu_i)(V_{i+1} - V_{i-1})\mu . \quad (1.9a)$$

Structure (b) in Fig. 1.9: $V_{fu} = \sum_i (\mu_i V_i)$. (1.9b)

Structure (a) in Fig. 1.10:

IF $\mu(e)$ is $\{\mu_i\} \equiv (\mu_{-q}, \mu_{-q+1}, ..\mu_{q-1}, \mu_q)^T$ AND $\lambda(\dot{e})$ is $\{\lambda_j\} \equiv (\lambda_{-q}, \lambda_{-q+1}, ..\lambda_{q-1}, \lambda_q)^T$

$$\text{THEN } V_{fu} = \sum_k [\{2 - \max(\mu_i, \lambda_j)\}(V_{k+1} - V_{k-1}) \max(\mu_i, \lambda_j) V_k] /$$

$$\sum_k [\{2 - \max(\mu_i, \lambda_j)\}(V_{k+1} - V_{k-1}) \max(\mu_i, \lambda_j)]. \quad (1.9c)$$

Structure (b) in Fig. 1.10:

IF $\mu(e)$ is $\{\mu_i\} \equiv (\mu_{-q}, \mu_{-q+1}, ..\mu_{q-1}, \mu_q)^T$ AND $\lambda(\dot{e})$ is $\{\lambda_j\} \equiv (\lambda_{-q}, \lambda_{-q+1}, ..\lambda_{q-1}, \lambda_q)^T$

$$\text{THEN } V_{fu} = \sum_k \max(\mu_i, \lambda_j) V_k . \quad (1.9d)$$

Structure in Fig. 1.11: $V_{fu} = \sum_i (\mu_i V_i) / \sum_i \mu_i$. (1.9e)

It is evident that a number of controller parameters are involved in a fuzzy controller structure. A sliding-mode controller offers the advantage of providing good control with lesser number of parameters.

1.4 Introduction to Sliding Mode Controller

Sliding-mode controllers, or SMCs, are often regarded as the most elegant and robust solution for tackling uncertainties and nonlinearities effect (Hwang, 1996; Wang et al., 2008). The control guides the system from the initial state through a reaching phase to a sliding phase, during which the system continues along a pre-determined trajectory, called as sliding surface depicted in Fig. 1.12. Following a reaching phase, the final stage involves a sliding phase. This phase is characterized by alternating the control forms at a high frequency.

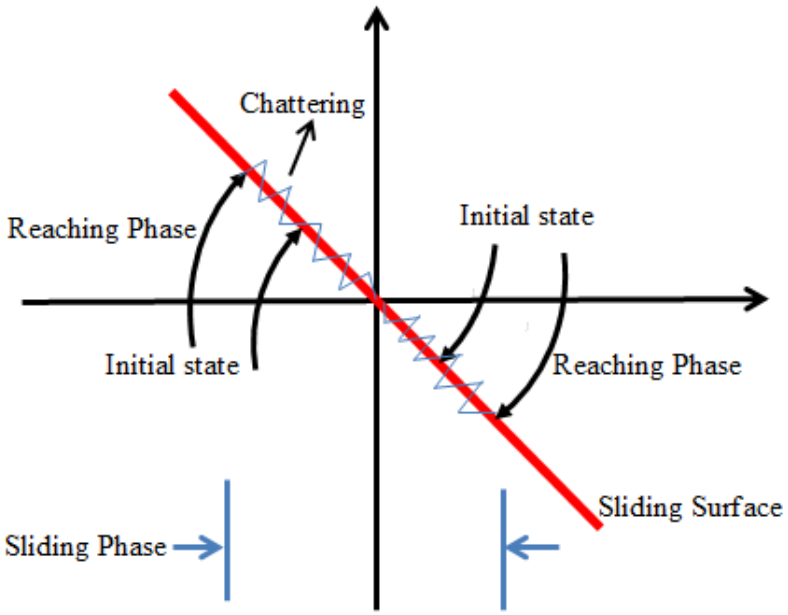

Figure 1.12: A traditional SMC with chattering.

A sliding-mode controller turns out to be very robust, since the latter phase dynamics is independent of the system features. But the penalty is a high-frequency control switching that is popularly referred as chattering portrayed in Fig. 1.12. The order of the SMC is defined as the maximum number of the derivatives of the output state that brings in control input in the system model. Different control strategies pertaining to first and second order systems along with mitigation of chattering have been described in the Chapter 2 for instance by Levant (1993, 2005, 2007).

Prior to implementing a controller structure, it is imperative to estimate reasonable values of these parameters that would ensure acceptable system performance. Optimization techniques (Herrera et al., 1998; Passino KM, 2002; Karaboga and Basturk, 2007) have been found to be useful for such identifications. Adoption of one such technique for system and controller identification has been discussed next.

1.5 Real-Coded Genetic Algorithm

The optimization technique is useful in finding an optimum solution of the design variables with or without constraints. Of course, the best solution, maximizing or minimizing a specified criterion, is selected from a generation containing a number of candidates, where each candidate is identified by specific values of all the variables. In the context of the controller design undertaken here, the target solution is the set of

controller parameters corresponding to the best system performance. Some applications of bio-inspired optimization pertaining to controllers for EHAS are Bacterial Foraging (Mandal et al., 2015b), Artificial Bee Colony (Mandal et al., 2016). For achieving an optimized controller design for the real-time system investigated in this work, a real-coded genetic algorithm, or RCGA, adopted from Sarkar et al. (2013b) has been used. The bio-mimicking features of GA are inheritance, mutation, selection, and crossover. With reference to Fig. 1.13, the implemented scheme has been discussed next in a generic manner.

The number of parameters has been considered as n_p by defining a search space of each parameter by specifying the upper bound $\mathbf{b}_u \equiv (b_{ui})_{1\times n_p}$ and the lower bound $\mathbf{b}_l \equiv (b_{li})_{1\times n_p}$ for the parameter vectors $\{\mathbf{p}_j\}_{n_c\times 1} \equiv [p_{ij}]_{n_c\times n_p}$. In the variation of GA implemented here, the fixed number of controllers n_c in each generation is an even number. Within the specified bounds, each parameter p_{ij} and controller C_j have been set first by using a random integer n_{ij} between 0 and 1 respectively as

$$p_{ij} = b_{li} + (b_{ui} - b_{li}) n_{ij} \text{ with } i = 1 \text{ to } n_p \text{ and } j = 1 \text{ to } n_c, \tag{1.10a}$$

$$\text{and } C_j \equiv (p_{1j} \;\; p_{2j} \;\; .. \;\; p_{ij} \;\; .. \;\; p_{n_p j}) \text{ with } j = 1 \text{ to } n_c. \tag{1.10b}$$

Using the system response $x(C_j, t)$ for each of C_j controllers and an input demand track $x_d(t)$, fitness value f_j and cumulative relative fitness R_j can be computed as

$$f_j = 1/[\int_0^T |x_d(t) - x(C_j, t)|\, dt + \varepsilon_c]. \tag{1.11a}$$

$$\text{and } r_j = \sum_{J=1}^{j} f_J / s, \tag{1.11b}$$

$$\text{where } s = \sum_{j=1}^{n_c} f_j, \tag{1.11c}$$

$$\text{and } \varepsilon_c = 10^{-3}, \text{ say if } |x_d(t) - x(C_j, t)| \leq 10^{-3}. \tag{1.11d}$$

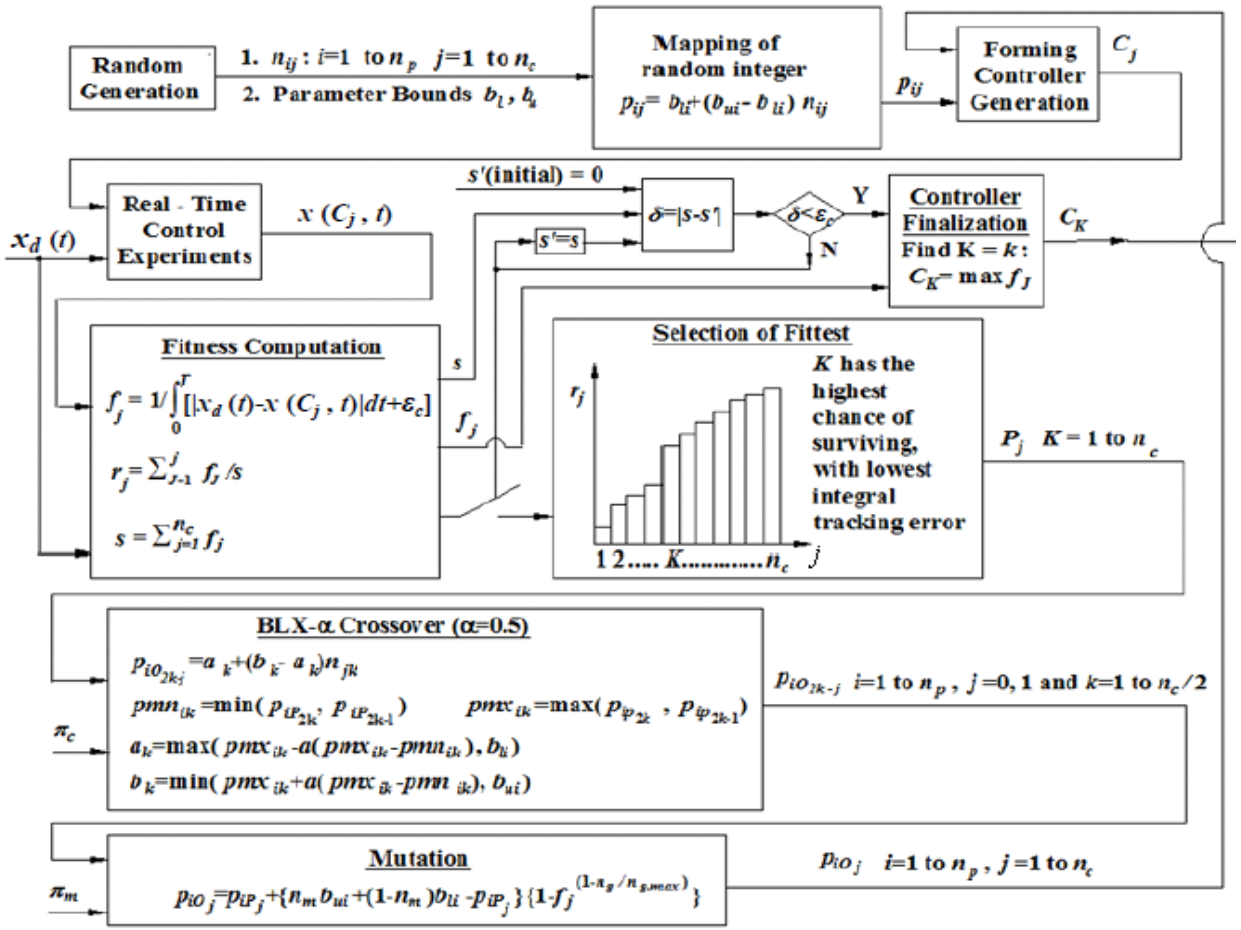

Figure 1.13: Controller optimization by GA with supporting real-time experiments. (adopted from Sarkar et al., 2013b)

In a block of Fig. 1.13, a typical relative fitness distribution r_j vs j is depicted involving the highest jump at K that would correspond to the lowest integral tracking error in the denominator of (1.11a) returning the highest fitness value in the numerator of (1.11b). The distribution obtained by processing a set of real-time performances is used to pick up a generation P_j of n_c controllers one after another, each time selecting a random numbers N_{sj} between 0 and 1. C_j would be selected in search P_1, if $r_{j-1} < N_{s1} \le r_j$. The controller C_K stands a good chance of getting selected, since (r_{K-1}, r_K) covers the largest span of the range used for choosing N_{sj}. The probability of the controllers of lower fitness values getting eliminated in the process is clearly higher. In other words, a controller with higher fitness value has a higher chance of surviving more number of times in selection forming the set P_j. Since a particular controller has probability of getting selected more than once, it is possible that the cumulative span covered by repeated selection of a particular controller in relative fitness distribution would be the largest. Such a controller has the highest probability of getting passed most number of times as a controller for next generation.

All the parameter vectors of the parent controller set P_j are then passed on for carrying out the genetic crossover and mutation processes yielding the parameter vectors for an offspring controller set O_j. Following an earlier recommendation in Herrera et al. (1998), BLX-α crossover mentioned in Eshelman and Schaffer (1993) with α equal to 0.5 and non-uniform mutation in Michalewicz (1992) have been adopted. Each crossover operation, executed $n_p \times (n_c/2)$ times with a probability of π_c, can be expressed as random selection of parameters for two offspring controllers between two bounds formed by the parameter values of a pair of parent controllers as

$$p_{iO_{2k-j}} = (a_k, b_k) \text{ for } i=1 \text{ to } n_p, j=0,1 \text{ and } k=1 \text{ to } (n_c/2), \tag{1.12a}$$

$$\text{where } a_k = \max(pmn_{ik} - \alpha(pmx_{ik} - pmn_{ik}), b_{li}), \tag{1.12b}$$

$$b_k = \min(pmx_{ik} + \alpha(pmx_{ik} - pmn_{ik}), b_{ui}), \tag{1.12c}$$

$$pmx_{ik} = \max(p_{iP_{2k}}, p_{iP_{2k-1}}), \tag{1.12d}$$

$$\text{and } \quad pmn_{ik} = \min(p_{iP_{2k}}, p_{iP_{2k-1}}). \tag{1.12e}$$

If a number chosen between 0 and 1 in a random manner turns out to be more than π_c, the crossover is not enabled and the selected parameter pair is passed off as offspring pair, unchanged at that stage. If the crossover is enabled, two consecutive random numbers n_{jk} between 0 and 1 give the changed offspring parameters as

$$p_{iO_{2k-j}} = a_k + (b_k - a_k) n_{jk} . \tag{1.12f}$$

Following the crossover involving all the parent pairs, each offspring is subjected to mutation with a probability of π_m. If the mutation is enabled for changing a parameter belonging to generation number n_g, then it is carried out by selecting a fractional random number f between 0 and 1 and another random number n_m that is either 0 or 1 to set the offspring parameter value as

$$p_{iO_j} = p_{iP_j} + [n_m b_{ui} + (1 - n_m) b_{li} - p_{iP_j}][1 - f^{(1 - n_g / n_{g,\max})}]$$

$$\text{for } i=1 \text{ to } n_p, j=1 \text{ to } n_c, \tag{1.13}$$

where $n_{g,max}$ is the set maximum number for stopping the optimization due to failed convergence. Such a formulation reduces the change brought in by mutation as the latter generation progress to higher maturity. The optimization process is terminated by finding a controller with highest fitness value achieved in the converged last generation, when the change δ in the cumulative fitness falls within a bound ε_c. While the optimization helps in offline identification of parameters, an adaptation is an online process of tuning the controller parameters. Lyapunov stability theory provides a basis of formulating an adaptive control law.

1.6 Lyapunov Stability Theory

Lyapunov stability theory pertains to a system, irrespective of it being linear or nonlinear, autonomous or non-autonomous, with passive or active control. Mathematical representations of these systems are now given in terms of a state vector of n real-valued states and an active control vector of real-valued p inputs respectively as

$$\mathbf{x} = (x_1 \equiv x \;\; x_2 \equiv \dot{x} \equiv x^{(1)} \;\; \ldots \;\; x_n \equiv x^{(n-1)})^T \;\; , \tag{1.14a}$$

$$\text{and } \mathbf{u} = (u_1 \;\; u_2 \;\; \ldots \;\; u_p) \;\; , \tag{1.14b}$$

with a superscript (n) implies n^{th} derivative of time (t).

The input linearization technique assists to represent the system equations (1.14a) and (1.14b) in an input linearized form as

$$\dot{\mathbf{x}} = \mathbf{A}\mathbf{x} + \mathbf{B}\mathbf{u}\,,\ \mathbf{u} = \text{-}\mathbf{K}\mathbf{x}\,, \tag{1.15}$$

with state matrix $\mathbf{A}$, state variable $\mathbf{x}$, input matrix $\mathbf{B}$, input $\mathbf{u}$ and gain matrix $\mathbf{K}$.

A nonlinear non-autonomous system is represented as

$$\dot{\mathbf{x}} = \mathbf{f}(\mathbf{x}, \mathbf{u}(\mathbf{x}), t)\,, \tag{1.16a}$$

where $\mathbf{f}$ is a function vector

$$\mathbf{f}(\mathbf{x}, \mathbf{u}(\mathbf{x}), t) = (f_1(\mathbf{x}, \mathbf{u}(\mathbf{x}), t)\ \ f_2(\mathbf{x}, \mathbf{u}(\mathbf{x}), t)\ \ \ldots\ \ f_n(\mathbf{x}, \mathbf{u}(\mathbf{x}), t)\ )^T\,, \tag{1.16b}$$

involving *n* scalar functions f_i possessing Lipschitz continuity.

Definition 1: A function $f(\mathbf{x}, t)$ is Lipschitz continuous, if $\| f(\mathbf{x}_1, t) - f(\mathbf{x}_2, t) \| \leq L \| \mathbf{x}_1 - \mathbf{x}_2 \|$ for a Lipscitz constant $L \geq 0$, t>0 and all $\mathbf{x}_1$, $\mathbf{x}_2 \in b(\mathbf{0}, h)$, where $b(\mathbf{0}, h)$ represents a ball of radius $h > 0$ centered around 0.

This continuity demands that for two different states in *h*-neighborhood of 0, the scalar functions remain bounded for all t>0. A piecewise continuous function can also hold Lipschitz continuity.

An autonomous or time-invariant system is a special case of (1.16a) and (1.16b) that can be modeled as

$$\dot{\mathbf{x}} = \mathbf{f}(\mathbf{x}, \mathbf{u}(\mathbf{x}))\,, \tag{1.17}$$

An autonomous passive or unforced system is a special case of (1.17) that does not involve any active control or external forcing can be written as

$$\dot{\mathbf{x}} = \mathbf{f}(\mathbf{x})\,. \tag{1.18}$$

Though system (1.15) can be rendered in term of (1.18) as

$$\dot{\mathbf{x}} = (\mathbf{A} - \mathbf{B}\mathbf{K})\mathbf{x}\,, \tag{1.19}$$

involving a linear vector function on the right hand side which is an active control system in view of the presence of the control gain matrix $\mathbf{K}$.

An equilibrium point of a dynamic system (1.15) to (1.19) is of course given by

$$\mathbf{x} = \mathbf{x}_e : \dot{\mathbf{x}} = \mathbf{0}\,. \tag{1.20a}$$

It is evident that the linear time-invariant, or LTI system represented by (1.15) has

$$\mathbf{x}_e = \mathbf{0}\,. \tag{1.20b}$$

A nonlinear system could have more than one equilibrium point. This is now illustrated with Fig. 1.14 of an inverted pendulum of mass *m* connected to a stick,

whose other end is loaded with a torsional spring of stiffness *k*. This end of the stick is free to rotate about a horizontal hinge end protruding from a vertical wall. The distance between the hinge and the center of mass is *l* and the mass of the stick is negligible. In terms of the angle θ that the stick subtends at an instant with respect to the upward vertical direction, the dynamics can be expressed as

$$ml^2\ddot{\theta} + cl\dot{\theta} + k\theta = mgl\sin\theta, \tag{1.21a}$$

where *c* is the proportionality constant for the friction proportional to linear velocity of the oscillating mass, *k* is the spring stiffness and *g* is the acceleration due to gravity. This is an example of a passive nonlinear autonomous system (1.19), since (1.21a) can be rewritten as

$$\begin{Bmatrix} \dot{x}_1 \\ \dot{x}_2 \end{Bmatrix} = \begin{Bmatrix} x_2 \\ g(\sin x_1)/l - cx_2/(ml) - kx_1/(ml^2) \end{Bmatrix}, \tag{1.21b}$$

$$\text{where } \mathbf{x}^T \equiv (x_1 \;\; x_2)^T \equiv (\theta \;\; \dot{\theta})^T, \tag{1.21c}$$

$$\text{and } \mathbf{f}^T(\mathbf{x}) \equiv (f_1(\mathbf{x}) \;\; f_2(\mathbf{x}))^T \equiv (\dot{\theta} \;\; -(g\sin\theta/l) - c\dot{\theta}/(ml) - k\theta/(ml^2))^T. \tag{1.21d}$$

For this system, the equilibrium points are

$$\mathbf{x}_e = (0 \;\; 0)^T, \tag{1.22a}$$

$$\text{and } (\pm\theta_{1e} \;\; 0)^T, \tag{1.22b}$$

$$\text{where } (\pm\theta_{1e} \;\; 0)^T \text{ is the solution of } \sin\theta_{1e} = k\theta_{1e}/(mgl). \tag{1.22c}$$

The first equilibrium point is of course the vertical configuration at rest. Of course, this is an unstable equilibrium point. With injection of small velocity to the mass towards left or right, the ensuing dynamics carry the mass to another equilibrium point with the stick inclined at an angle θ_{1e} counter-clockwise or clockwise respectively. Either of these equilibrium points is stable and all the three equilibrium points ate isolated.

Lyapunov functional method provides a means to understand the nature of stability of an equilibrium point or to arrive at a control law that would ensure stable operation around zero system error

$$\mathbf{e} = \mathbf{x}_d - \mathbf{x}, \tag{1.23}$$

where $\mathbf{x}_d$ is the demand and $\mathbf{x}$ is the system state described by (1.14a)**.** Of course, a specification of the position demand $x_{1d} \equiv x_d(t)$ is sufficient to specify the full demand state in case of a motion control system.

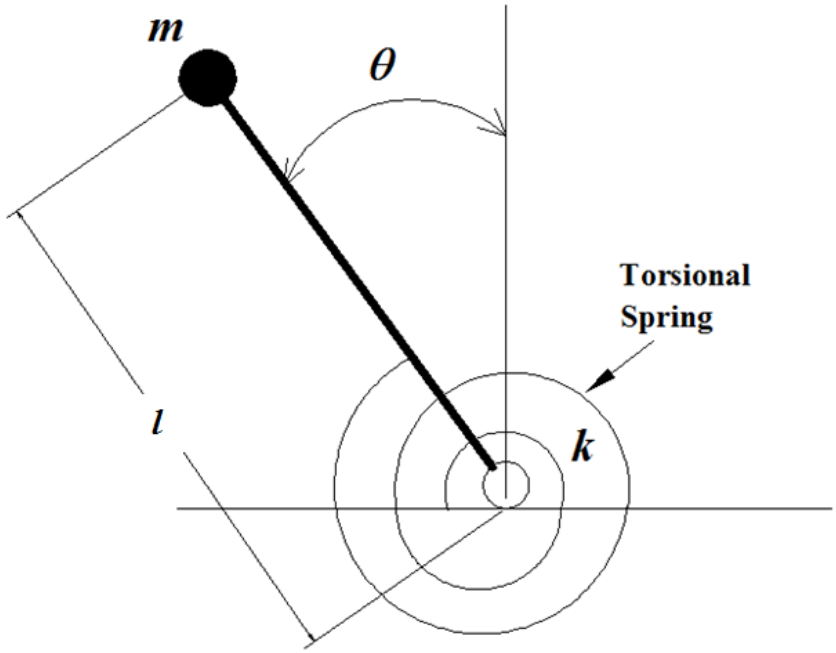

Figure 1.14: A simple inverted pendulum loaded with a torsional spring.

Lyapunov functional method warrants a formal definition of different classes of stability and definiteness properties of a function that are initiated next through two stability statements followed by two definitions.

Statement 1: An equilibrium point $\mathbf{x}_e$ is termed as locally stable, if for an $\varepsilon > 0$ and a $t_0 \geq 0$ there exists a $\delta(\varepsilon, t_0) > 0$ such that the system dynamics ensuing from an initial state $\mathbf{x}_0 \equiv \mathbf{x}(t_0)$ lying within δ -neighborhood of the equilibrium point implying $\| \mathbf{x}_0 - \mathbf{x}_e \| < \delta$ stays within an ε-neighborhood of the equilibrium point implying $\| \mathbf{x}(t) - \mathbf{x}_e \| < \varepsilon$ for all $t>0$. Otherwise, the equilibrium point is unstable.

As discussed earlier in the context of the system model (1.21a) that are recast as (1.21b) to (1.21d), Statement 1 is indeed consistent for (1.22a) describing an unstable equilibrium point and (1.22b) together with (1.22c) describing two stable equilibrium points.

If a system is stable without any δ -neighborhood restriction in Statement 1, then the equilibrium point is globally stable. Such a possibility exists for an LTI system (1.15) with single equilibrium point (1.20b).

If a system is stable for an $\delta \equiv \delta(\varepsilon)$ independent of t_0 in Statement 1, then the equilibrium point is uniformly stable. It may be noted that an autonomous stable system is uniformly stable.

Statement 2: An equilibrium point $\mathbf{x}_e$ is termed as locally asymptotically stable, if for a $t_0 \geq 0$ there exists a $\delta(t_0) > 0$ such that the system dynamics ensuing from an initial state $\mathbf{x}_0 \equiv \mathbf{x}(t_0)$ lying within δ-neighborhood of the equilibrium point such that $\| \mathbf{x}_0 - \mathbf{x}_e \| < \delta$ approaches $\mathbf{x}_e$ as $t \to \infty$ that is $\underset{t \to \infty}{Lim}\, \mathbf{x}(t) \to \mathbf{x}_e$.

If there is no restriction on initial time, then the asymptotically stable equilibrium point is uniformly asymptotically stable and the asymptotic equilibrium point is global, in case there is no neighborhood restriction.

Definition 2: A function $L(\mathbf{x})$ is called positive (or negative) definite, if $L(\mathbf{x}) > 0$ (or $L(\mathbf{x}) < 0$) for all $\mathbf{x} \neq 0$ and $L(\mathbf{0}) < 0$.

Definition 3: A function $L(\mathbf{x})$ is called positive (or negative) semi-definite, if $L(\mathbf{x}) \geq 0$ (or $L(\mathbf{x}) \leq 0$).

For a system model

$$\dot{s} = -s + u + d\,, \tag{1.24a}$$

that contains a control variable

$$s(\mathbf{x}) = \lambda_0 e + \lambda_1 \dot{e} + \lambda_2 e^{(2)} + .. + \lambda_{n-1} e^{(n-1)}\,, \tag{1.24b}$$

containing the error states in (1.23) and Routh coefficients λ_0, λ_1, λ_2, .., λ_{n-1} that are by definition positive, a disturbance term d is bounded by

$$|\, d \,| < \alpha\,, \tag{1.24c}$$

and a control term defined as

$$u = -\alpha\, \mathrm{sgn}(s)\,, \tag{1.24d}$$

a positive definite function by Definition 2 can be defined as

$$L(\mathbf{x}) = s^2 / 2\,. \tag{1.25a}$$

Using (1.24b-c) in the expression for derivative of (1.25a), it can be obtained that

$$\dot{L}(\mathbf{x}) = s\dot{s} = -s^2 - s\alpha\, \mathrm{sgn}(s) - sd \leq -s^2 - s(\alpha - |\, d \,|)\, \mathrm{sgn}(s) \leq 0\,, \tag{1.25b}$$

which is negative semi-definite by Definition 2. It should be noted that (1.24d) does not violate Lipschitz continuity stated under Definition 1.

It may be mentioned now that Lyapunov theorems pertain to the system behavior in the neighborhood of an equilibrium point and not the system as a whole. Without loss

of generality, a coordinate transformation through substitution of $\mathbf{x}$ by $\mathbf{x}+\mathbf{x}_e$ enables a shift of a non-zero equilibrium point $\mathbf{x}_e$ to $\mathbf{x}_e=\mathbf{0}$.

Statement 3: Lyapunov Stability Theorem

If a positive definite function $L(\mathbf{x})$ exists locally in the neighborhood of the origin with $L(\mathbf{0})=0$ for an autonomous system $\dot{\mathbf{x}}=\mathbf{f}(\mathbf{x})$ with the function $\mathbf{f}(\mathbf{x})$ possessing Lipschitz continuity such that its time derivative $\dot{L}(\mathbf{x})$ is negative semi-definite, then the origin is a stable equilibrium point.

Corollary 1: If a positive definite function $L(\mathbf{x})$ exists locally in the neighborhood of the origin with $L(\mathbf{0})=0$ for an autonomous system $\dot{\mathbf{x}}=\mathbf{f}(\mathbf{x})$ with the function $\mathbf{f}(\mathbf{x})$ possessing Lipschitz continuity such that its time derivative $\dot{L}(\mathbf{x})$ is negative semi-definite and $\dot{\mathbf{x}}=\mathbf{0}$ dynamics under the constraint $\dot{L}(\mathbf{x})=0$ has no equilibrium point other than the origin, then the origin is an asymptotically stable equilibrium point.

Statement 4: Lyapunov Asymptotic Stability Theorem

If a positive definite function $L(\mathbf{x})$ exists locally in the neighborhood of the origin with $L(\mathbf{0})=0$ for an autonomous system $\dot{\mathbf{x}}=\mathbf{f}(\mathbf{x})$ with the function $\mathbf{f}(\mathbf{x})$ possessing Lipschitz continuity such that its time derivative $\dot{L}(\mathbf{x})$ is negative definite with $\dot{L}(\mathbf{0})=0$, then the origin is an asymptotically stable equilibrium point.

Corollary 2: An equilibrium point is unstable, if not stable.

Corollary 3: If a positive definite function $L(\mathbf{x})$ exists for an autonomous system $\dot{\mathbf{x}}=\mathbf{f}(\mathbf{x})$ with the function $\mathbf{f}(\mathbf{x})$ possessing Lipschitz continuity, which is also radially unbounded implying $L(\mathbf{x})\to\infty$ as $\|\mathbf{x}\|\to\infty$ and possesses negative definite time derivative $\dot{L}(\mathbf{x})$, then $\mathbf{x}_e=\mathbf{0}$ is a globally asymptotically stable equilibrium point.

Proofs:

Since positive definiteness of L ensures it to be zero only for $\mathbf{x}=\mathbf{0}$ and $\dot{V}=0$ indicates achieving a local minima, the origin of the $L-\dot{L}$ plane represents attainment of local equilibrium.

An initial non-equilibrium state of the system $\mathbf{x}(0)$ and $\dot{\mathbf{x}}(0)\neq\mathbf{0}$ implies the state to be located away from the origin of the $L-\dot{L}$ plane. In view of the definiteness conditions of L and $\dot{L}$ in Statement 3, it could be located anywhere on the fourth

quadrant of this plane including the $\dot{L}=0$ axis, but excluding the $L=0$ axis. The exclusion arises for avoiding the violation of positive definiteness of L by virtue of it becoming less than zero consequent to the dynamics with $L=0$ and $\dot{L}<0$. In case the initial or any intermediate non-equilibrium state maps on the fourth quadrant excluding the $\dot{L}=0$ axis, the trajectory would proceed to diminishing L irrespective of whether $\dot{L}$ is locally increasing, decreasing or remaining constant.

In case $\dot{L}$ is negative semi-definite, the initial or any intermediate non-equilibrium state could map on the positive side of the $\dot{L}=0$ axis where $\dot{\mathbf{x}}$ is neither equal to or nearly equal to 0. Then by virtue of $\dot{\mathbf{x}}(t)\neq\mathbf{0}$, the trajectory would curve into the fourth quadrant to achieve $\dot{L}<0$ and hence to further proceed to acquire lower L. This dynamics would continue up to, say time T at which $\dot{L}(\mathbf{x}(T))=0$ and $\dot{\mathbf{x}}(T)\approx\mathbf{0}$ are concurrently achieved. In view of the uncertainties of a real-life system not captured by the modeling, it is quite possible that the trajectory on the $L-\dot{L}$ plane would stay on this point. This would imply accomplishment of local stability in conformity to **Statement 3**.

In case $\dot{\mathbf{x}}(T)\approx\mathbf{0}$ is not achieved anywhere on the positive side of the $\dot{L}=0$ axis and $\dot{\mathbf{x}}=\mathbf{0}$ only at the origin of the $L-\dot{L}$ plane, then the system would eventually proceed to the equilibrium state $\mathbf{x}_e=\mathbf{0}$ despite the possibility of acquiring $\dot{L}=0$ along the trajectory. This establishes the asymptotic stability statement of **Corollary 1** as acceptable.

In case $\dot{L}$ is negative definite, the initial or any intermediate equilibrium point cannot lie even on the $\dot{L}=0$ axis and the trajectory can acquire $\dot{L}=0$ only at $\mathbf{x}=\mathbf{0}$. Hence, the system would be asymptotically stable in accordance to **Statement 4**.

Corollary 3 is evident, since the radial unbounded condition $\underset{\|\mathbf{x}\|\to\infty}{Lim}\, L(\mathbf{x})\to\infty$ together with the negative definiteness of $\dot{L}(\mathbf{x})$ implies that $\dot{L}(\mathbf{x})$ would not be zero anywhere else other than the origin of $L-\dot{L}$ plane, no matter how near or how far the system state is with respect to the equilibrium at the origin of $L-\dot{L}$ plane.

Case Studies

(a) In view of (1.25a-b), control system (1.24a) to (1.24d) can be concluded as stable.

(b) Consider a simple pendulum problem and an inverse pendulum problem both without friction respectively given by

$$\dot{\mathbf{x}} \equiv (\dot{x}_1 \;\; \dot{x}_2)^T = (f_1 = x_2 \;\; f_2 = -g \sin x_1 / l))^T \equiv \mathbf{f}(\mathbf{x}), \tag{1.26a}$$

and $$\dot{\mathbf{x}} \equiv (\dot{x}_1 \;\; \dot{x}_2)^T = (f_1 = x_2 \;\; f_2 = g \sin x_1 / l))^T \equiv \mathbf{f}(\mathbf{x}), \tag{1.26b}$$

where x_1 is the angle that the stick makes with respect to the vertically downward and upward directions respectively and all other variables pertain to those described in the context of (1.21a).

For both the systems (1.26a) and (1.26b), a positive definite function with $\mathbf{x}_e = \mathbf{0}$ may be described for $-\pi < x_1 < \pi$ by a sum of kinetic energy and potential energy yielding

$$L(x_1, x_2) = \{ml^2 x_2^2 + mgl(1 - \cos x_1)\}/2. \tag{1.27}$$

These systems belong to the general form (1.19), for which it can be written that

$$\dot{L}(\mathrm{x}) = (dL/d\mathrm{x}^T)\dot{\mathrm{x}} = \nabla L.\mathrm{f}(\mathrm{x}) = (\partial L/\partial x_1 \;\; \partial L/\partial x_2 \;\; \ldots \;\; \partial L/\partial x_n)(f_1 \;\; f_2 \;\; \ldots \;\; f_n)^T. \tag{1.28}$$

Thus taking the derivative of (1.27) and using (1.26a) and (1.26b) in that respectively, it can be obtained that

$$\dot{L}(\mathbf{x}) = (-mgl \sin x_1 \;\; ml^2 x_2)(x_2 \;\; -g \sin x_1 / l)^T = 0, \tag{1.29a}$$

and $$\dot{L}(\mathbf{x}) = (-mgl \sin x_1 \;\; ml^2 x_2)(x_2 \;\; g \sin x_1 / l)^T = 2mglx_2 \sin x_1 \geq 0. \tag{1.29b}$$

Therefore in view of Lyapunov stability theorem and Corollary 1, the equilibrium state (0 0) for the simple and inverted pendulums are respectively stable and unstable. The continuous limit cycling of the system is consistent with conservation of energy along the system trajectory revealed by (1.29a).

(c) In presence of friction similar to system (1.21a) and the function (1.27), (1.26a) and (1.29a) get modified respectively to

$$\dot{\mathbf{x}} \equiv (\dot{x}_1 \;\; \dot{x}_2)^T = (x_2 \;\; -g \sin x_1 / l - cx_2 /(ml)))^T, \tag{1.30a}$$

and $$\dot{L}(\mathbf{x}) = (-mgl \sin x_1 \;\; ml^2 x_2)(x_2 \;\; -g \sin x_1 / l - cx_2 /(ml))^T = -clx_2^2, \tag{1.30b}$$

implying the system to be stable in view of the negative semi-definitiveness of (1.30b). In view of the energy dissipation that friction brings in, physically the system is asymptotically stable that Lyapunov theory fails to recognize. Therefore, this theory provides a necessary condition, but not a sufficient condition.

It would be now interesting to check Corollary 1 in this case.

$\dot{L}(\mathbf{x}) = 0$ in (1.30b) implies

$x_2 = 0$ for all t subsequent to achieving $x_2 = 0$, (1.30c)

which in turn implies

$\dot{x}_2 = 0$. (1.30d)

Now, (1.30b) and (1.30d) can be used together to write

$-g \sin x_1 / l - c x_2 /(ml) = 0$, (1.30e)

which together with (1.30c) leads to

$x_1 = 0$. (1.30f)

Hence, (1.30b) to (1.30f) together establish the equilibrium point as asymptotically stable by Corollary 1.

1.7 Scope of work

In the perspective detailed in the earlier sections, the main objective of the present work is set as to design and implement a chattering-free SMC on laboratory-scale EHAS that would be suitable in many real-life accurate position tracking devices. For achieving high-precision controller solution in such systems, a fuzzy controller coupled with SMC, or FSMC, has been contemplated to take care both continuous and discontinuous nonlinearity effects of the system dynamics. Another type of robust solution with SMC has been designed by combining a nonlinear integral or I-controller, leading to an SMIC. I-controller proposed as tangent hyperbolic function of time integral of the variable has an intrinsic saturating form. Lyapunov based adaptation technique has been adopted to get an asymptotically stable system. Projection operators have been used to restrict the controller operations within admissible bounds. The control command in each system has been extracted as electrical voltage through input linearization of the nonlinear system model. Two different single degree-of-freedom EHAS have been studied in order to obtain real-time validation of the controller performances. In both of these linear and angular-motion EHAS, the performances for different tracking demands, such as sinusoidal, step, and saw-tooth variations of the position demands have been investigated. Development of adaptive controllers for such EHAS have been considered, since its on-line parameter tuning capability has minimized the burden of conducting several experiments and using these results to carry out a parallel search for the optimized

parameter setting. For identification of both the non-adaptive parameters and the initial values of the adaptive parameters, optimization technique has been used. Based on detailed study of the real-time performance, a recommendation has been given for the preferred controller type.

1.8 Organization of the thesis

It is evident from the above discussion that SMC provides an evolving control strategy for its robustness. However, chattering remains a major problem in its implementation for real-life systems. In this backdrop, other control strategies have been coupled with SMC with the objective of attenuating the chattering. Two formulations for nonlinear systems representative of the linear and angular-motion EHAS along with their adaptation have been described. These are fuzzy-SMC, or FSMC, and a nonlinear integral (I) controller coupled with SMC, or SMIC. EHAS has been considered as the benchmark system, since it involves a host of nonlinear features.

Chapter 2 of the thesis considers first and second order SMC in a general manner. Different aspects of SMC, FSMC and SMIC have been brought in through simple numerical simulations.

In Chapter 3, the proposed controllers have been implemented in an experimental setup with an electrohydraulic valve-cylinder pair providing linear motion, typically utilized in construction, press, molding and material forming.

Chapter 4 deals with a laboratory-scale set up converting linear motion in a cylinder to an angular motion at the output, typically employed in excavators, thrust vectoring of rocket engines and aircraft maneuvering.

Mathematical modeling and input linearization techniques specific for extracting the control voltage from the input of SMC corresponding to the nonlinear electrohydraulic systems have been discussed in both Chapters 3 and 4. Also the parameter identification, controller architecture, selection of the suitable controller and the real-time performances of the controllers with different types of demands have been investigated in these chapters.

Chapter 5 concludes the major finding with the real time performances of the developed controllers. Also the future scope of this work has been outlined here.

CHAPTER 2: MODELING AND THEORETICAL ANALYSIS OF SLIDING-MODE CONTROL AND ITS VARIANTS

2.1 SMC Modeling

For designing the control input of the SMC, a sliding variable s can be expressed with combination of the different order error dynamic equations. With reference to Fig. 1.3, corresponding to an input demand x_d and the system response x as piston displacement of the EHAS mentioned in Fig. 1.1, the objective of the controller is to minimize the error e which can be defined as

$$e = x_d - x. \tag{2.1a}$$

Now with help of (2.1a), the system dynamic equation (1.4c) can be rewritten in terms of the error dynamic equation as

$$\ddot{e} = -\lambda\dot{e} + u_s + d, \tag{2.1b}$$

which is 2nd order error dynamic equation with the control input u_s corresponding to the SMC and d is the disturbance associated with the system.

The order of SMC can be considered as

(a) 1st order SMC or 1-SMC which has been formulated as

$$s_1 = \dot{e} + s_e e, \tag{2.2a}$$

with a positive error coefficient s_e. By using (2.1b), the single derivative of (2.2a) can be written as $\dot{s}_1 = u_s + d'$, (2.2b)

where $d' = d + (-\lambda + s_e)\dot{e}$. (2.2c)

(b) 2nd order SMC or 2-SMC can be defined as

$$s_2 = e, \tag{2.3a}$$

which has to be taken derivative as twice to get the control input equation (2.1b) as

$$\ddot{s}_2 = u_s + d', \tag{2.3b}$$

where $d' = d - \lambda\dot{e}$. (2.3c)

2.2 Design of SMC

The control input for the different order SMC has been formulated from Levant (2007) within the maximum and minimum bounds of α_s and $-\alpha_s$ as below

(a) Control input for 1-SMC: The control input u_s in (2.2b) has been defined as

$$u_s = -\alpha_s \,\text{sgn}\,(s_1), \tag{2.4a}$$

(b) Control input for 2-SMC: The 2-SMC control input u_s in (2.3b) has been considered as

$$u_s = -\alpha_s \,\text{sgn}\,(\dot{s}_2 + \beta_s |s_2|^{p/q}), \tag{2.4b}$$

with $\beta_s > 0$ and $p/q \le 1$, which has been used here to give different power in s_2 in the fractional form. The value of p has been considered as 1 and the value of q has been taken as $q \ge 1$ such that $p/q \le 1$.

From the control input equations (2.4a) and (2.4b), it can be inferred that the high-frequency oscillation can be attributed in the control due to the **sgn** function in the control input equation. This high-frequency oscillation in the control is called as chattering. In the context of the electro-hydraulic control system referred here, the practical implication of this would be voltage oscillation in the solenoid of the valve that may lead to its failure. The need of chattering attenuation for the SMC has been described by a Matlab simulation in the next section.

2.3 Simulations for 1-SMC and 2-SMC

A numerical study has been performed in this section for different order of SMC to demonstrate the corresponding control input, sliding variable. The need of chattering attenuation associated with SMC has been described through this simulation study. The simulation study has been done for the corresponding $s - \dot{s}$ plot termed as phase plane plot which is required to get an idea regarding the system dynamics.

The Matlab simulation study has been presented in Figs. 2.1 to 2.3 with a random disturbance input

$$d'(t) = |d'| \sin\{2\pi . rand(1,1)\}, \tag{2.5a}$$

given as a random scalar expression $rand(1,1)$ available as a built-in command in Matlab that provides random numbers between 0 and 1 at different instant of times at

which (2.2b) and (2.3b) would be integrated. Of course, the sin function converts the random distribution between ±1. It is well known that for

$$\alpha_s > |d'|, \tag{2.5b}$$

the sliding variable would stabilize to near-zero value observed by Levant (2007). Matlab simulation has been obtained with α_s equal to 2000 and d' equal to 1500 with time step of integration of 10^{-3}s. The corresponding simulation study has been done in next.

(a) *Simulation for 1-SMC*:

The simulation study of 1-SMC has been performed in Fig. 2.1 with a disturbance input of (2.5a). Fig. 2.1(a) depicts high-frequency chatter of control input with u_s equal to ±2000. The chatter is apparent in Fig. 2.1(a) after the initial period of decrease of the sliding variable to near-zero value revealed in Fig. 2.1(b). During the chattering phase, large oscillation $\dot{s}_1$ is exhibited in the phase-plane plot in Fig. 2.1(c). Prior to the near-origin chatter, the superimposed effect of disturbance over a nearly constant $\dot{s}_1$ is quite evident in this plot.

In order to establish the behavior presented in Fig. 2.1 for 1-SMC consistent with the system model in (2.2b), the control input in (2.4a) and the condition in (2.5b) together ensures $\dot{s}_1$ as bounded given by

$$\dot{s}_1 \in -(\alpha_s + |d'|, \alpha_s - |d'|)\,\mathrm{sgn}(s_1), \tag{2.6a}$$

or $s_1 \dot{s}_1 < 0$. (2.6b)

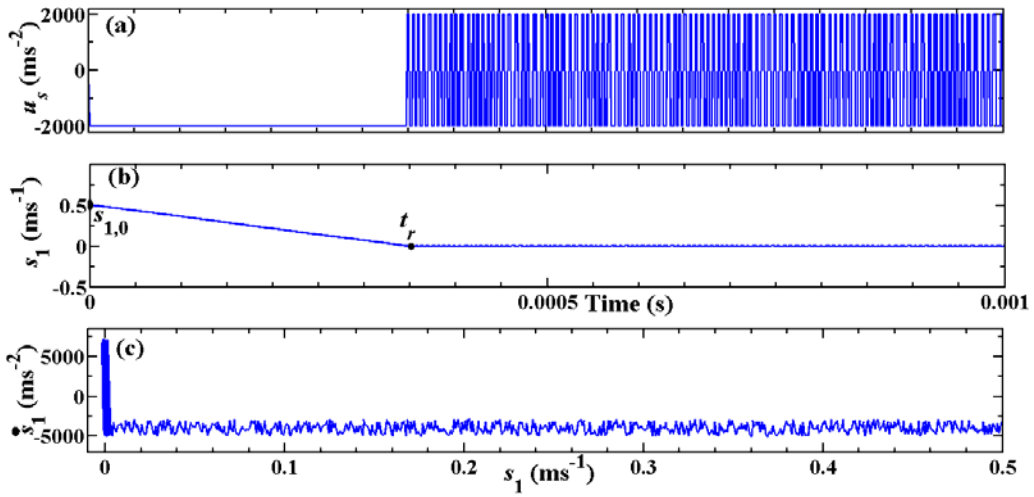

Figure 2.1: 1-SMC control input and phase plane plot.

This is consistent with $\dot{s}_1 < 0$ in Fig. 2.1(a) for $s_1 > 0$. Of course, $\dot{s}_1 < 0$ causes a decrease of s_1 with time towards zero as reflected in Fig. 2.1(b). This is achieved despite an oscillation in $\dot{s}_1$ apparent in Fig. 2.1(c) consistent with the form of disturbance (2.5b). The form (2.4b) leads to a reversal in u_s between $-\alpha_s$ and $+\alpha_s$ each time s_1 crosses zero that in turn results in a reversal in the sign of $\dot{s}_1$ according to (2.6a). These reversals are evident in Fig. 2.1(a) and Fig. 2.1(c). However, the chattering in the control input in Fig. 2.1(a) has been started when sliding variable s_1 achieved near to zero in Fig. 2.1(b). The phase of approach of the sliding variable to the sliding surface, which is $s_1 = 0$ in this case, is called the reaching phase.

Following the reaching phase, (2.2a) can be approximated as

$$\dot{e} + s_e e = 0\,, \tag{2.7a}$$

that ensures an asymptotic approach to $e = 0$. This phase is called the sliding phase. Now the duration of the reaching phase t_r can be derived from (2.6a) as

$$t_r = \int_0^{s_{1,0}} \frac{ds}{[\alpha_s + |d'|, \alpha_s - |d'|]} = \frac{s_{1,0}}{[\alpha_s + |d'|, \alpha_s - |d'|]}\,, \tag{2.7b}$$

where $s_{1,0}$ is the initial value of s_1 at time $t = 0$. This shows that a faster reaching phase can be achieved by having α_s larger but at the cost of higher amplitude of control chattering. In Fig. 2.1(b), $s_{1,0}$ has been considered as 0.5ms^{-1} and the corresponding t_r has been found approximately as 0.00035s.

(b) *Simulation for 2-SMC*:

In Fig. 2.2, the phase-plane behavior of the 2-SMC is shown for both of extension and retraction of the piston corresponding to a step demand to the change of the position of the system initially at rest for p/q equal to 1/2 and β_s equal to 10. Fig. 2.3 shows the phase-plane plot corresponding to the extension of the piston dynamics for different values of these values. This ratio equal to 1/2 yields the sliding surface as given by two semi-parabolas in $s_2 \dot{s}_2 < 0$ quadrants passing through the origin represented by

$$\dot{s}_2 + \beta_s \sqrt{|s_2|} = 0\,. \tag{2.8a}$$

According to the stated initial conditions for the extension or retraction demands and (2.3a), the initial point $s_{2,0}$ in Fig. 2.2 lies either on the right or left of the origin.

In view of (2.3b) and (2.4b) together yielding

$$\ddot{s}_2 \in -(\alpha_s + |d'|, \alpha_s - |d'|)\,\mathrm{sgn}(\dot{s}_2 + \beta_s\sqrt{|s_2|})\,. \tag{2.8b}$$

In view of the previous equation, the slope of the system trajectory in the $s_2 - \dot{s}_2$ phase plane can be obtained as

$$\frac{d\dot{s}_2}{ds_2} = \frac{\ddot{s}_2}{\dot{s}_2} = \frac{-(\alpha_s + |d'|, \alpha_s - |d'|)\,\mathrm{sgn}(\dot{s}_2 + \beta_s\sqrt{|s_2|})}{\dot{s}_2}, \tag{2.8c}$$

which yield the equation of system trajectory during the reaching and sliding phase respectively given by

$$\dot{s}_2^2 = -2(\alpha_s + |d'|, \alpha_s - |d'|)\,\mathrm{sgn}(\dot{s}_2 + \beta_s\sqrt{|s_2|})(s_2 - s_{2,0})\,, \tag{2.8d}$$

and $\dot{s}_2^2 - \dot{s}_{2,\varepsilon}^2 = -2(\alpha_s + |d'|, \alpha_s - |d'|)\,\mathrm{sgn}(\dot{s}_2 + \beta_s\sqrt{|s_2|})(s_2 - s_{2,\varepsilon})\,,$ (2.8e)

where $(s_{2,\varepsilon}, \dot{s}_{2,\varepsilon})$ is the system state at each instant of the sign reversal of u_s according to (2.4b) each time the trajectory crosses the sliding surface given in (2.8a). The crossing arises due to the finite-time delay in enacting the reversal in any real hardware. In case of the simulation study, the finite-time effect arises from the time step of numerical integration. The predicted reversals of the control corresponding to the numerical study are shown in the insets of Fig. 2.2.

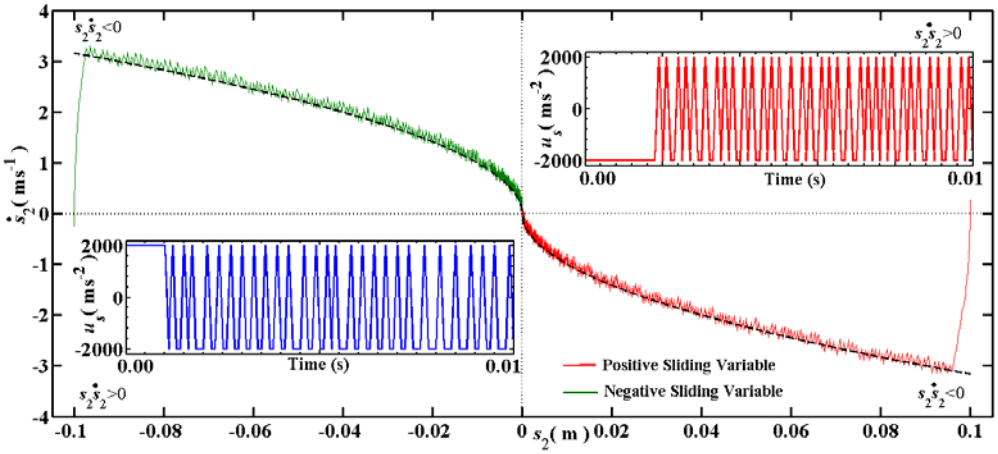

Figure 2.2: 2-SMC control input and phase plane plot.

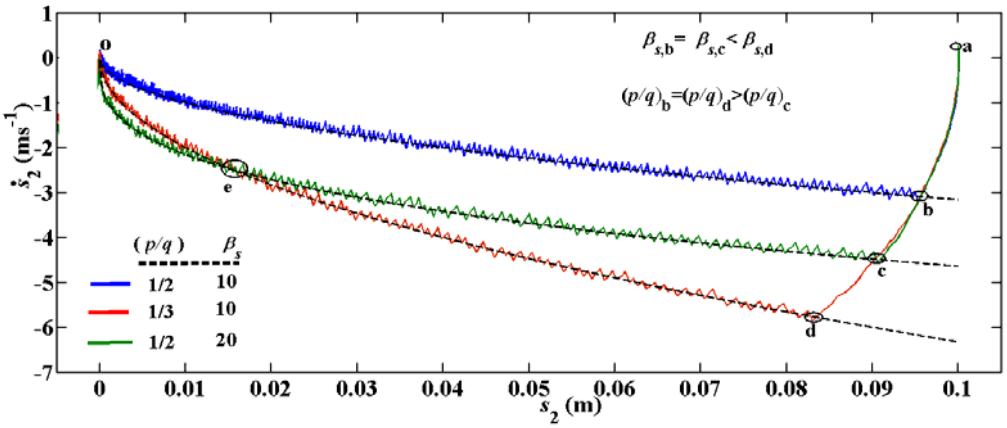

Figure 2.3: 2-SMC structure with different values of β_s and p/q.

Fig. 2.3 reveals that the 2-SMC reaches higher $\dot{s}_2$ at the intersection with the β_s surface at **b**, **c** and **d** respectively with β_s = 10, 10, 20 and p/q = 1/2, 1/3, 1/2. Of course, a higher $\dot{s}_2$ helps in reducing s_2 at a faster rate towards its zero target. However, a lower p/q may also imply continuing with a relatively higher $\dot{s}_2$ up to quite near the origin of the phase plane beyond **e**.

It is evident from the Figs. 2.2 and 2.3 that SMC ensures progress of the system error to zero in the face of the uncertainties and lack of information about system parameters. In other words, SMC is a robust strategy but there is high frequency chattering associated with the input control. An objective of the current research is the mitigation of the associated control chattering.

2.4 Formulations for FSMC and SMIC

In this thesis, one of the most important scope of work is to design a chattering free SMC and its implementation in the real-time. To design such chattering free SMC, it has been proposed two types of combined SMC, one is fuzzy controller coupled with SMC or FSMC and another is integral controller coupled with SMC or SMIC. The activity of fuzzy in FSMC is to take care the continuous nonlinearity effect of the nonlinear system dynamic observed by Shahnazi et al. (2008). The continuous type of nonlinearity effect contributed predominantly by the real-time friction in the cylinder and actuator surface. Similarly the role of integral controller I-controller of SMIC is to resolve the wind up problem involved in a conventional linear integral controller (Precup et al., 2014). I-controller would ensure the zero steady error in the system dynamic.

A detailed study of controller formulations of the proposed controllers FSMC and SMIC have been done in this section for an n^{th} order nonlinear system. The controller formulations have been established through the mathematical formulation of the nonlinear dynamic system and the controller inputs with their estimation, theory and proof. Lyapunov based adaptation technique has been adopted here to update the controller parameters with the corresponding change in the system.

2.4.1 Model of Nonlinear Dynamic System

A dynamic model with controller inputs and the disturbances has been considered here in the general form for the n^{th} order nonlinear system. The dynamic equation with system states $x, x^{(1)},..., x^{(n-1)}$ can be expressed for an n^{th} order nonlinear system as

$$x^{(n)} = -\lambda_{n-1}x^{(n-1)} - \lambda_{n-2}x^{(n-2)} - .... - \lambda_1 x^{(1)} - \lambda_0 x + \hat{u}(x, x^{(1)},..., x^{(n-1)}, \boldsymbol{\psi}, \mathbf{r}, \mathbf{q}, V) + d(x, x^{(1)},..., x^{(n-1)}, \mathbf{r}). \quad (2.9a)$$

Now the corresponding output formulation of (2.9a) can be written as

$$\mathbf{x} = (x \equiv y, x^{(1)},..., x^{(n-1)}). \quad (2.9b)$$

It can be mentioned that the dynamic system model (2.9a) and (2.9b) contain few terms which have important significance for this controller formulation study. The terms can be explained as below.

(a) The symbol ‘ˆ’ with a hat over a variable, say ‘.’ signifies its estimate.

(b) The coefficients $\lambda_0,...., \lambda_{n-2}$ and λ_{n-1} of the system states are Hurwitz coefficient so as to ensure stability of the system represented by dynamic equation in (2.9a). Of course for first and second-order system equations, the positive value of the coefficients is sufficient to guarantee system stability.

(c) $\boldsymbol{\psi}$ and $\mathbf{q}$ are vectors for control and system parameters respectively. $\mathbf{r}$ corresponding to the disturbance parameters which are described latter elaborately in this section.

(d) d is the disturbance that could depend on state vector $\mathbf{x}$ and non-Hurwitz coefficients in the disturbance vector $\mathbf{r}$.

(e) V used in the controller input $\hat{u}$ has been regarded as the actuation input. This input has the deadband V_d which can be again expressed as

$$V_d \in (V_0, -V_0), \quad (2.9c)$$

(f) $\hat{u}$ is the estimate of input linearized control u that could depend on $\mathbf{x}$, $\boldsymbol{\psi}$, $\mathbf{r}$ and $\mathbf{q}$.

Of course the adaptation of the estimate $\hat{u}$ would be convergent, if its attainment of the ideal value u^* would force the system (2.9a) to track the demand x_d yielding

$$x_d^{(n)} = -\lambda_{n-1}x_d^{(n-1)} - \lambda_{n-2}x_d^{(n-2)} - .... - \lambda_1 x_d^{(1)} - \lambda_0 x_d + u^* + d(x, \dot{x}, .., \mathbf{r}) + \delta d(e, \dot{e}, ..), \quad (2.10a)$$

where δd is a function of tracking error $e = x_d - x$, (2.10b)

inflicted by dependence of disturbance on demand vector.

To relate with the u^* and $\hat{u}$ the switching function or sliding surface (2.28b) has to be established which is basically a function of error dynamics. The expression of the switching function is expressed consequently.

2.4.2 Designing switching function or sliding surface

The requirement and a brief description of the sliding surface in the control dynamic has been discussed in Section 2.1, now it can be implemented for the nonlinear dynamic systems (2.9a) and (2.10a) which will together can be written as

$$\dot{s} = (u^* - \hat{u}) + \delta d, \quad (2.11a)$$

where sliding surface s can be expressed in terms of a filtered tracking error (Su et al., 2000) as

$$s = \lambda_0 \int e dt + ... + \lambda_{n-1} e^{(n-2)} + e^{(n-1)}. \quad (2.11b)$$

Now, it is required to estimate the control input $\hat{u}$ used in (2.11a) for the respective controller. For this purpose, a detailed study of the estimation and the corresponding role of the control input have been conferred subsequently.

2.4.3 Estimation and role of controller submodules

The system is nonlinear and this nonlinearity is discontinuous for the system, so the controller has been proposed in such a way that it should have the efficient capability to tackle these effects. For this purpose the controllers FSMC and SMIC have been proposed with combination of different types of controllers which have the different role in the control input.

(I) *Estimation of control input*

The corresponding control input for the proposed FSMC and SMIC in the nonlinear system (2.9a) has been estimated separately.

a) *Estimation of control input for FSMC*

The control input for FSMC has been considered as the combination of the three different controllers and it can be expressed as

$$\hat{u}_{\text{FSMC}} = \hat{u}_b + \hat{u}_f + \hat{u}_{s,\text{FSMC}}, \tag{2.12a}$$

where $\hat{u}_b$, $\hat{u}_f$ and $\hat{u}_{s,\text{FSMC}}$ are the consequent estimations of the three controllers as biasing, fuzzy and SMC respectively.

b) *Estimation of control input for SMIC*

The estimation of the control input for SMIC has been proposed with the combination of the two controllers as

$$\hat{u}_{\text{SMIC}} = \hat{u}_I + \hat{u}_{s,\text{SMIC}}, \tag{2.12b}$$

where $\hat{u}_I$ is estimation of an integral controller and $\hat{u}_{s,\text{SMIC}}$ is estimation of SMC.

(II) *Role of control input*

The role of each part in $\hat{u}_{\text{FSMC}}$ and $\hat{u}_{\text{SMIC}}$ has been discussed next.

a) *Role of Biasing controller* ($\hat{u}_b$): The biasing controller in FSMC is required to overcome the discontinuous nonlinearities effects associated with the nonlinear system. One of the most prominent examples of such discontinuous nonlinearities is stiction that depends on the direction of the initiation of motion.

Now the biasing controller has been proposed here in such a way that it can overcome the discontinuous nonlinearities. So that this biasing controller has been formulated as

$$\hat{u}_b = \hat{\alpha}_b \tanh(\beta_b e), \tag{2.13}$$

to make the controller as saturated within $\pm\hat{\alpha}_b$ where $\hat{\alpha}_b$ is the estimation of the α_b. To make the controller in the saturation level within certain limit, the parameter β_b has to be taken as a large positive value.

b) *Role of Fuzzy controller* ($\hat{u}_f$): The fuzzy controller is one of the most important part of FSMC and its contribution is approximately to take care the continuous nonlinearity effect such as dynamic friction in cylinder-actuator surface.

The fuzzy controller has been selected from Shahnazi et al. (2008) as

$$\hat{u}_f = \sum_{i=1}^{M} \{\hat{\alpha}_{fi} \hat{\xi}_{fi}(s)\}, \tag{2.14a}$$

where $\hat{\alpha}_{fi}$ and $\hat{\xi}_{fi}$ are the estimations of the α_{fi} and ξ_{fi} respectively. It has to be mentioned that the symbolic representations have their individual significance as M indicates the number of fuzzy rules, α_{fi} signifies the singleton output connected with the i^{th} rule of the fuzzy rule base and $\hat{\xi}_{fi}$ represents the output of the Gaussian membership function, given as

$$\hat{\xi}_{fi} = \exp\{-\hat{\beta}_i^2 (s(t) - \hat{c}_i)^2\}, \tag{2.14b}$$

where $\hat{c}_i$ is the center and $\hat{\beta}_i$ is the inverse radius of each fuzzy subset.

c) *Role of SMC* ($\hat{u}_{s,\text{FSMC}}$ *and* $\hat{u}_{s,\text{SMIC}}$): To design a precise controller for nonlinear system, it is mandatory to correct the different types of approximation and uncertainties associated with the system modeling and controller modeling. The approximations can be raised from the input linearization technique or the adaption scheme of the controller parameters. The source of uncertainties is the disturbance d in the system such as vibration, noise, oscillation. SMC has been proposed here to overcome the approximation and uncertainties.

Now the necessary correction has been required for the approximation and uncertainties of the system and the controller modeling. This correction has been regarded as 1st order SMC in terms of the sliding surface (2.11b) as

$$\hat{u}_{s,\text{FSMC}} = \hat{\alpha}_{s,\text{FSMC}} \operatorname{sgn}(s), \tag{2.15a}$$

$$\text{and } \hat{u}_{s,\text{SMIC}} = \hat{\alpha}_{s,\text{SMIC}} \operatorname{sgn}(s), \tag{2.15b}$$

where $\hat{\alpha}_{s,\text{FSMC}}$ and $\hat{\alpha}_{s,\text{SMIC}}$ are the estimations for the large positive constants $\alpha_{s,\text{FSMC}}$ and $\alpha_{s,\text{SMIC}}$ respectively.

It has been considered that the approximation and uncertainties together encompassing an unknown bound of $\pm\xi$, in such a way that all types of errors remain comprehend as

$$\alpha_{s,\text{FSMC}} > \left|\xi_{s,\text{FSMC}}\right|, \tag{2.15c}$$

$$\text{and } \alpha_{s,\text{SMIC}} > \left|\xi_{s,\text{SMIC}}\right|, \tag{2.15d}$$

where $\xi_{s,\text{FSMC}}$ and $\xi_{s,\text{SMIC}}$ are unknown bound for FSMC and SMIC rexpetively.

d) *Role of Integral controller* ($\hat{u}_I$): The integral controller has been used in case of SMIC and the purpose of this controller is almost similar to that of $\hat{u}_b$ incase of FSMC. The role of this controller is to make $\hat{u} \to -d$ in the input control for the system dynamic equation (2.9a) and consequently it will produce $\hat{u} \to u^*$ with the convergence scheme of the adaptive rule which will be discussed in the next section. The adaptive convergence of $\hat{u}$ to u^* would make the latter approach $-d-\delta d$ in (2.10a).

Integral controller has been proposed in this work as

$$\hat{u}_I = \hat{\alpha}_I \tanh(\beta_I \int s dt), \tag{2.16}$$

considering that $\hat{\alpha}_I$ will be saturated at $\pm\hat{\alpha}_I$ for a large positive number β_I and large s. The saturation capability of this controller resolves the wind up problem which is one of the worst concern involved in a linear integral controller. This controller would ensure the zero steady error in the system dynamic due to the reason that the controller architecture (2.16) being integral in nature.

2.4.4 Adaptation of Controller Parameters

The adaptation of the controller parameters is indispensable for such nonlinear dynamic system and the real-time adaptation technique is an emerging research field in the modern engineering sector. The real-time adaptation process does not requires the offline optimization technique, which needs the post processing after each run of the real-time execution and so that the offline technique will take more time compare to the proposed online adaptation technique. For these reasons, a detailed study regarding the adaptation technique has been reported here to implement the real-time adaptation of the controller parameters of $\hat{u}_{\text{FSMC}}$ and $\hat{u}_{\text{SMIC}}$.

The controller parameters can be expressed in terms of control parameter vector ψ for both types of controllers. The respective controller parameters $\hat{\alpha}_b$, $\hat{\alpha}_{fi}$, $\hat{\beta}_i$, $\hat{c}_i$, and $\hat{\alpha}_{s,\text{FSMC}}$ of (2.13), (2.14a), (2.14b) and (2.15a) can be expressed in terms of the estimated control parameter vector for FSMC as

$$\hat{\psi}_{\text{FSMC}} = (\hat{\alpha}_b \quad \hat{\alpha}_{fi} \quad \hat{\beta}_i \quad \hat{c}_i \quad \hat{\alpha}_{s,\text{FSMC}}). \tag{2.17a}$$

Similarly the controller parameters $\hat{\alpha}_I$ and $\hat{\alpha}_{s,\text{SMIC}}$ for SMIC can be expressed as

$$\hat{\psi}_{\text{SMIC}} = (\hat{\alpha}_I \quad \hat{\alpha}_{s,\text{SMIC}}). \tag{2.17b}$$

At a sampling interval T_s, these estimates of the parameters should be updated such that $\hat{u} \to u^*$ forcing δd in (2.10a) to zero for small error (2.10b) causing a first order change in disturbance related to $\mathbf{x}_d$ than $\mathbf{x}$ defined in (2.9b).

The adaptive rules for adaptation of the corresponding control parameters have been discussed in next. These rules include the theorem and proof. The proof section has been dealt with the concept of Lyapunov based adaptation technique to verify the adaptive theorems and prove the system stability criteria.

(I) ***Adaptive rules for FSMC***

Theorem: For the nonlinear dynamic system (2.9a) to (2.9c) and FSMC controller (2.12a), (2.13), (2.14a), (2.14b), (2.15a) and (2.15c) involving the corresponding error e, a small positive error e_δ and the sliding surface (2.11b), the set of robust and convergent adaptive rules can be written as

$$\dot{\hat{\alpha}}_b = \text{Proj}\ (\hat{\alpha}_b, y_b)\ \text{ for } |e| > e_\delta, \tag{2.18a}$$

$$\dot{\hat{\alpha}}_{fi} = \text{Proj}\ (\hat{\alpha}_{fi}, y_{fi})\ \text{ for } |e| > e_\delta, \tag{2.18b}$$

$$\dot{\hat{\beta}}_i = \text{Proj}\ (\hat{\beta}_i, y_{\beta i})\ \text{ for } |e| > e_\delta, \tag{2.18c}$$

$$\dot{\hat{c}}_i = \text{Proj}\ (\hat{c}_i, y_{ci})\ \text{ for } |e| > e_\delta, \tag{2.18d}$$

$$\dot{\hat{\alpha}}_{s,\,\text{FSMC}} = \text{Proj}\ (\hat{\alpha}_{s,\,\text{FSMC}}, y_{s,\,\text{FSMC}})\ \text{ for } |e| > e_\delta, \tag{2.18e}$$

$$\dot{\hat{\alpha}}_b = \dot{\hat{\alpha}}_{fi} = \dot{\hat{\beta}}_i = \dot{\hat{c}}_i = \dot{\hat{\alpha}}_{s,\,\text{FSMC}} = 0\ \text{ for } |e| \le e_\delta, \tag{2.18f}$$

$$\text{and } \dot{\hat{u}}_{s,\text{FSMC}} = 0\ \text{ for } |e| \le e_\delta, \tag{2.18g}$$

$$\text{where } y_b = \gamma_b s \tanh(\beta_b e), \tag{2.18h}$$

$$y_{fi} = \gamma_f s \hat{\xi}_{fi}, \tag{2.18i}$$

$$y_{\beta i} = \gamma_\beta s \hat{d}_{\beta i} \hat{\alpha}_{fi}, \tag{2.18j}$$

$$y_{ci} = \gamma_c s \hat{d}_{ci} \hat{\alpha}_{fi}, \tag{2.18k}$$

$$y_{s,\,\text{FSMC}} = \gamma_{s,\,\text{FSMC}} |s|, \tag{2.18l}$$

$$\text{Proj}(\hat{\alpha}_b, y_b) = \begin{cases} 0, \text{if } \hat{\alpha}_b = \hat{\alpha}_{b,\max} \vee y_b > 0 \\ 0, \text{if } \hat{\alpha}_b = \hat{\alpha}_{b,\min} \vee y_b < 0 \\ \text{else } y_b \end{cases}, \tag{2.18m}$$

$$\text{Proj}(\hat{\alpha}_{fi}, y_{fi}) = \begin{cases} 0, \text{if } \hat{\alpha}_{fi} = \hat{\alpha}_{fi,\max} \vee y_{fi} > 0 \\ 0, \text{if } \hat{\alpha}_{fi} = \hat{\alpha}_{fi,\min} \vee y_{fi} < 0 \\ \text{else } y_{fi} \end{cases}, \tag{2.18n}$$

$$\text{Proj}(\hat{\beta}_i, y_{\beta i}) = \begin{cases} 0, \text{if } \hat{\beta}_i = \beta_{i,\max} \vee y_{\beta i} > 0 \\ 0, \text{if } \hat{\beta}_i = \beta_{i,\min} \vee y_{\beta i} < 0 \\ \text{else } y_{\beta i} \end{cases}, \tag{2.18o}$$

$$\text{Proj}(\hat{c}_i, y_{ci}) = \begin{cases} 0, \text{if } \hat{c}_i = c_{i,\max} \vee y_{ci} > 0 \\ 0, \text{if } \hat{c}_i = c_{i,\min} \vee y_{ci} < 0 \\ \text{else } y_{ci} \end{cases}, \tag{2.18p}$$

$$\text{and } \text{Proj}(\hat{\alpha}_s, y_{s,\text{FSMC}}) = \begin{cases} 0, \text{if } \hat{\alpha}_{s,\text{FSMC}} = \hat{\alpha}_{s,\text{FSMC,max}} \\ \text{else } y_{s,\text{FSMC}} \end{cases}, \tag{2.18q}$$

$$\text{where } \hat{d}_{\beta i} = (\partial u_f / \partial \beta_i)|_{\hat{\beta}_i}, \tag{2.18r}$$

$$\text{and } \hat{d}_{ci} = (\partial u_f / \partial c_i)|_{\hat{c}_i}. \tag{2.18s}$$

γ_b, γ_f, γ_β, γ_c and $\gamma_{s,\text{FSMC}}$ are the rate parameters for the corresponding control parameters of $\hat{\psi}_{\text{FSMC}}$ and these rate parameters have been considered as positive value because the sign of the adaptation rates of (2.18h) to (2.18l) only dependable to the sign of s. A dot over any parameter before any equal to sign in (2.18a) to (2.18g) is the adaptive rate of the parameter.

The corresponding rate parameters and large positive parameter β_b can be treated as fixed parameters which can be expressed as

$$\text{f}_{\text{FSMC}} = (\gamma_b \;\; \gamma_f \;\; \gamma_\beta \;\; \gamma_c \;\; \gamma_{s,\text{FSMC}} \;\; \beta_b). \tag{2.18t}$$

The projection operators (Su et al., 2000; Hu et al., 2011) in (2.18m-q) suspend the adaptation, if (2.18h) to (2.18l) indicate a parameter going beyond its corresponding specified range. Another condition of postponed adaptation arises in case the tracking error satisfies the condition mentioned in (2.18f) together with holding of sliding-mode contribution in (2.18g). Even after the convergence of the error within a small bound, the filtered variable (2.11b) could oscillate about a finite value caused by the disturbances in a real system. Of course, the undesired growth of the parameters is kept in check by the conditional use of (2.18f) instead of (2.18h) to (2.18l).

The max and min subscripts in (2.18m-q) are respectively designate the maximum and minimum limits of those corresponding parameters and the adaptive scheme has been contained within those limit values. These maximum and minimum controller parameters can be represented in terms of the corresponding upper and lower limit of the estimated controller parameters respectively as

$$\hat{\psi}_{\text{FSMC}}(\text{upper}) = \max(\hat{\alpha}_b \quad \hat{\alpha}_{fi} \quad \hat{\beta}_i \quad \hat{c}_i \quad \hat{\alpha}_{s,\text{FSMC}}), \tag{2.18u}$$

$$\text{and } \hat{\psi}_{\text{FSMC}}(\text{lower}) = \min(\hat{\alpha}_b \quad \hat{\alpha}_{fi} \quad \hat{\beta}_i \quad \hat{c}_i \quad \hat{\alpha}_{s,\text{FSMC}}). \tag{2.18v}$$

The respective updating of the controller parameters starting from their corresponding initial values which can be again represented in terms of the estimated controller parameters as

$$\hat{\psi}_{\text{FSMC}}(\text{initial}) = \text{initial}(\hat{\alpha}_b \quad \hat{\alpha}_{fi} \quad \hat{\beta}_i \quad \hat{c}_i \quad \hat{\alpha}_{s,\text{FSMC}}). \tag{2.18w}$$

The necessary proof of the above mentioned adaptive theorems has been discussed in next.

***Proof*:** The corresponding parameters of $\hat{\psi}_{\text{FSMC}}$ can be represented at the current time step t and these parameters $\hat{\alpha}_b|_t$, $\hat{\alpha}_{fi}|_t$, $\hat{\beta}_i\big|_t$, $\hat{c}_i\big|_t$ and $\hat{\alpha}_{s,\text{FSMC}}|_t$ specifically signify the current estimated parameter vector as $\hat{\psi}_{\text{FSMC}}|_t$. Consistent with the current estimation of the controller parameters, the converged estimate and the estimation errors can be expressed respectively as

$$\psi^*_{\text{FSMC}} = \hat{\psi}_{\text{FSMC}}|_t + \delta\hat{\psi}_{\text{FSMC}}, \tag{2.19a}$$

$$\text{and } \tilde{\psi}_{\text{FSMC}} = \psi_{\text{FSMC}} - \hat{\psi}_{\text{FSMC}}. \tag{2.19b}$$

with the last term in (2.19a) in the limit satisfying

$$\delta\hat{\psi}_{\text{FSMC}}\big|_{\delta d \to 0} \to 0. \tag{2.19c}$$

Now, applying (2.19c) regarding the current estimation error (2.19b), the Taylor series expansion of $\hat{u}_b$ can be obtained as

$$\Delta_b = (\partial\hat{u}_b / \partial\hat{\alpha}_b)(\hat{\alpha}_b|_{t+1} - \hat{\alpha}_b|_t) = \tilde{\alpha}_b \tanh(\beta_b e) + o(\Delta_b) + O(\delta\hat{\psi}_{\text{FSMC}}), \tag{2.20a}$$

with $o(\Delta_b)$ and $O(\delta\hat{\psi}_{\text{FSMC}})$ respectively denoting higher order terms negligible and comparable with respect to the ones in the arguments.

Similarly $\hat{u}_f$ can be achieved as

$$\Delta_f = \sum_{i=1}^{M}\{\hat{\alpha}_{fi}(\hat{d}_{\beta i}\tilde{\beta}_i + \hat{d}_{ci}\tilde{c}_i) + \hat{\xi}_{fi}\tilde{\alpha}_{fi}\} + o(\Delta_f) + O(\delta\hat{\psi}_{\text{FSMC}}). \tag{2.20b}$$

Now, using (2.12a), (2.19a), (2.20a) and (2.20b), (2.11a) can be rewritten as

$$\dot{s} = \tilde{\alpha}_b \tanh(\beta_b e) + \sum_{i=1}^{M} \{\hat{\alpha}_{fi}(\hat{d}_{\beta i}\tilde{\beta}_i + \hat{d}_{ci}\tilde{c}_i) + \hat{\xi}_{fi}\tilde{\alpha}_{fi}\} + \xi_{s,\mathrm{FSMC}} - \hat{u}_{s,\mathrm{FSMC}}, \quad (2.21)$$

since $u^*_{\mathrm{FSMC}} = \hat{u}_b + \Delta_b + \hat{u}_f + \Delta_f + \xi_{s,\mathrm{FSMC}}$, (2.22a)

and the uncertainty bound $\xi_{s,\mathrm{FSMC}} = o(\Delta_I, \Delta_f) + O(\delta\hat{\psi}_{\mathrm{FSMC}}) + \delta d$, (2.22b)

in which δd arises from (2.11a) that involves the uncertainty in $\hat{u}_{s,\mathrm{FSMC}}$ as well.

Now considering Lyapunov based stability theorem mentioned in the Section 2.4, the Lyapunov functional of a quadratic form involving sliding surface s and the adaptive parameters of $\hat{\psi}_{\mathrm{FSMC}}$ can be defined as

$$L_{\mathrm{FSMC}} = [s^2 + \tilde{\alpha}_b^2/\gamma_b + \sum_{i=1}^{M}(\tilde{\alpha}_{fi}^2/\gamma_f + \tilde{\beta}_i^2/\gamma_\beta + \tilde{c}_i^2/\gamma_c) + \tilde{\alpha}_{s,\mathrm{FSMC}}^2/\gamma_{s,\mathrm{FSMC}}]/2, \quad (2.23a)$$

and differentiating of above Lyapunov function (2.23a) and using(2.21), it can be obtained that

$$\dot{L}_{\mathrm{FSMC}} = s[\tilde{\alpha}_b \tanh(\beta_b e) + \sum_{i=1}^{M}\{\hat{\alpha}_{fi}(\hat{d}_{\beta i}\tilde{\beta}_i + \hat{d}_{ci}\tilde{c}_i) + \hat{\xi}_{fi}\tilde{\alpha}_{fi}\} + \xi_{\mathrm{FSMC}} - \hat{u}_{s,\mathrm{FSMC}}] + \tilde{\alpha}_b\dot{\tilde{\alpha}}_b/\gamma_b + \sum_{i=1}^{M}(\tilde{\alpha}_{fi}\dot{\tilde{\alpha}}_{fi}/\gamma_f + \tilde{\beta}_i\dot{\tilde{\beta}}_i/\gamma_\beta + \tilde{c}_i\dot{\tilde{c}}_i/\gamma_c) + \tilde{\alpha}_{s,\mathrm{FSMC}}\dot{\tilde{\alpha}}_{s,\mathrm{FSMC}}/\gamma_{s,\mathrm{FSMC}}, \quad (2.23b)$$

which can be further rewritten with help of (2.15a) and (2.19b) as

$$\dot{L}_{\mathrm{FSMC}} = s[\tilde{\alpha}_b \tanh(\beta_b e) + \sum_{i=1}^{M}\{\hat{\alpha}_{fi}(\hat{d}_{\beta i}\tilde{\beta}_i + \hat{d}_{ci}\tilde{c}_i) + \hat{\xi}_{fi}\tilde{\alpha}_{fi}\} + \xi_{\mathrm{FSMC}} - \alpha_{s,\mathrm{FSMC}}\mathrm{sgn}(s) + \tilde{\alpha}_{s,\mathrm{FSMC}}\,\mathrm{sgn}(s)] + \tilde{\alpha}_b\dot{\tilde{\alpha}}_b/\gamma_b + \sum_{i=1}^{M}(\tilde{\alpha}_{fi}\dot{\tilde{\alpha}}_{fi}/\gamma_f + \tilde{\beta}_i\dot{\tilde{\beta}}_i/\gamma_\beta + \tilde{c}_i\dot{\tilde{c}}_i/\gamma_c) + \tilde{\alpha}_{s,\mathrm{FSMC}}\,\dot{\tilde{\alpha}}_{s,\mathrm{FSMC}}/\gamma_{s,\mathrm{FSMC}}. \quad (2.23c)$$

If either tracking error (2.10b) not small or the controller parameters not saturated through the projection operators (2.18m) to (2.18q), then in a manner detailed in Shahnazi et al. (2008) (2.18a) to (2.18e), (2.19b) and (2.23c) together yield

$$\dot{L}_{\mathrm{FSMC}} = s\xi_{s,\mathrm{FSMC}} - s\alpha_{s,\mathrm{FSMC}}\,\mathrm{sgn}(s), \quad (2.24a)$$

which can be rewritten as negative semi-definite by implementing the unknown bound concept of (2.15c)

$$\dot{L}_{\mathrm{FSMC}} = -(|s|\alpha_{s,\mathrm{FSMC}} - s\xi_{s,\mathrm{FSMC}}) \le 0. \quad (2.24b)$$

Now, the above equation can be written in terms of its negative semi-definiteness form as $\int_o^t(-\dot{L}_{\mathrm{FSMC}})d\tau \ge 0$, (2.24c)

and expanding the left side of (2.24c), it can be achieved that

$$L_{\mathrm{FSMC}}|_{t=0} - L_{\mathrm{FSMC}}|_t \ge 0. \quad (2.24d)$$

Of course, $L_{\text{FSMC}}|_{t=0}$ and $L_{\text{FSMC}}|_t$ both have positive and finite value in view of Lyapunov based quadratic form of the right hand side of (2.23a). Since $L_{\text{FSMC}}|_{t=0}$ is finite prior to the controller initiation, (2.24d) guarantees finiteness of $L_{\text{FSMC}}|_t$ as well. Their finiteness and positivity allow (2.24c) to be expressed as

$$\lim_{t\to\infty}\int_o^t |\dot{L}_{\text{FSMC}}|\, d\tau < \infty . \tag{2.24e}$$

Now (2.23a), (2.24b) and (2.24e) together with Barbalat's lemma, yield $\lim_{t\to\infty}\dot{L}_{\text{FSMC}} = 0$ and in turn leads to $\lim_{t\to\infty}|s| = 0$ in view of (2.24b). The last inference and (2.11a) together yield

$$\lim_{t\to\infty} e = 0 . \tag{2.24f}$$

With help (2.24f), it can be established that proposed adaptation scheme of FSMC comprised of (2.18a) to (2.18e) and (2.18h) to (2.18q) as convergent.

(II) ***Adaptive rules for SMIC***

The adaptive rules including the adaptive theorem and their corresponding proof for SMIC have been deliberated in next.

Theorem: For the nonlinear system (2.9a) to (2.9c) involving the tracking error and the sliding surface in (2.11b) the convergent and robust adaptive rules of the respective controller (2.12b), (2.15b), (2.15d) and (2.16) can be expressed as

$$\dot{\hat{\alpha}}_I = \text{Proj}\ (\hat{\alpha}_I, y_I)\ \text{ for } |e| > e_\delta , \tag{2.25a}$$

$$\dot{\hat{\alpha}}_{s,\text{SMIC}} = \text{Proj}\ (\hat{\alpha}_{s,\text{SMIC}}, y_{s,\text{SMIC}})\ \text{ for } |e| > e_\delta , \tag{2.25b}$$

$$\dot{\hat{\alpha}}_I = \dot{\hat{\alpha}}_{s,\text{SMIC}} = 0\ \text{ for } |e| \le e_\delta , \tag{2.25c}$$

$$\text{and } \dot{\hat{u}}_{s,\text{SMIC}} = 0 \text{ for } |e| \le e_\delta , \tag{2.25d}$$

$$\text{where } y_I = \gamma_I s \tanh(\beta_I \int s dt) , \tag{2.25e}$$

$$y_{s,\text{SMIC}} = \gamma_{s,\text{SMIC}} |s| , \tag{2.25f}$$

$$\text{Proj}(\hat{\alpha}_I, y_I) = \begin{cases} 0, \text{if } \hat{\alpha}_I = \hat{\alpha}_{I,\max} \vee y_I > 0 \\ 0, \text{if } \hat{\alpha}_I = \hat{\alpha}_{I,\min} \vee y_I < 0 \\ \text{else } y_I \end{cases} , \tag{2.25g}$$

$$\text{Proj}(\hat{\alpha}_{s,\text{SMIC}}, y_{s,\text{SMIC}}) = \begin{cases} 0, \text{if } \hat{\alpha}_{s,\text{SMIC}} = \hat{\alpha}_{s,\text{SMIC,max}} \\ \text{else } y_{s,\text{SMIC}} \end{cases}, \tag{2.25h}$$

with the respective positive rate parameters of γ_I and $\gamma_{s,\text{SMIC}}$ for the corresponding controller parameters in $\hat{\psi}_{\text{SMIC}}$.

Now similar to FSMC, the corresponding rate parameters and large positive parameter β_I can be expressed in terms of fixed parameters as

$$\text{f}_{\text{SMIC}} = (\gamma_I \quad \gamma_{s,\text{SMIC}} \quad \beta_I). \tag{2.25i}$$

The maximum and minimum values of the adaptive parameters comprises the upper and lower limits of their respective values which can be expressed respectively as

$$\hat{\psi}_{\text{SMIC}}(\text{upper}) = \max(\hat{\alpha}_I \quad \hat{\alpha}_{s,\text{SMIC}}), \tag{2.25j}$$

and $$\hat{\psi}_{\text{SMIC}}(\text{lower}) = \min(\hat{\alpha}_I \quad \hat{\alpha}_{s,\text{SMIC}}). \tag{2.25k}$$

The controller parameters can be updated within the above mentioned limits and the updating starts from the respective initial value which can be represented as

$$\hat{\psi}_{\text{SMIC}}(\text{initial}) = \text{initial}(\hat{\alpha}_I \quad \hat{\alpha}_{s,\text{SMIC}}). \tag{2.25l}$$

The necessary proof of the adaptive theorems has been discussed in next.

***Proof*:** The estimates $\hat{\alpha}_I|_t$ and $\hat{\alpha}_{s,\text{SMIC}}|_t$ of SMIC generically constructs $\hat{\psi}_{\text{SMIC}}|_t$ at the current time step t. The converged estimates and the estimation errors can be expressed respectively as

$$\psi^*_{\text{SMIC}} = \hat{\psi}_{\text{SMIC}}|_t + \delta\hat{\psi}_{\text{SMIC}}, \tag{2.26a}$$

and $$\tilde{\psi}_{\text{SMIC}} = \psi_{\text{SMIC}} - \hat{\psi}_{\text{SMIC}}. \tag{2.26b}$$

with the last term in (2.26a) in the limit satisfying $\delta\hat{\psi}_{\text{SMIC}}\big|_{\delta d \to 0} \to 0$. (2.26c)

Now implementing (2.26b), the first-order term of the Taylor series expansion of the integral controller (2.16) can be achieved as

$$\Delta_I = (\partial\hat{u}_I / \partial\hat{\alpha}_I)(\hat{\alpha}_I|_{t+1} - \hat{\alpha}_I|_t) = \tilde{\alpha}_I \tanh(\beta_I \int sdt) + o(\Delta_I) + O(\delta\hat{\psi}_{\text{SMIC}}). \tag{2.27}$$

Now, using (2.12b), (2.26a) and (2.27), (2.11a) is rewritten as

$$\dot{s} = \tilde{\alpha}_I \tanh(\beta_I \int sdt) + \xi_{s,\text{SMIC}} - \hat{u}_{s,\text{SMIC}}, \tag{2.28}$$

since $$u^*_{\text{SMIC}} = \hat{u}_I + \Delta_I + \xi_{\text{SMIC}}, \tag{2.29a}$$

and the uncertainty bound $$\xi_{s,\text{SMIC}} = o(\Delta_I) + O(\delta\tilde{\psi}_{\text{SMIC}}) + \delta d, \tag{2.29b}$$

in which δd arises from (2.11a) that involves uncertainty in $\hat{u}_{s,\text{SMIC}}$ as well.

Similar to FSMC, one quadratic Lyapunov based function has been constructed for SMIC in term of s and controller parameters in $\hat{\psi}_{\text{SMIC}}$. The quadratic Lyapunov functional has been defined here as

$$L_{\text{SMIC}} = (s^2 + \tilde{\alpha}_I^2 / \gamma_I + \tilde{\alpha}_{s,\text{SMIC}}^2 / \gamma_{s,\text{SMIC}}) / 2 , \tag{2.30a}$$

which has been differentiated and rearranged using (2.28) as

$$\dot{L}_{\text{SMIC}} = s\,[\tilde{\alpha}_I \tanh(\beta_I \int s dt) + \xi_{\text{SMIC}} - \hat{u}_{s,\text{SMIC}}] + \tilde{\alpha}_I \dot{\tilde{\alpha}}_I / \gamma_I + \tilde{\alpha}_{s,\text{SMIC}}\, \dot{\tilde{\alpha}}_{s,\text{SMIC}} / \gamma_{s,\text{SMIC}} , \tag{2.30b}$$

that can be further rewritten with help of (2.15b) and (2.26a) as

$$\dot{L}_{\text{SMIC}} = s\,[\tilde{\alpha}_I \tanh(\beta_I \int s dt) + \xi_{\text{SMIC}} - \alpha_{s,\text{SMIC}} \text{sgn}(s) + \tilde{\alpha}_{s,\text{SMIC}} \text{sgn}(s)] + \tilde{\alpha}_I \dot{\tilde{\alpha}}_I / \gamma_I + \tilde{\alpha}_{s,\text{SMIC}} \dot{\tilde{\alpha}}_{s,\text{SMIC}} / \gamma_{s,\text{SMIC}} . \tag{2.30c}$$

A modified form of (2.30c) can be written using (2.25a), (2.25b) and (2.26b) in the manner detailed in Shahnazi et al. (2008) as

$$\dot{L}_{\text{SMIC}} = s\xi_{\text{SMIC}} - s\alpha_{s,\text{SMIC}} \text{sgn}(s) , \tag{2.31a}$$

considering either the tracking error not small or the controller parameters of SMIC not saturated through the proposed projection operators of (2.25g) and (2.25h). With help of (2.15d), the last equation can be again rearranged as

$$\dot{L}_{\text{SMIC}} = -(|s|\alpha_{s,\text{SMIC}} - s\xi_{s,\text{SMIC}}) \le 0 , \tag{2.31b}$$

which is basically treated as negative semi-definite.

Now, writing the negative semi-definiteness form of (2.31b) as

$$\int_o^t (-\dot{L}_{\text{SMIC}}) d\tau \ge 0 , \tag{2.31c}$$

and expanding the left side of this equation it can be found that

$$L_{\text{SMIC}}|_{t=0} - L_{\text{SMIC}}|_t \ge 0 . \tag{2.31d}$$

Each term of the right side of (2.31d) is positive and finite in view of the quadratic form of the right hand side of (2.30a). Since $L_{\text{SMIC}}|_{t=0}$ is finite prior to the controller initiation, (2.31d) guarantees finiteness of $L_{\text{SMIC}}|_t$ as well. Their finiteness and positivity allow (2.31c) to be expressed as

$$\lim_{t\to\infty} \int_o^t |\dot{L}_{\text{SMIC}}| d\tau < \infty . \tag{2.31e}$$

Hence, (2.30a), (2.31b) and (2.31e) together with Barbalat's lemma, yield $\lim_{t\to\infty}\dot{L}_{\text{SMIC}}=0$ and in turn leads to $\lim_{t\to\infty}|s|=0$ in view of (2.31b). The last inference and (2.11a) together yield

$$\lim_{t\to\infty}e=0, \tag{2.31f}$$

and this equation establishes the proposed adaptation scheme for SMIC comprised of (2.25a), (2.25b) and (2.25e) to (2.25h) as convergent.

A simple numerical simulation exercise for each of FSMC and SMIC presented in the next section with reference to Figs. 2.4 to 2.6 clearly reveal the corresponding adaptive rules.

2.5 Numerical simulations for FSMC and SMIC

For the purpose of numerical simulations of FSMC and SMIC, a non-dimensional 2nd order dynamic system has been considered with a sinusoidal demand x_d in terms of amplitude *a* and the frequency *f* for the time *t* as

$$x_d=a\sin(2\pi f t), \tag{2.32a}$$

and disturbance d containing $0<\text{rand}(0,1)<1$ as

$$d=\ddot{x}_d+\lambda_1\dot{e}+\lambda_0 e+b\sin\{2\pi f\ \text{rand}(0,1)\}. \tag{2.32b}$$

Now, the corresponding sliding variable $\dot{s}$ and s for the 2nd order dynamic system can be written with help of (2.11a-b) respectively as

$$\dot{s}=u+d, \tag{2.32c}$$

$$\text{and } s=\dot{e}+\lambda_1 e+\lambda_0\int e dt, \tag{2.32d}$$

where λ_1 and λ_0 are the Routh coefficients which can be expressed in terms of the vector form of Hurwirtz coefficient as

$$\lambda=(\lambda_1\ \ \lambda_0). \tag{2.32e}$$

For the numerical study, the corresponding values of upper limit, lower limit, initial and the fixed values have been chosen as suitable for representation. For an abundant discussion of each numerical study, three cases have been studied with a PID-type sliding variable (Xu, 2017) with $x|_{t=0}=a$, f =1 and b =10 for each of the cases and *a* = 1 for Cases 1 and 3 while Case 2 with *a* = 0.5. The values of fixed parameters have been considered as same for each case. The Hurwirtz coefficients have been

considered as same for Cases 1 and 3. The initial values for the corresponding adaptive parameters have been considered as same for Cases 2 and 3.

Hurwirtz coefficients have been chosen for both of FSMC and SMIC as

$\lambda = (1\ 1)$ for Cases 1 and 3, (2.33a)

and $\lambda = (2\ 0.5)$ for Case 2. (2.33b)

The other parameters have been mentioned in the corresponding numerical studies in next.

2.5.1 Numerical studies for FSMC

The numerical study of FSMC has been presented in Figs. 2.4 and 2.6 for validation of the adaptive formulations mentioned in (2.18a-s). For study of each case, the parameters of $\hat{\psi}_{\text{FSMC}}(\text{upper})$ and $\hat{\psi}_{\text{FSMC}}(\text{lower})$ have been chosen respectively as

$$\hat{\psi}_{\text{FSMC}}(\text{upper}) = (10\ 10\ 10\ 10\ 10\ 10\ 1\ 1\ 1\ 1\ 1\ 6\ 6\ 6\ 6\ 6\ 100), \quad (2.34a)$$

and $\hat{\psi}_{\text{FSMC}}(\text{lower}) = (0.01\ 0.01\ 0.01\ 0.01\ 0.01\ 0.01\ 0\ 0\ 0\ 0\ 0$

$$-1\ -1\ -1\ -1\ -1\ 1), \quad (2.34b)$$

considering the fuzzy controller with five rules in the rule base for $\hat{\xi}_{fi}$.

The corresponding parameters in $\hat{\psi}_{\text{FSMC}}(\text{initial})$ have been chosen as

$\hat{\psi}_{\text{FSMC}}(\text{initial}) = (1\ 1\ 1\ 1\ 1\ 1\ 0.7\ 0.4\ 0.3\ 0.1\ 0.01\ 0\ 1\ 2\ 3\ 4\ 1)$ for Case1, (2.34c)

and $\hat{\psi}_{\text{FSMC}}(\text{initial}) = (0.5\ 2\ 2\ 2\ 2\ 2\ 0.1\ 0.2\ 0.3\ 0.4\ 0.5\ -1\ 0.2\ 1\ 2\ 3\ 10)$

for Cases 2 and 3. (2.34d)

Fixed parameters in f_{FSMC} for each case have been taken as

$$\text{f}_{\text{FSMC}} = (1\ 10\ 0.1\ 1\ 100\ 20000). \quad (2.34e)$$

Fig. 2.4(b) depicts the adaption of $\hat{\alpha}_b$ and $\hat{\alpha}_{s,\text{FSMC}}$ and Fig. 2.5 represents the adaptation of $\hat{\alpha}_f$ for the same error mentioned in Fig. 2.4(a). Figs. 2.4(a) and (b) respectively show the progression of the error and the parameters in time with no markings for Case 3 and with subscripts 1 and 2 to *g* to *l* for Cases 1 and 2. Though marking for Case 3 for adaptation of $\hat{\alpha}_f$ has been given in Fig. 2.5. In each case, Fig. 2.4(a) shows the small bound $\pm e_\delta$. Figs. 2.4 and 2.5 show active adaptations from *g* to *h*, the latter lying at the lower bound of $\pm e_\delta$. Each adaptation then remains suspended up to the instant of the error reaching the upper bound at *i*. Thereafter, the

adaptations have resumed from the respective last updated values and pass through the next active phase between *i* and *j*. It is evident that each adaptation remains active in intervals *g*-*h*, *i*-*j* and *k*-*l* for $|e| \equiv |x_d - x| > e_\delta$ and remains suspended between *h*-*i* and *j*-*k* for $e \le \pm e_\delta$. The observed monotonic increase of $\hat{\alpha}_{s,\text{FSMC}}$ and oscillation of $\hat{\alpha}_b$ are consistent with (2.18l) and (2.18h) respectively. These forms along with close variations of error rates for Cases 1 and 3 explain rates of adaptation $\hat{\alpha}$ s to remain almost unaffected by the choices of λ s. However, different initial errors for Cases 1 and 2 have justifiably altered all three rates.

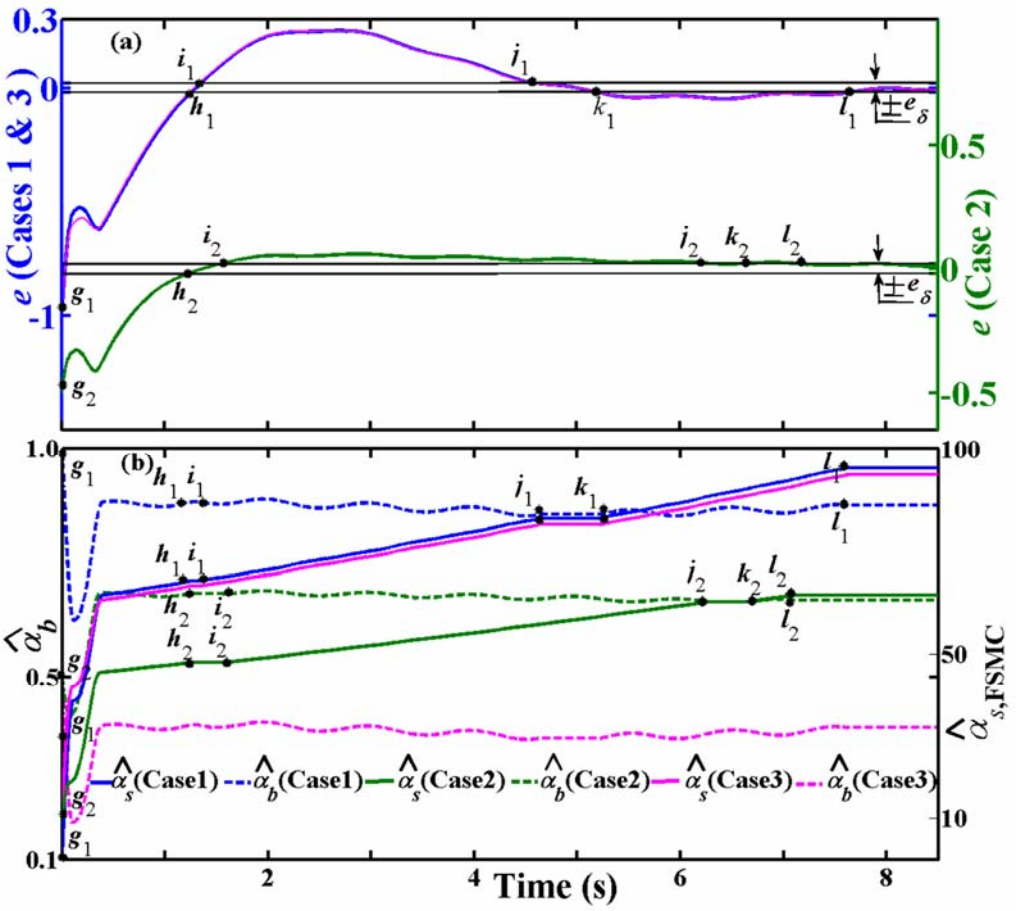

Figure 2.4: A simple numerical simulation exercise of FSMC for $\hat{\alpha}_b$ and $\hat{\alpha}_{s,\text{FSMC}}$ with different cases.

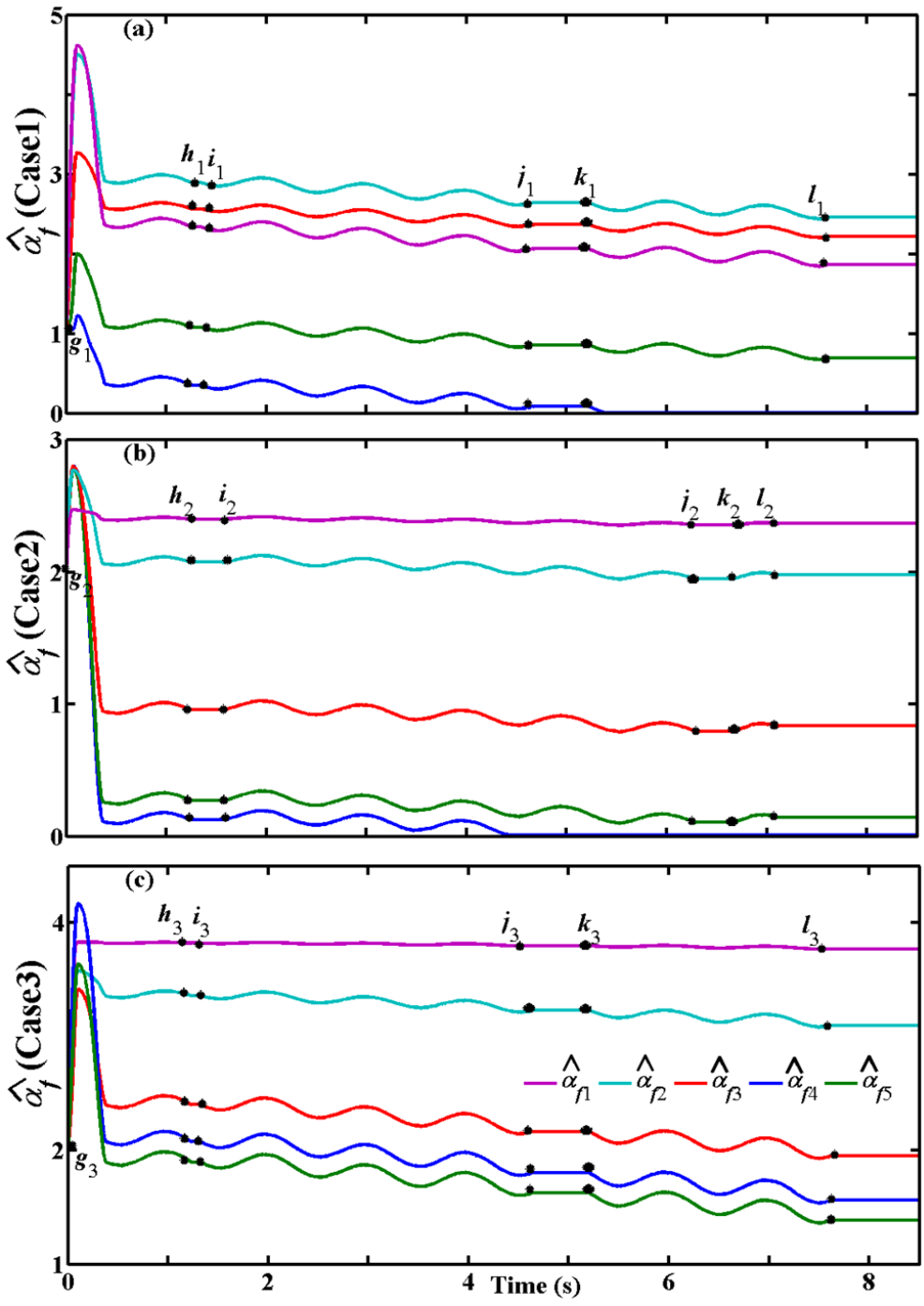

Figure 2.5: A simple numerical simulation exercise of FSMC for $\hat{\alpha}_f$ with different cases for corresponding error in Fig. 2.4(a).

2.5.2 Numerical studies for SMIC

The numerical study of SMIC has been presented in Fig. 2.6 for validation of the adaptive formulations mentioned in (2.25a-h). The corresponding parameters of $\hat{\psi}_{SMIC}(\text{upper})$ and $\hat{\psi}_{SMIC}(\text{lower})$ have been chosen respectively as

$$\hat{\psi}_{SMIC}(\text{upper}) = (10\ \ 100), \tag{2.35a}$$

$$\text{and } \hat{\psi}_{SMIC}(\text{lower}) = (0.01\ \ 1), \tag{2.35b}$$

for the study of each case.

The corresponding parameters in $\hat{\psi}_{SMIC}(\text{initial})$ have been considered as

$$\hat{\psi}_{SMIC}(\text{initial}) = (1\ \ 1) \text{ for Case1}, \tag{2.35c}$$

$$\text{and } \hat{\psi}_{SMIC}(\text{initial}) = (0.5\ \ 10) \text{ for Cases 2 and 3.} \tag{2.35d}$$

Fixed parameters in f_{SMIC} for each case has been taken as

$$f_{SMIC} = (100\ \ 10000\ \ 20000). \tag{2.35e}$$

Similar to Fig. 2.4, the initial error has been mentioned as *p* in Fig. 2.6(a). The adaptions of parameters have been depicted in Fig. 2.6(b) with no markings for Case 3 and with subscripts 1 and 2 to *p* to *w* for Case 1 and *p* to *u* for Case 2. In each case, Fig. 2.6(a) shows the small bound $\pm e_\delta$ used in (2.25a) to (2.25d).

Fig. 2.6 shows active adaptations from *p* to *q*, the latter lying at the lower bound of $\pm e_\delta$. Each adaptation then remains suspended up to the instant of error reaching the upper bound at *r*. Thereafter, the adaptations have resumed from the respective last updated values and pass through the next active phase between *r* and *s*. It is evident that each adaptation remains active in intervals *p*-*q*, *r*-*s*, *t*-*u* and *v*-*w* for $|e| > e_\delta$ and remains suspended between *q*-*r*, *s*-*t* and *u*-*v* for $e \le \pm e_\delta$. The observed monotonic increase of $\hat{\alpha}_{s,SMIC}$ and oscillation of $\hat{\alpha}_I$ are consistent with (2.25f) and (2.25e) respectively. These forms along with close variations of error rates for Cases 1 and 3 explain rates of adaptation $\hat{\alpha}$s to remain almost unaffected by the choices of λs. However, different initial errors for Cases 1 and 2 have justifiably altered all three rates. The effect of Hurwitz coefficients has been reflected in different error pattern between Case 1 and Case 2 in Fig. 2.6(a).

The real time performances of FSMC and SMIC with linear and angular-motion EHAS have been discussed in the next chapters.

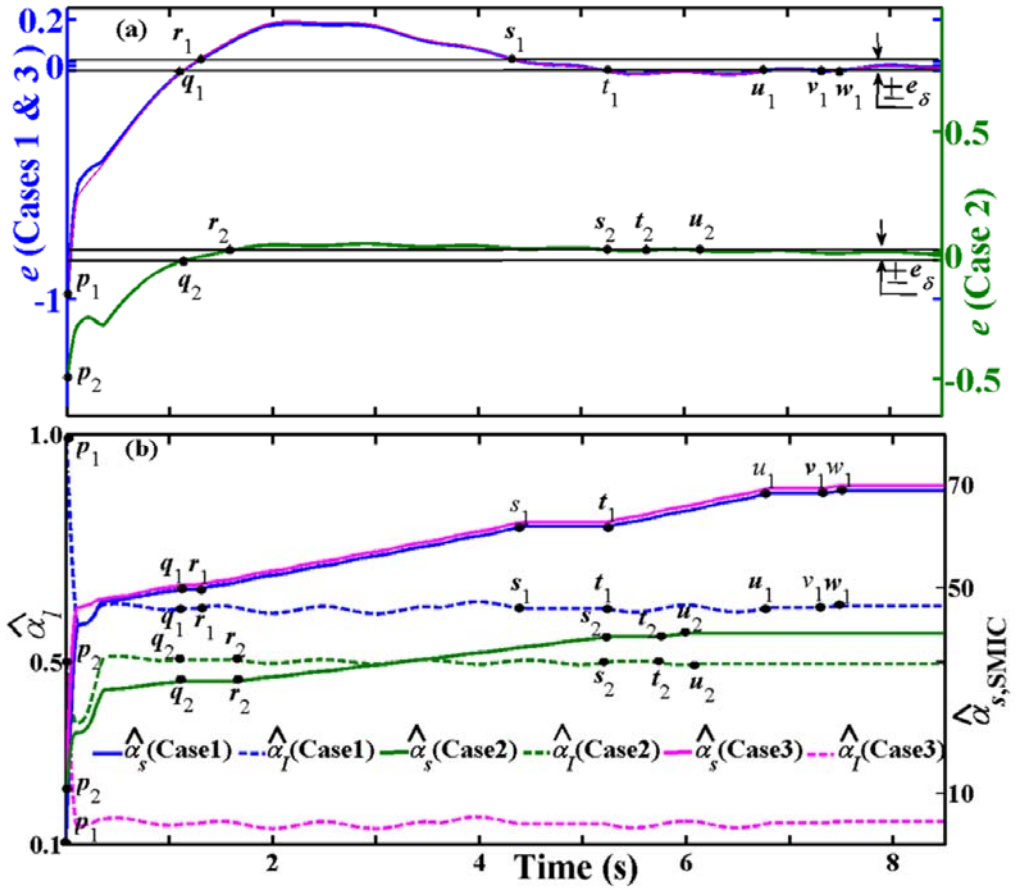

Figure 2.6: A simple numerical simulation exercises of SMIC with different cases.

2.6 Conclusions

Simple numerical analyses for application of SMC on first and second order systems have been presented in this chapter involving random disturbances. Results reveal chattering during the sliding control. Two more variants of SMC coupled with fuzzy and nonlinear integral controls along with the adaptive rules for the controller parameters have been formulated with the objective of reducing the chattering. This has been arrived at proposing a boundary layer and by retaining the SMC contribution computed while entering the layer. Since no update has been carried out within the boundary layer for the control input, the problem of chattering has got resolved as expected.

Such a suspension of adaptation of SMC parameters also means withdrawal of the robustness as well in case of adaptation of only the fuzzy parameter for FSMC. This is in view of lack of any formalism for robustness of a fuzzy controller. In order to resolve the robustness issue as well, a nonlinear integral controller has been coupled

to SMC in the proposed SMIC design. Within the boundary layer near the origin, this integral controller resembles a classical integral controller that guarantees zero steady error for a linearized system. This form is expected to perform better than FSMC for a real-life system with many uncertain issues. It worth studying this aspect through real-time implementation of these controllers.

CHAPTER 3: REAL-TIME CONTROL OF LINEAR MOTION BY EHAS

The implementations of proposed controllers, namely FSMC and SMIC, have been performed in this chapter for the real time control of an EHAS producing linear motion. This chapter deals with the description of a laboratory scaled EHAS for linear motion followed by its mathematical modeling and the corresponding controller formulation. The optimization process using RCGA has been applied for the identification of the system and controller parameters. The real time experimentation with linear motion by EHAS has been done with the optimized parameters and the best suited controller has been investigated through few experiments.

3.1 Description and component specification of EHAS for Linear Motion

The photographic view of the real time experimental set up producing the linear motion by EHAS has been depicted in Fig. 3.1 and the corresponding symbolic representation has been represented in Fig. 3.2. The experimental set up has an electric motor M to operate the hydraulic pump to feed oil in a circuit involving tank, NRV, PRV, PV and a single-rod double acting cylinder C with a piston separating right chamber Ch1 and left chamber Ch2. The effective cross sectional areas of the two chambers are A_{a1} and A_{a2} as depicted in the inset of Fig. 3.1 along with functional diagram and flow details of PV and C. The motion of the spool in PV meters the flow at ports A and B connecting ports a1 and a2 of a cylinder causing motion of its piston. The corresponding motions of the spool-land arrangement for the voltage $V \geq V_0$ and $V < -V_0$ have been depicted respectively by lines with single and double arrowheads similar to that of Fig. 1.1 in Chapter 1. The deadband voltage V_0 which can be treated here as the minimum voltage required to operate PV. The $V \geq V_0$ causes the rightward spool displacement to direct the flow between the ports P to A and B to T to sustain a leftward piston motion which has been defined here as extension of the piston. Similarly, $V < -V_0$ causes a rightward piston motion to generate the retraction motion of the piston.

The piston displacement x measured by a linear variable differential transformer LVDT and communicated to Host PC through ±10V input module IM of a real-time system RTS. The host PC receives the user defined demand of the piston x_d and

compares it with x to make the tracking error e which can be minimized with the real time control voltage V. The real time generation of V for the corresponding controller has been done in LabView-13.0.1 software by communicating with the host PC and RTS. LabView generated V has been communicated electronically through a ±10V output module OM of RTS to the integral control electronics ICE of PV. This causes the corresponding movement of the spool-land arrangement in PV and meters the flow in the actuator chambers to move the piston. There is a provision of loading the piston-rod by a compression spring S.

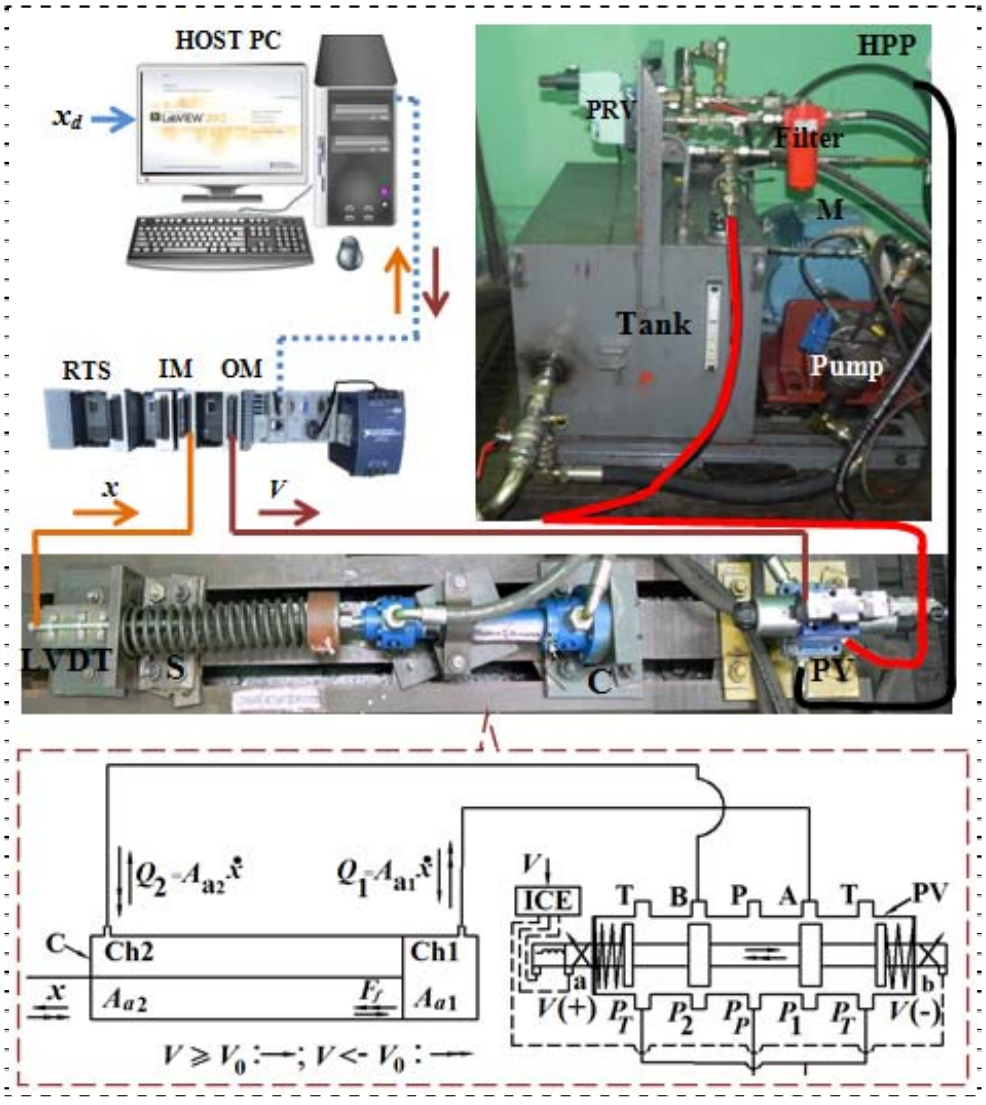

Figure 3.1: Laboratory set up for producing linear motion by an EHAS with flow details between PV and C.

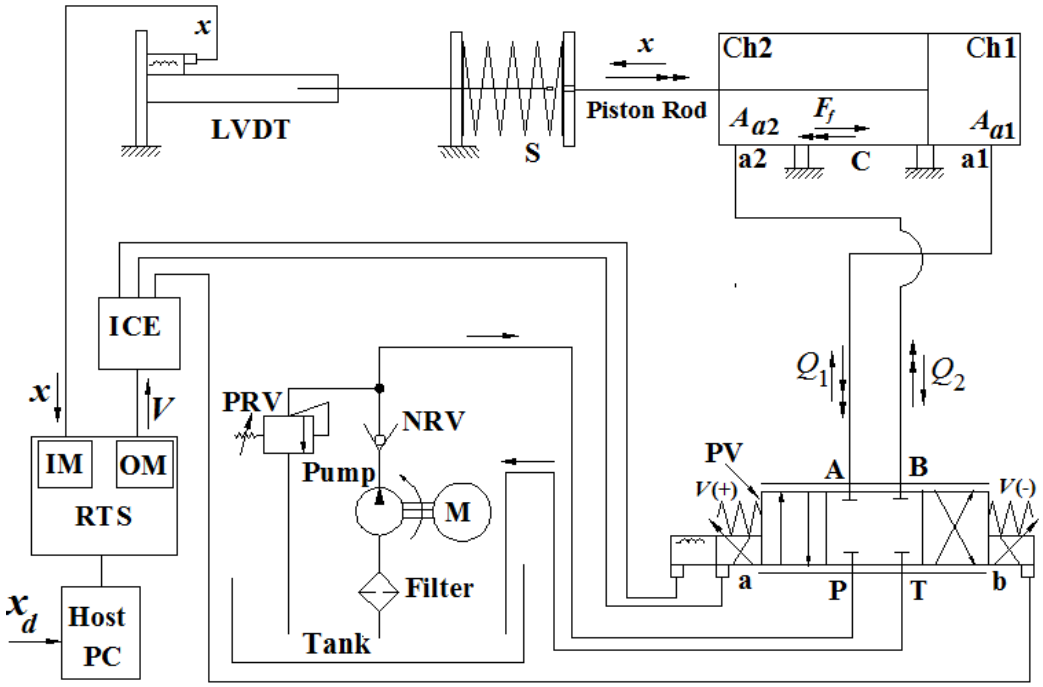

Figure 3.2: Symbolic representation of Laboratory set up for linear motion by EHAS.

From Figs. 3.1 and 3.2, it can be observed that the system encompasses the following subsystems to produce the linear motion and its real time control

1) Hydraulic Power Pack or HPP comprising of motor, pump, tank, NRV, PRV, filter and hydraulic oil,
2) Electrohydraulic cylinder-valve arrangement along with LVDT,
3) A compression spring arrangement for provision of loading to the piston-rod,
4) RTS along with IM and OM,
5) Host PC.

The subsystems have been depicted with their corresponding photographic views in Figs. 3.3 to 3.7 and their specifications have been listed out in Tables 3.1 to 3.5.

Table 3.1: Component specification of Hydraulic Power Pack (HPP)

Electric Motor	Manufacturer	ABB
	Rated Power	30 KW
	Speed	1470 rpm
	Frequency	50 Hz
Pump	Manufacturer	Rexroth
	Serial No.	A10VSO 45DR/31 R-PPA12NOO
	Type	Axial piston
	Nominal pressure	280bar
	Flow	60lpm
Pressure Relief Valve (PRV)	Manufacturer	Yuken
	Serial No.	EBG-03-H-11
	Max Pressure	245bar
Filter	Manufacturer	Hydac
	Serial No.	DFBN/HC110G10G10B1.1
	Max Pressure	420bar
Hydraulic Oil	Grade	Servosystem HLP 68
	Flash Point	210^0 C
	Pour Point	-12^0 C

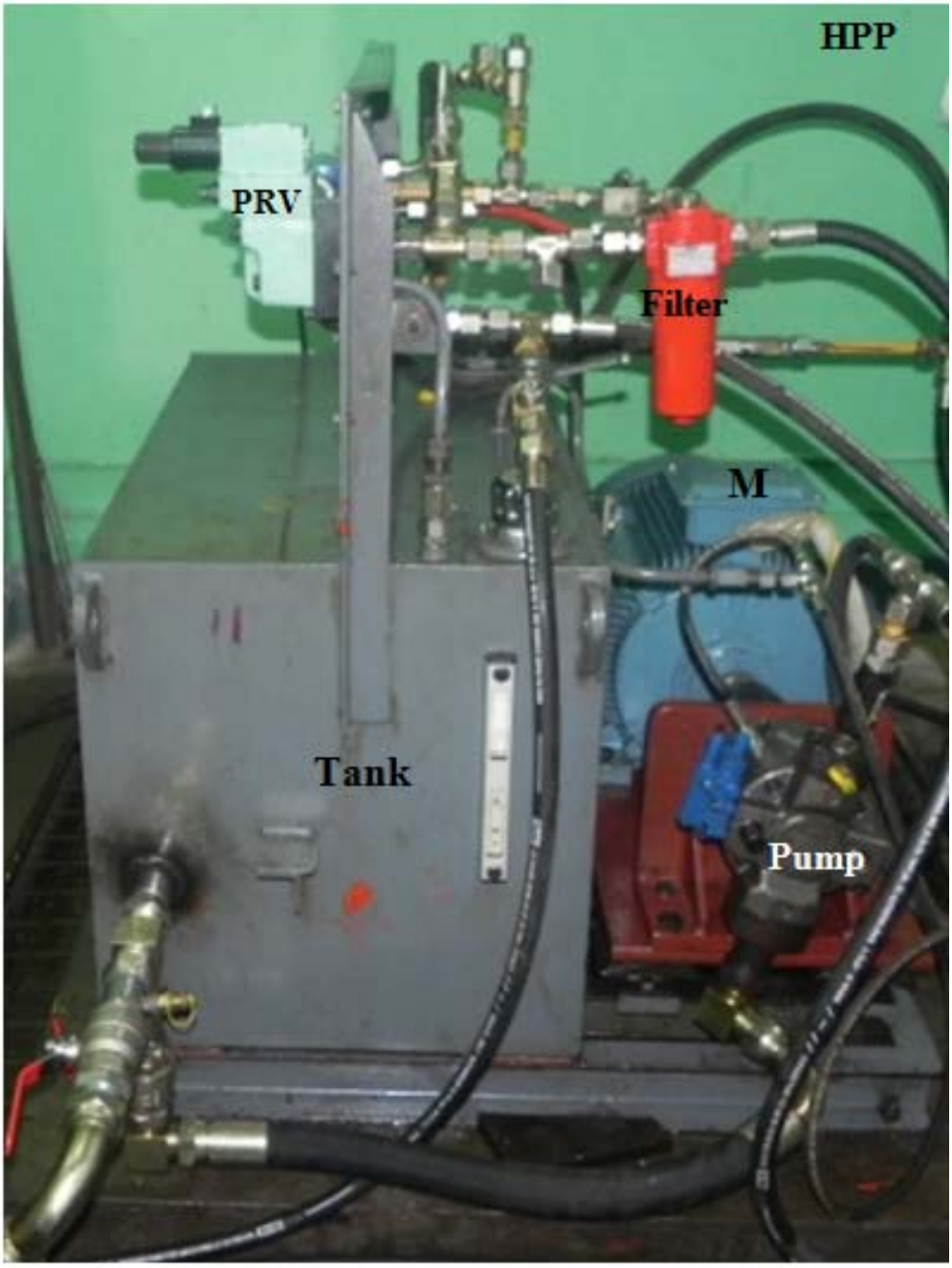

Figure 3.3: Photographic view of HPP.

Table 3.2: Component specification of Electrohydraulic System

Cylinder and piston	Manufacturer	Rexroth
	Serial No.	CD250D40/20-200A1X/01CGDHT
	Closed Length	0.45m
	Bore Diameter	ϕ 0.04m
	Rod Diameter	ϕ 0.02m
	Full Stroke	0.2m
	Piston mass	2.5 kg
Proportional Valve (PV)	Manufacturer	Rexroth
	Serial No.	4WREE 10 E50-23/G24K31/A1V
	Valve Type	Direct operated4/3 proportional directional valve with electrical position feedback and integrated electronics
	Deadband, bandwidth	Valve deadband of 10% and bandwidth of 25Hz
	Pressure rating	315 bar
	Spool Type	Mechanical centre position by solenoid return springs Centre condition: Overlap spool, causing a “dead zone” Spring offset condition: P,A,B,T blocked
	Rated flow	50 lpm at 1.0 MPa total pressure drop at 2:1 area-ratio metered ports
	Command signal	± 10volts
	Electrical connection	7-pin connector with plug
	Electrical power	24V DC amplifier supply
Linear variable differential Transformer (LVDT)	Manufacturer	HBM
	Type	WA200, Plunger
	Range	0-200mm
	Input voltage	24V DC (-15/ +20 %)
	Output voltage	0-10V DC
	Connection Type	7 pin connector
	Nominal Sensitivity	80mV/V
	Nominal output range	9.5V(0.5....10)

Figure 3.4: Photographic view of Cylinder – Piston arrangement.

Figure 3.5: Photographic view of PV.

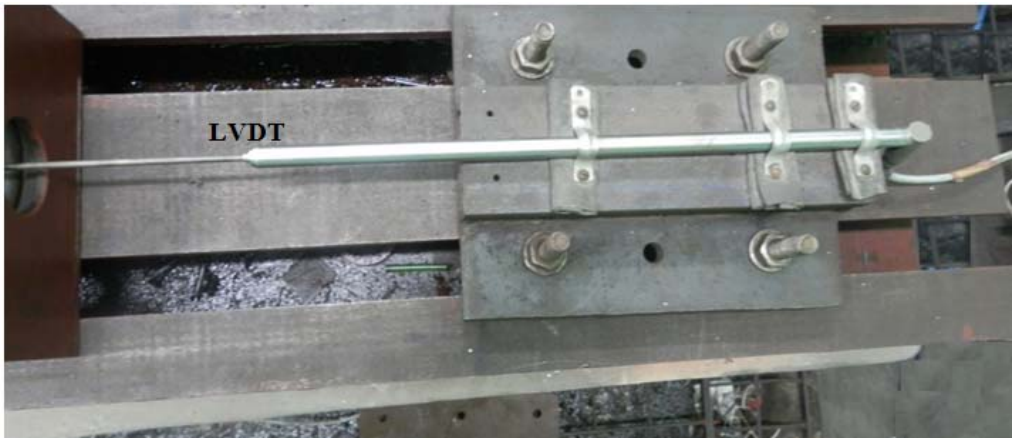

Figure 3.6: Photographic view of LVDT.

Table 3.3: Specification of spring

Spring	Manufacturer	Locally Made
	Length	0.4m
	Stiffness	20kN/m
	Type	Coiled(Compression)
	Material	Chrome silicon, Chrome Vanadium

Table 3.4: Component specification of Real-time system, RTS

Manufacturer	National Instrument (NI)
Serial No.	NI-cRIO 9081
Processor	Intel Celeron U3405 (1.06GHz)
Operating Temperature Range	0 to 55 °C operating
Input module, IM	NI-cRIO 9215 (4 Ch ±10V 16- Bit simultaneous Analog Input; -40^0 C ≤ Ta ≤70^0 C)
Output module, OM	NI-cRIO 9263 (4 Ch ±10V 16- Bit Analog Output; -40^0 C ≤ Ta ≤70^0 C)

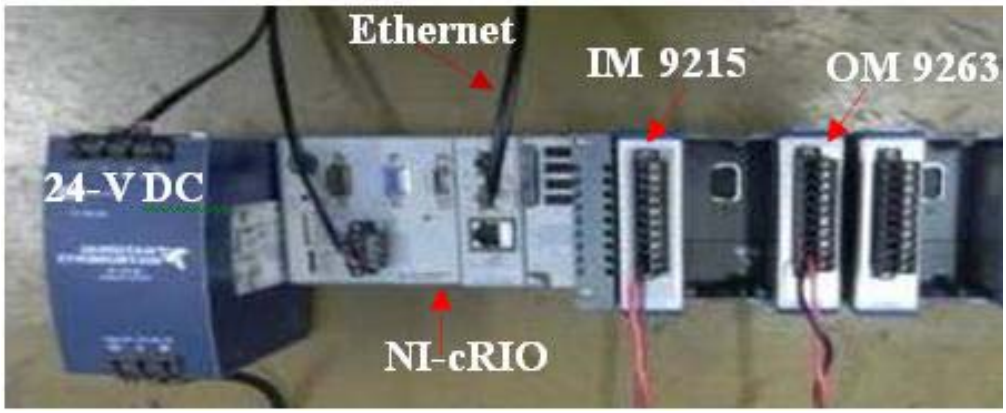

Figure 3.7: Photographic view of RTS.

Table 3.5: Component specification of Host PC

Processor	Intel Core i5-3450 CPU @3.10GHz
RAM	16.0 GB
System Type	64- Bit OS
Windows editions	Windows-7 Professional
Labview Edition	NI LabView 13.0.1 Professional for developing a motion-control software and interfacing it with the real-time system for system operation

3.2 Mathematical modeling of system

The mathematical modeling for the experimental set up in Fig. 3.1 is essential for implementation of the proposed controllers. This modeling has been dealt with the dynamic of the piston motion and the modeling for chamber pressures of actuator.

3.2.1 Dynamic modeling of piston motion

The dynamic modeling of piston motion in Fig. 3.1 is nearly similar to the dynamic modeling of Fig. 1.1. The dynamic equations of the piston motion in Fig. 3.1 with a compressive spring load can be expressed for the actuating piston mass m_p in terms of the extension and retraction modeling as

$$\ddot{x} = [P_1 A_{a1} - P_2 A_{a2} - k(x+\delta) - F_f]/m_p \text{ for } V \geq V_0, \quad (3.1a)$$

and $$\ddot{x} = [P_2 A_{a2} - P_1 A_{a1} - k(x-\delta) - F_f]/m_p \text{ for } V < -V_0, \quad (3.1b)$$

where F_f is the friction in cylinder surface, k is stiffness of the spring and δ is the pre-compression of the spring. For this system, compression of the spring can be immediately felt effected with start of motion of the piston.

The friction F_f has been considered as the simplified form of the friction model incorporating the friction parameters α_{vp}, α_{vn}, F_{0p} and F_{0n} mentioned in (1.2c) and (1.2d). The chamber pressures have been considered as P_1 in Ch1 and P_2 in Ch2 with corresponding areas A_{a1} and A_{a2} which have been formulated previously in (1.1d) and (1.1e) of Section 1.1.

3.2.2 Modeling for chamber pressures of actuator

The corresponding chamber pressures P_1 and P_2 can be obtained similar to Section 1.1 by implementing the valve modeling adopted from Sarkar et al. (2013a) and flow-pressure relationship mentioned in Merritt (1967). Considering the incompressible fluid flow, the corresponding flow-pressure relationship can be established as

$$Q_1 = C_{v1}(V - V_0)\sqrt{P_P - P_1} \text{ for } V \geq V_0, \tag{3.2a}$$

$$\text{and } Q_2 = C_{v2}(V - V_0)\sqrt{P_2 - P_T} \text{ for } V \geq V_0, \tag{3.2b}$$

$$\text{or } Q_1 = C_{v1}(V + V_0)\sqrt{P_1 - P_T} \text{ for } V < -V_0, \tag{3.2c}$$

$$\text{and } Q_2 = C_{v2}(V + V_0)\sqrt{P_P - P_2} \text{ for } V < -V_0, \tag{3.2d}$$

where C_{v1} and C_{v2} are the valve coefficients in ports A and B respectively. The pump and tank pressure have been considered as P_P and P_T respectively.

Now the chamber pressures can be derived by using the continuity equations (1.3a-b) and the corresponding flow-pressure relationships (3.2a-d) as

$$P_1 = P_P - [(A_{a1}\dot{x})/\{C_{v1}(V - V_0)\}]^2 \text{ for } V \geq V_0, \tag{3.2e}$$

$$\text{and } P_2 = P_T + [(A_{a2}\dot{x})/\{C_{v2}(V - V_0)\}]^2 \text{ for } V \geq V_0, \tag{3.2f}$$

$$\text{or } P_1 = P_T + [(A_{a1}\dot{x})/\{C_{v1}(V + V_0)\}]^2 \text{ for } V < -V_0, \tag{3.2g}$$

$$\text{and } P_2 = P_P - [(A_{a2}\dot{x})/\{C_{v2}(V + V_0)\}]^2 \text{ for } V < -V_0. \tag{3.2h}$$

For PV (Hydraulic catalogue of Bosch Rexroth AG - 4WREE, RE 29061/10.05) with specifications given in Table 3.2 and, it can be stated that PV used for linear-motion EHAS is a 2:1 valve and the pressure drop ratio in two metered ports is 4:1. From this pressure drop conditions, rated flow and flow-pressure relationships of (3.2a-d), it can be inferred that $C_{v1} = 2C_{v2}$.

Now considering $C_{v1} = C_v$ and so that $C_{v2} = 0.5C_v$, the simplified pressure equations can be rewritten with help of (3.2e-h) as

$$P_1 = P_P - [(A_{a1}\dot{x})/\{C_v(V - V_0)\}]^2 \text{ for } V \geq V_0, \tag{3.3a}$$

$$\text{and } P_2 = P_T + [(A_{a2}\dot{x})/\{0.5C_v(V - V_0)\}]^2 \text{ for } V \geq V_0, \tag{3.3b}$$

$$\text{or } P_1 = P_T + [(A_{a1}\dot{x})/\{C_v(V + V_0)\}]^2 \text{ for } V < -V_0, \tag{3.3c}$$

$$\text{and } P_2 = P_P - [(A_{a2}\dot{x})/\{0.5C_v(V + V_0)\}]^2 \text{ for } V < -V_0. \tag{3.3d}$$

The real time control voltage V in (3.3a) to (3.3d) has been extracted in the next section by using the voltage extraction model through input linearization technique.

3.3 Input Linearization technique for Voltage Extraction model

The system dynamic equations in (3.1a-b) can be related to n^{th} order nonlinear dynamic system (2.9a) and it can be inferred from those equations that the existing set up is 2nd order system. The corresponding 2nd order dynamic equation can be reformed with help of (3.3a-d) as

$$\ddot{x} = [P_P A_{a1} - \{A_{a1}^3\dot{x}^2 / C_v^2(V - V_0)^2\} - P_T A_{a2} - \{4A_{a2}^3\dot{x}^2 / C_v^2(V - V_0)^2\} - k(x + \delta) - F_f]/m_p \text{ for } V \geq V_0, \tag{3.4a}$$

$$\text{or } \ddot{x} = [P_P A_{a2} - \{4A_{a2}^3\dot{x}^2 / C_v^2(V + V_0)^2\} - P_T A_{a1} - \{A_{a1}^3\dot{x}^2 / C_v^2(V + V_0)^2\} - k(x - \delta) - F_f]/m_p \text{ for } V < -V_0. \tag{3.4b}$$

To execute the real-time experimentations of nonlinear dynamic system (3.4a) or (3.4b), the input linearization technique in Section 2.4 can be implemented to construct the voltage extraction formulation from the corresponding control input. The 2nd order system (3.4a) or (3.4b) recasts as (2.32c) involving the sliding variable (2.32d) and Hurwirtz coefficient (2.32e), the disturbance d, linearized input u and the extracted voltage V can be expressed in the form consistent with (2.9a-c) as

$$d = \ddot{x}_d + \lambda_1\dot{x}_d + \lambda_0 x_d - \{(P_P A_{a1} - P_T A_{a2})/m_p\} - \lambda_1\dot{x} + \lambda_0 x + k\delta \text{ for } V \geq V_0, \tag{3.5a}$$

$$\text{or } d = \ddot{x}_d + \lambda_1\dot{x}_d + \lambda_0 x_d - \{(P_P A_{a2} - P_T A_{a1})/m_p\} - \lambda_1\dot{x} + \lambda_0 x - k\delta \text{ for } V < -V_0, \tag{3.5b}$$

$$u = [\{\dot{x}^2/(V \pm V_0)^2\}\{(A_{a1}^3/C_v^2) + (4A_{a2}^3/C_v^2)\} + kx + F_f]/m_p, \tag{3.5c}$$

$$\text{and } V = \dot{x}\sqrt{[\{(A_{a1}^3/C_v^2) + (4A_{a2}^3/C_v^2)\}/(m_p u - kx - F_f)]} + V_0\,\text{sgn}(\dot{x}). \tag{3.5d}$$

The disturbance formulation (3.5a) or (3.5b) involves the output x and its derivative along with disturbances parameters in the form of pump pressure, tank pressure, spring stiffness, actuated mass, the demand, its first and second derivatives.

The linearized input (3.5c) involves the system parameter vector containing the valve coefficient, friction coefficient and some of the disturbance parameters. This justifies the use of compensation through (2.15a) and (2.15c) or (2.15b) and (2.15d). Moreover, the linearized input also involves the extracted voltage in an explicit form together with the control vector containing the parameters mentioned in (2.17a) or (2.17b) in an implicit form.

The input linearized extracted voltage V is the input to the control card of PV to execute the piston dynamic of the system. The parameters involved to formulate V in the real-time experiments are as

(a) *Constant parameters,* $\mathrm{C}_{\text{linear}}$**:** The constant parameters A_{a1}, A_{a2}, m_p and k have been represented as

$$\mathrm{C}_{\text{linear}} = (A_{a1} \;\; A_{a2} \;\; m_p \;\; k \;). \tag{3.6a}$$

A_{a1} and A_{a2} can be extracted from the specifications of cylinder in Table 3.2 and using their respective formulations used in (1.1d) and (1.1e) as

$$A_{a1} = \pi(0.04)^2 / 4 = 0.0013\mathrm{m}^2, \tag{3.6b}$$

and $$A_{a2} = \pi\{(0.04)^2 - (0.02)^2\} / 4 = 0.00094\mathrm{m}^2. \tag{3.6c}$$

Tables 3.2 and 3.3 provide m_p as 2.5kg and k as 20KN/m.

(b) *System parameters,* $\mathrm{q}_{\text{linear}}$**:** The friction parameters α_{vp}, α_{vn}, F_{0p} and F_{0n} of (1.2c) and (1.2d) have been used here to construct the friction F_f which is again used to formulate V. Including these friction parameters along with C_v and V_0 have been treated as the system parameters and these parameters have been represented as

$$\mathrm{q}_{\text{linear}} = (\alpha_{vp} \;\; \alpha_{vn} \;\; F_{0p} \;\; F_{0n} \;\; C_v \;\; V_0). \tag{3.7}$$

(c) *Control parameter,* $\hat{\psi}_{\text{FSMC}}$ ***or*** $\hat{\psi}_{\text{SMIC}}$**:** The corresponding control parameters in $\hat{\psi}_{\text{FSMC}}$ and $\hat{\psi}_{\text{SMIC}}$ have been involved to construct u which is again required to formulate V.

The system parameters $\mathrm{q}_{\text{linear}}$ and control parameters $\hat{\psi}_{\text{FSMC}}$ or $\hat{\psi}_{\text{SMIC}}$ together can make the parameter vector $\mathbf{p}$ mentioned in Fig. 1.13. These system and control parameters have been optimized in the next section.

3.4 Identification of System and Control Parameters

For the identification of $\mathrm{q}_{\mathrm{linear}}$ and then for $\hat{\psi}_{\mathrm{FSMC}}$ or $\hat{\psi}_{\mathrm{SMIC}}$, RCGA with an in-house script (Sarkar et al., 2013b) has been employed here offline. The identification of each case has been performed with the procedures mentioned in Fig. 1.13 of Section 2.3. The corresponding terms upper bound $\mathbf{b}_u$ and the lower bound $\mathbf{b}_l$ for the parameter vectors $\mathbf{p}$ used in Fig. 1.13 have been stated later in the corresponding identification process. In each case, the first generation is created as a random distribution of ten sets of parameter values over a specified bound for each. For the next generations, another ten sets are obtained by aiming a minimization of the difference between a model prediction and its experimental variation with a preset PID controller for 1Hz sinusoidal motion of 0.02m amplitude.

3.4.1 Identification of System Parameters

For estimating the system parameters, the index to be minimized is taken as integral absolute error, IAE which has been defined as

$$\mathrm{IAE} = \int_0^T |x_d - x|\, dt, \tag{3.8}$$

where x is the piston motion predicted by using open-loop models (3.4a) and (3.4b) for each set of parameters in a generation and x_d is taken here as the experimental response of PID for the sinusoidal demand over a cycle time T. The experimental response x_d has been considered here as LVDT reading of PID performance. The constant parameters and the experimental variation of the voltage V have been fed in (3.4a) and (3.4b) as the excitation input in each prediction run.

Now Fig. 3.8 depicts the convergence of IAE for all 10 sets of parameter values after every 5 generations. The optimizer yielded the system parameters of $\mathrm{q}_{\mathrm{linear}}$ as

$$\mathrm{q}_{\mathrm{linear}} = (\,2000\;\; 2500\;\; 900\;\; 600\;\; 2*10^{-7}\;\; 0.8), \tag{3.9a}$$

with their respective unit as kgs^{-1}, kgs^{-1}, N, N, $\mathrm{m}^3/(\mathrm{s.V.}\sqrt{\mathrm{Pa}})$ and V extracted from the set yielding the lowest IAE after 15 generations.

The corresponding $\mathbf{b}_l$ and $\mathbf{b}_u$ in Fig. 1.13 for $\mathrm{q}_{\mathrm{linear}}$ have been chosen respectively as

$$\mathrm{q}_{\mathrm{linear}}(\mathrm{lower}) = (\,1000\;\; 1500\;\; 500\;\; 200\;\; 5*10^{-8}\;\; 0.5), \tag{3.9b}$$

and $$\mathrm{q}_{\mathrm{linear}}(\mathrm{upper}) = (\,4000\;\; 3500\;\; 1500\;\; 900\;\; 9*10^{-7}\;\; 1.5). \tag{3.9c}$$

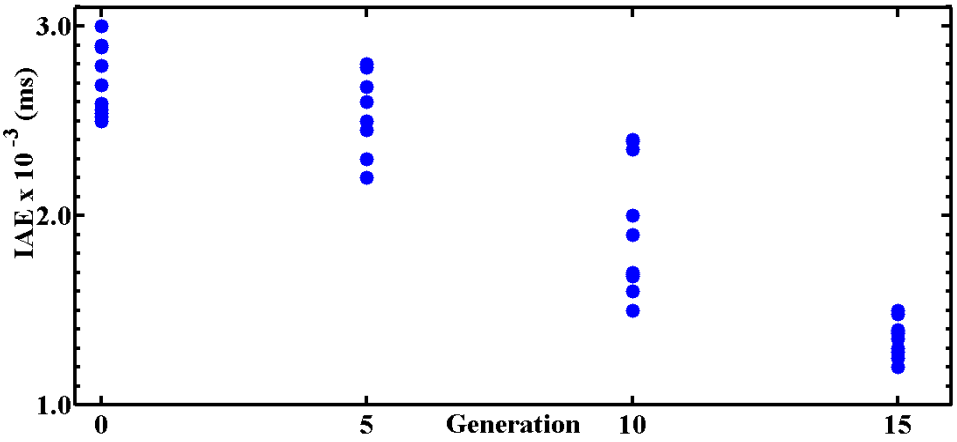

Figure 3.8: Identification of system parameters for linear-motion EHAS through optimization.

3.4.2 Identification of Control Parameters

For estimating the control parameters, the control energy CE index has been implemented and this index has been defined as

$$\mathrm{CE} = \int_0^T V^2 dt \text{ for actual control } V, \tag{3.10a}$$

$$\text{and } \mathrm{CE}_p = \int_0^T V_p{}^2 dt \text{ for predicted control } V_p, \tag{3.10b}$$

where V is the experimental voltage and V_p has been predicted from (3.5d). In (3.5d), sequential use has been made of friction model equations (1.2c) and (1.2d), the variation of LVDT reading, the constant parameters $\mathrm{C}_{\mathrm{linear}}$, the optimized $\mathrm{q}_{\mathrm{linear}}$ and the corresponding u.

The difference of CE and CE_p yielding

$$|\,\mathrm{CE} - \mathrm{CE}_p\,| = \int_0^T |\,V^2 - V_p^2\,|\,dt, \tag{3.10c}$$

has been minimized to identify the control parameters of FSMC and SMIC in next.

(I) *Identification of control parameters of FSMC*

In FSMC input (2.12a), the set (2.32d), (2.13), (2.14a) and (2.15a) has been used in this identification with chosen values of Hurwirtz coefficient as

$$\lambda = (5\ \ 3), \tag{3.11a}$$

with their dimensions as s^{-1} and s^{-2}.

The parameters in $\mathrm{f}_{\mathrm{FSMC}}$ have been chosen as

$$\mathrm{f}_{\mathrm{FSMC}} = (2000\ \ 2000\ \ 2000\ \ 2000\ \ 2000\ \ 5000), \tag{3.11b}$$

with their corresponding dimensions s^{-2}, s^{-2}, $\mathrm{s}^{6}\mathrm{m}^{-5}$, $\mathrm{s}^{2}\mathrm{m}^{-1}$, s^{-2} and m^{-1} respectively.

The corresponding $\mathbf{b}_l$ and $\mathbf{b}_u$ for ψ_{FSMC} have been chosen respectively as

$$\psi_{\text{FSMC}}(\text{lower}) = (1000\ \ 0\ 0\ 0\ 0\ 0\ \ 0\ 0\ 0\ 0\ -4\ \ -3\ -2\ -1\ 0\ \ 2000), \qquad (3.11c)$$

and $\psi_{\text{FSMC}}(\text{upper}) = (10000\ 1000\ 1000\ 1000\ 1000\ 1000\ 2\ 2\ 2\ 2\ 2$

$$4\ 5\ 6\ 7\ 8\ 10000), \qquad (3.11d)$$

with their dimensions as ms^{-2}, ms^{-2}, ms^{-2}, ms^{-2}, ms^{-2}, ms^{-2}, sm^{-1}, sm^{-1}, sm^{-1}, sm^{-1}, sm^{-1}, ms^{-1}, ms^{-1}, ms^{-1}, ms^{-1}, ms^{-1}, ms^{-2}, ms^{-2}, ms^{-2}, ms^{-2} and ms^{-2} respectively. Fuzzy controller in ψ_{FSMC} has five rules in the rule base for $\hat{\xi}_{fi}$.

Fig. 3.9 depicts the convergence of $|\text{CE} - \text{CE}_p|$ for all 10 sets of parameter values after every 5 generations by using the corresponding values in (3.11a-d). The optimizer yields the optimized parameters of $\psi_{\text{FSMC}}(\text{initial})$ from the set yielding the lowest value of $|\text{CE} - \text{CE}_p|$ after 20 generations depicted in Fig. 3.9 as

$$\psi_{\text{FSMC}}(\text{initial}) = (3000\ \ 100\ \ 200\ \ 300\ \ 400\ \ 500\ 1\ 1\ 1\ 1\ 1$$

$$-2\ -1\ 0\ 1\ 2\ 2000), \qquad (3.11e)$$

with their corresponding dimensions as in (3.11c) or (3.11d).

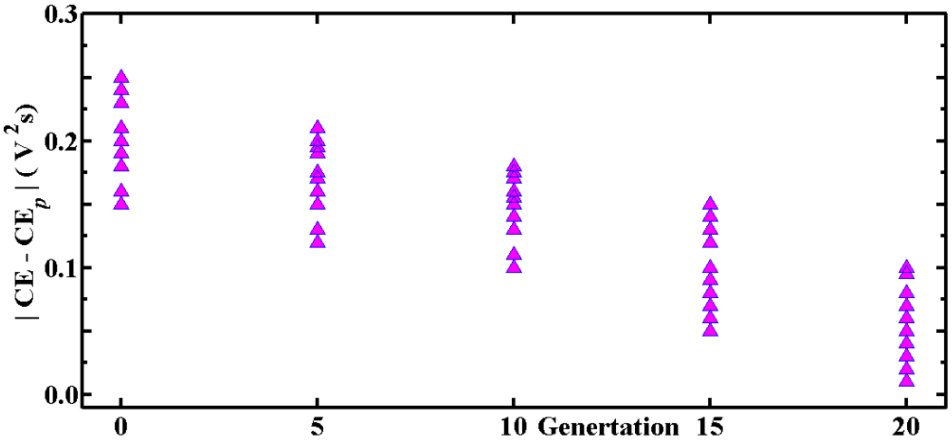

Figure 3.9: Identification of control parameters of FSMC for linear-motion EHAS through optimization.

(II) ***Identification of control parameters of SMIC***

In SMIC input (2.12b), the set (2.32d), (2.16) and (2.15b) has been used in this identification with chosen values of Hurwirtz coefficient as

$$\lambda = (5\ \ 3), \tag{3.12a}$$

with their dimensions as s^{-1} and s^{-2}.

The parameters in f_{SMIC} have been chosen as

$$f_{SMIC} = (2000\ \ 2000\ \ 5000), \tag{3.12b}$$

with their dimensions s^{-2}, s^{-2} and m^{-1} respectively.

The corresponding $\mathbf{b}_l$ and $\mathbf{b}_u$ for ψ_{SMIC} have been selected respectively as

$$\psi_{SMIC}(\text{lower}) = (1000\ \ 5000), \tag{3.12c}$$

$$\text{and } \psi_{SMIC}(\text{upper}) = (10000\ \ 10000), \tag{3.12d}$$

with their dimensions ms^{-2} and ms^{-2}.

Fig. 3.10 depicts the convergence of $|CE - CE_p|$ for all 10 sets of parameter values after every 5 generations by using the corresponding values in (3.12a-d). The optimizer yield the corresponding parameters in $\psi_{SMIC}(\text{initial})$ as

$$\psi_{SMIC}(\text{initial}) = (4000\ \ 5000), \tag{3.12e}$$

extracted from the set yielding the lowest $|CE - CE_p|$ after 25 generations.

With the optimized values of system and control parameters, the implementation and real time performance of the overall controller have been described in the next section.

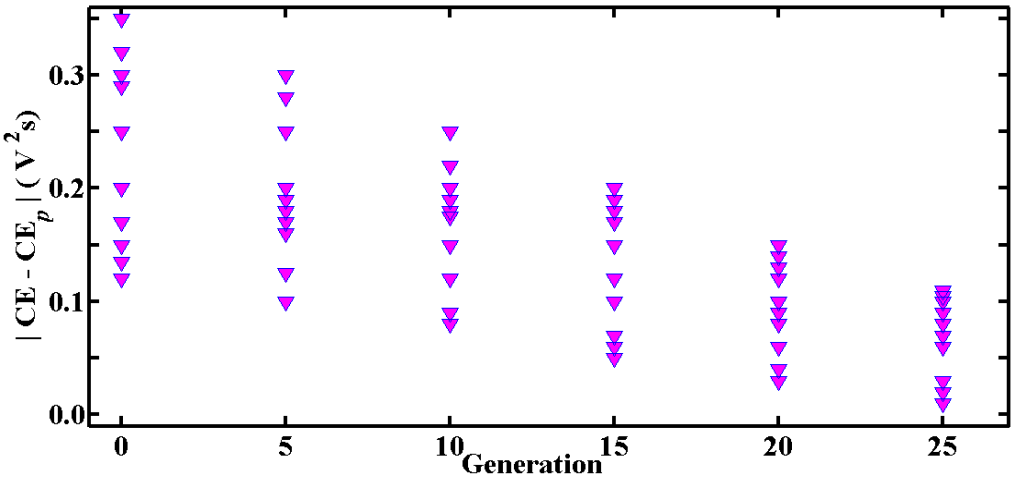

Figure 3.10: Identification of control parameters of SMIC for linear-motion EHAS through optimization.

3.5 Results and Discussion

This section deals with the real time control with the proposed adaptive controllers FSMC and SMIC for a laboratory scale real-time EHAS set up of Fig. 3.1 producing the linear motion. For developing the motion-control software and interfacing it with the real-time system, NI LabView13.0.1 Professional has been used in the Host PC. An user defined demand x_d has been fed to Labview and the real time system response x measured by LVDT has been communicated to Labview through IM of RTS. The tracking error e has been formulated by using x_d together with LVDT response x gathered at a sampling rate T_s of 1kHz. To minimize the error, the control voltage V has been extracted in Labview by using the input linearized control voltage formulation (3.5d). Labview extracted control voltage has been communicated to the control card of PV through OM of RTS. The control card has been excited and it controls the required flow rate as well as the direction of the fluid flow to the actuator to get the desired piston motion. The control voltage formulation (3.5d) has been extracted by using the constant parameters, the optimized system and control parameters obtained in the Section 3.4.

The corresponding controller architecture followed by the controller selection process and the real time results have been discussed in the next section. The real time experiments have been done with the setup described by Fig. 3.1 at 8MPa PRV setting and 50 lpm flow rate. The experimental plan for this system has been organized as

(a) Controller Architecture for adaptation of FSMC.

(b) Real time adaption of FSMC control parameters for 1Hz sinusoidal motion with 0.02m amplitude demand.

(c) Controller Architecture for adaptation of SMIC.

(d) Real time adaptation of SMIC control parameters for 1Hz sinusoidal motion with 0.02m amplitude demand.

(e) Selection of suitable Controller for real time performances

(f) Real time performances with suitable controller for different types of tracking, regulatory and their combined motions.

3.5.1 Controller Architecture for Adaptive Control

The controller architecture contains few blocks and the flow diagram for making the connectivity between the different blocks to represent the input to the system, error dynamics, parameters required to formulate the control input, adaptive rules and the system output. The corresponding adaptive formulation process and the step along with an experimental result showing the adaption of the control parameter for each case have been performed in next.

(I) ***Controller Architecture for real time adaptation of FSMC***

The controller architecture for FSMC has been described now with help of Fig. 3.11 involving the following adaption steps

a) Choose the fixed parameter f_{FSMC} and the corresponding control parameters $\hat{\psi}_{FSMC}(\text{upper})$, $\hat{\psi}_{FSMC}(\text{lower})$ and $\hat{\psi}_{FSMC}(\text{initial})$.

b) Find the sliding variable s from (2.32d).

c) Determine $\hat{\xi}_{fi}$, $\hat{d}_{\beta i}$ and $\hat{d}_{ci}$ respectively from (2.14b), (2.18r) and (2.18s).

d) Using the values obtained in last step along with Lyapunov functional (2.23a) and its derivative (2.23c) and corresponding adaptive rules (2.18a-q), obtain $\hat{u}_{FSMC}$ using

$$\hat{\psi}_{FSMC}|_{t+1} = \hat{\psi}_{FSMC}|_{t} + \dot{\hat{\psi}}_{FSMC}|_{t}\, T_s \ . \tag{3.13}$$

e) Extract the control voltage V from (3.5d) by using constant parameters of C_{linear}, optimized system parameters of q_{linear} and control parameters of $\hat{\psi}_{FSMC}$

f) Execute the real time system with the extracted control voltage V.

g) Formulate the error e by using the user defined demand x_d and the system response x measured by LVDT feedback.

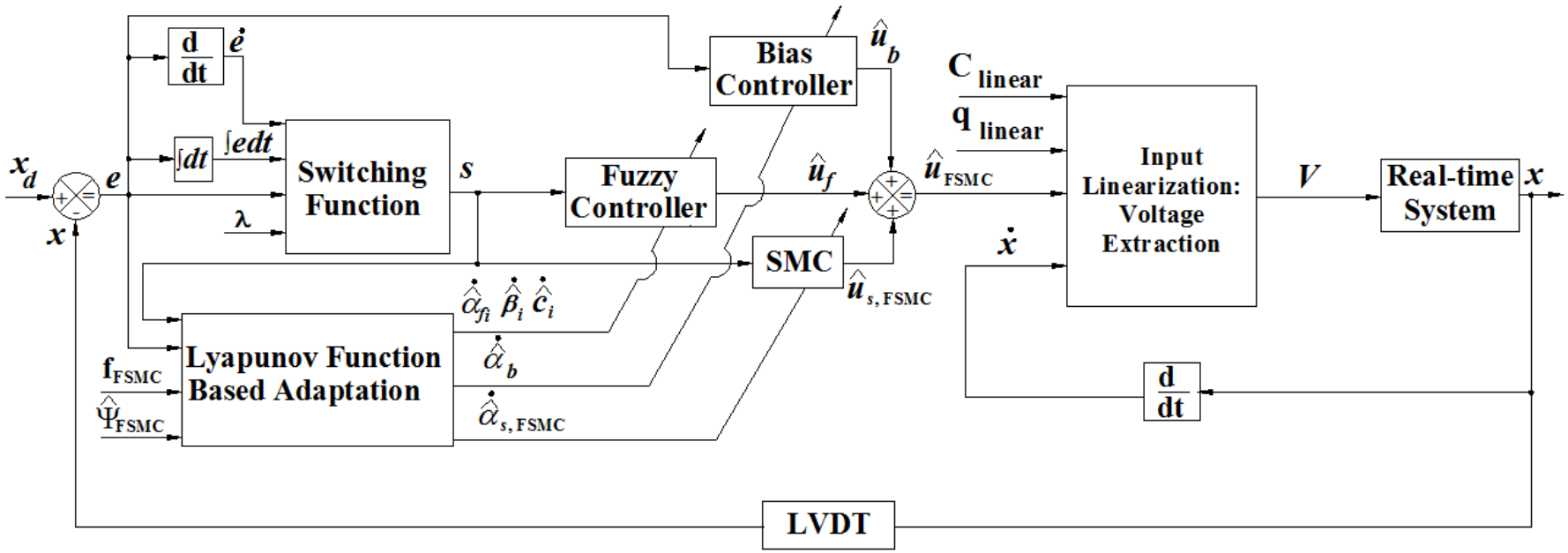

Figure 3.11: Schematic architecture of the proposed adaptive FSMC for linear- motion EHAS.

Implementing the corresponding adaptation steps of FSMC, the real time adaptions of the corresponding control parameters have been depicted in Figs. 3.12 and 3.13 for 1Hz sinusoidal motion of 0.01m amplitude. The real time response for the sinusoidal motion has been depicted in Fig. 3.12(a) with the corresponding error in Fig. 3.12(b) or 3.13(a). For the response in Fig 3.12(a), the adaptations of $\hat{\alpha}_b$ and $\hat{\alpha}_{s,\mathrm{FSMC}}$ have been depicted in Fig. 3.12 and the adaptations of $\hat{\alpha}_{fi}$, $\hat{\beta}_i$ and $\hat{c}_i$ have been portrayed in Fig. 3.13. The adaptions in Figs. 3.12(c, d) and 3.13(b-p) show that the adaption process has been started from their corresponding initial values and continue before reaching to e_δ region which has been taken here as ±2mm. The adaptation remains suspended within e_δ region and the control parameter sustains its last updated value. It is also evident that adaptation process has been activated instantly when error crosses e_δ zone and this updating has been stared from their corresponding last updated value.

Figs. 3.12(b-d) and Figs. 3.13(a-p) states that green colored points correspond to activation of the adaptation of the control parameters due to the error e growing beyond the layer $\pm e_\delta$ within which the adaptation remains suspended. Red colored points represent to deactivation of the adaptation process. Each phase of adaptive change in Figs. 3.12(c, d) and 3.13(b-p) shows monotonic increase of $\hat{\alpha}_{s,\mathrm{FSMC}}$ acording to (2.18l) and non-monotonic changing phase of $\hat{\alpha}_b, \hat{\alpha}_{fi}$, $\hat{\beta}_i$ and $\hat{c}_i$ through (2.18h-k). A resetting option for $\hat{\alpha}_{s,\mathrm{FSMC}}$ at the optimizer-determined value after detecting its dwelling at the upper limit for a reasonably long phase overcomes the possible problem of saturation of this parameter rendered by the projection operator. The adaption has been done with in the corresponding lower and upper limit which has been clearly reflected for $\hat{\beta}_i$ and $\hat{c}_i$ in Figs. 3.13(g-p). The results in Figs. 3.12 and 3.13 clearly show that adaptive laws and formulations have been successfully implemented.

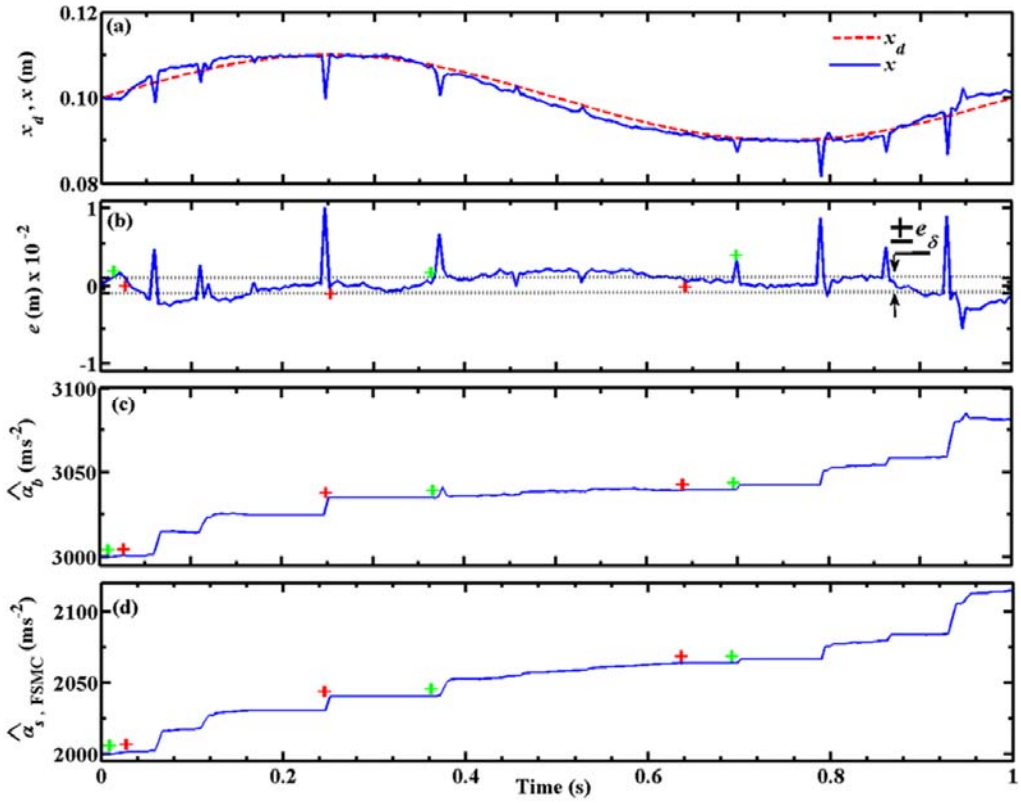

Figure 3.12: Real-time adaptation of $\hat{\alpha}_b$ and $\hat{\alpha}_{s,\mathrm{FSMC}}$ for 1Hz sinusoidal motion with 0.02m amplitude demand.

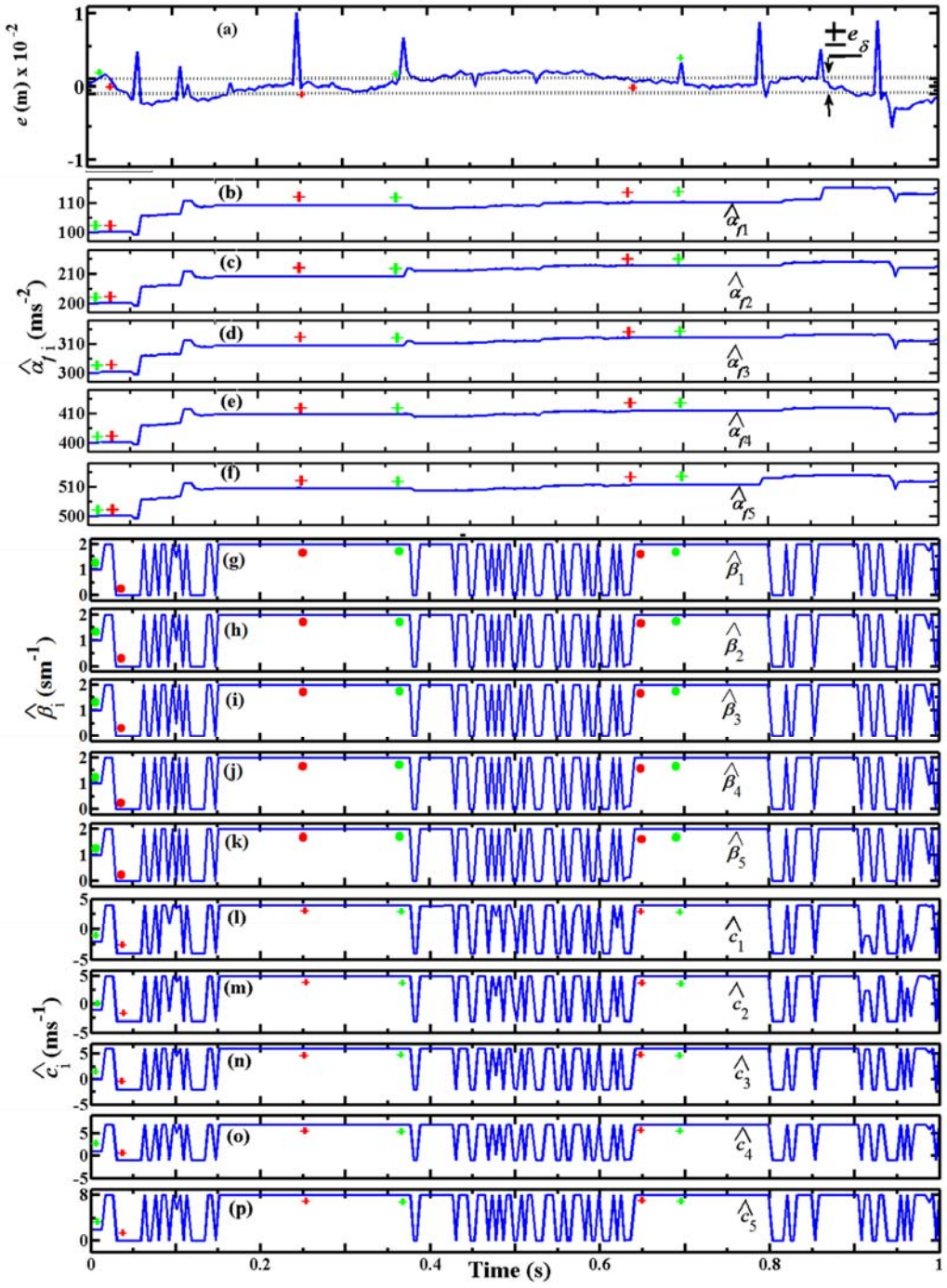

Figure 3.13: Real-time adaptation of $\hat{\alpha}_{fi}$, $\hat{\beta}_i$ and $\hat{c}_i$ for the corresponding response in Fig 3.12(a).

(II) ***Controller Architecture for real time adaptation of SMIC***

The controller architecture for SMIC has been described now with help of Fig. 3.14 and adaption steps. The steps are as

a) Choose the fixed parameter f_{SMIC} and the corresponding control parameters $\hat{\psi}_{SMIC}(\text{upper})$, $\hat{\psi}_{SMIC}(\text{lower})$ and $\hat{\psi}_{SMIC}(\text{initial})$.

b) Find the sliding variable s from (2.32d).

c) Using Lyapunov functional (2.30a) and its derivative (2.30c) and corresponding adaptive rules (2.25a-h), obtain $\hat{u}_{SMIC}$ using

$$\hat{\psi}_{SMIC}|_{t+1} = \hat{\psi}_{SMIC}|_{t} + \dot{\hat{\psi}}_{SMIC}|_{t} T_s . \tag{3.14}$$

d) Extract the control voltage V from (3.5d) by using constant parameters of C_{linear}, optimized system parameters of q_{linear} and control parameters of $\hat{\psi}_{SMIC}$.

e) Execute the real time system with the extracted control voltage V.

f) Formulate the error e by using the user defined demand x_d and the system response x measured by LVDT feedback.

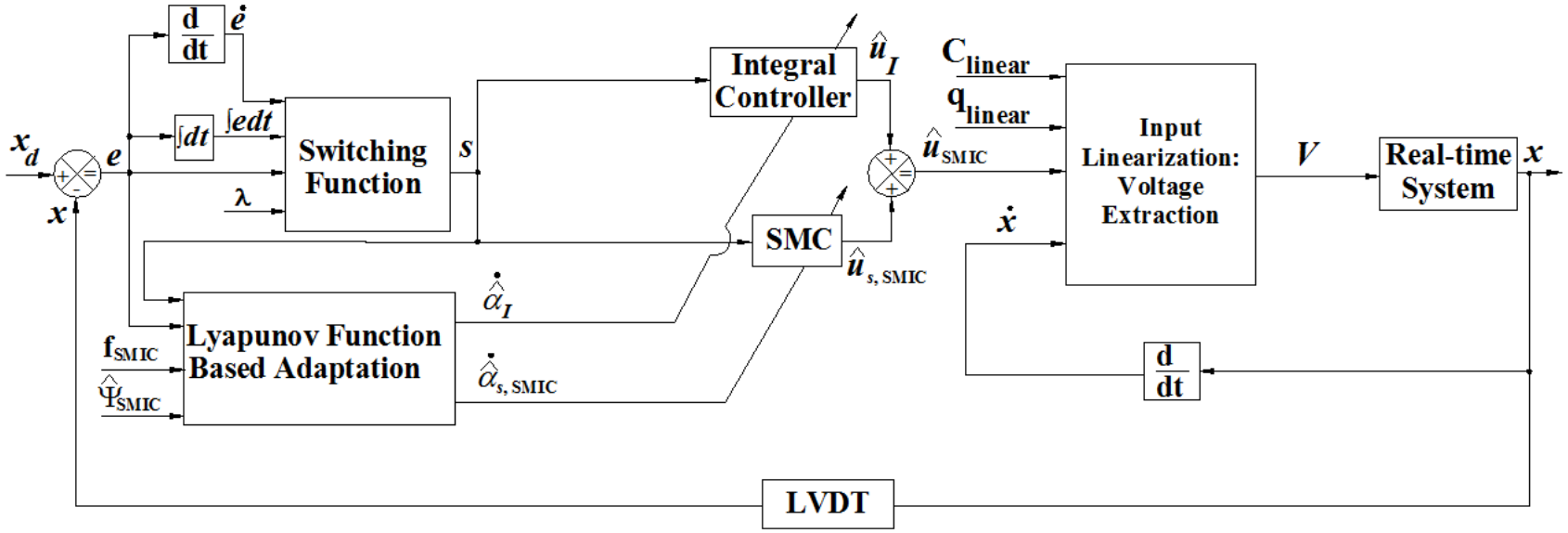

Figure 3.14: Schematic architecture of the proposed adaptive SMIC for linear-motion EHAS.

The real time adaptions of SMIC parameters have been depicted in Fig. 3.15 with 1Hz sinusoidal motion of 0.01m amplitude. The adaptions of $\hat{\alpha}_I$ and $\hat{\alpha}_{s,\text{SMIC}}$ have been shown respectively in Fig. 3.15(c) and Fig. 3.15(d) for the corresponding response in Fig. 3.15(a) and error in Fig. 3.15(b). The adaptions of $\hat{\alpha}_{s,\text{SMIC}}$ and $\hat{\alpha}_I$ have been started from their corresponding initial values and continue before reaching to the e_δ of ±2mm where the adaptation remains suspended and the control parameters sustain their last updated values. Few deactivation points have been notified with red color and few activation points have been shown as green color in Figs. 3.15(b-d). The increasing trends of $\hat{\alpha}_{s,\text{SMIC}}$ through (2.25f) and non-monotonic adaptation of $\hat{\alpha}_I$ through (2.25e) have been reflected in Fig. 3.15. The projection operator has been implemented here to reset $\hat{\alpha}_{s,\text{FSMC}}$ after detecting its dwelling at the upper limit.

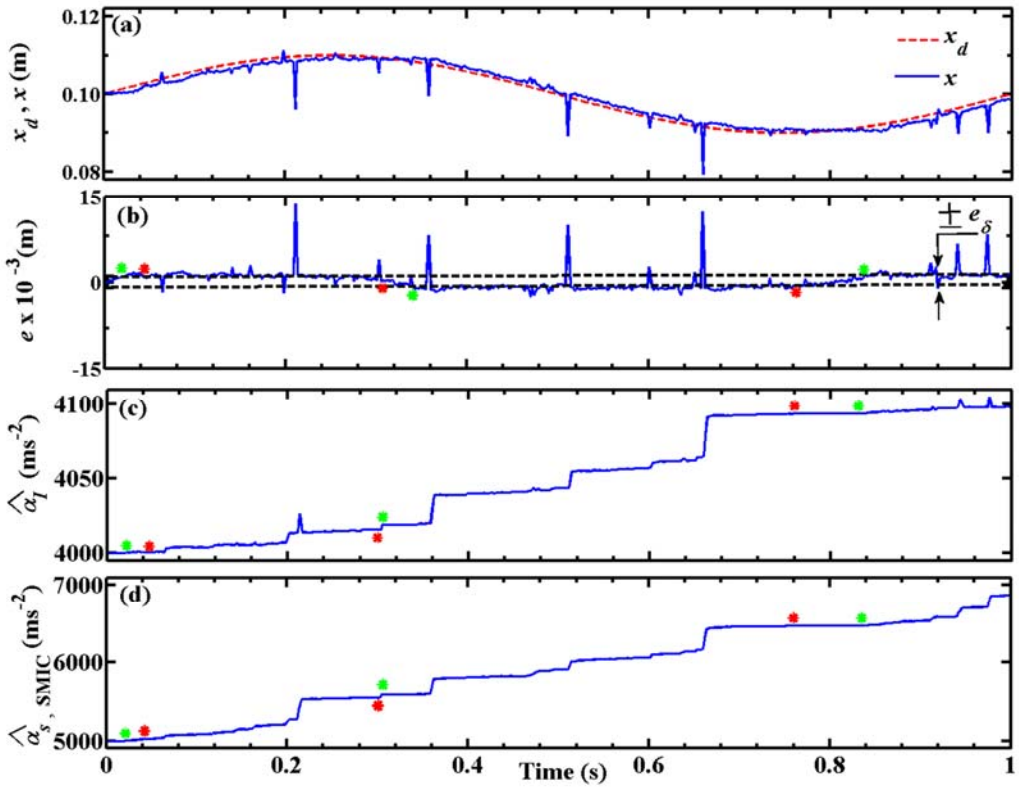

Figure 3.15: Real-time adaptation of SMIC parameters for 1Hz sinusoidal motion with 0.02m amplitude demand.

3.5.2 Selection of suitable Controller for real time performances

A comparison study for controller selection has been performed with the proposed controllers FSMC and SMIC including the other controllers as SMC formulated in (2.15a) or (2.15b), integral controller IC formulated in (2.16). The parameters used in FSMC and SMIC have been taken from their corresponding optimized values which have been identified in Section 3.4. The procedure followed for selection of parameters of SMC and IC has been adopted from the optimization processes developed in Section 3.4. The optimized parameters correspond to initial value of $\hat{\alpha}_s$ in SMC and $\hat{\alpha}_I$ in IC are respectively as 6000ms^{-2} and 8000ms^{-2}. The comparison study has been done also with Fuzzy-tuned PI controller developed by Dasmahapatra et al. (2015) with same linear-motion EHAS.

The comparison study has been done in Table 3.6 indicating the values of IAE and CE for 0.02m amplitude sinusoidal motion with frequency variation for different controllers. The formulation of IAE in (3.8) has been achieved with the user defined demand x_d and the piston motion x obtained by LVDT reading. The calculation of CE in (3.10a) has been performed with the control voltage V formulated by using (3.5d). The performance of the controller with the lowest value of these indexes has been treated as the best suited controller for the real time performances.

The observed higher IAE and CE variations in Table 3.6 with respect to those for SMC can be attributed for IC for its known feature of transient overshoot. The lower values of IAE for FSMC compare to SMC prove that Fuzzy has the capability to take care the continuous nonlinearity effect of the nonlinear system dynamic. Table 3.6 shows the higher values of IAE and CE for Fuzzy-tuned PI with respect to FSMC which establishes that SMC can tackle with different types of approximation and uncertainties associated with the system and controller modeling. Of course, the benefits of lower steady state error of IC and higher disturbance rejection capability of SMC have yielded the lowest IAE and CE in case of SMIC. With respect to the minimum IAE values apparent for all the controllers in the range between 3 and 4Hz, the observed increase with lowering of frequency could be due to the longer low-velocity phase of the piston for which Stribeck friction is known to increase (Rahmat et al., 2011). Table 3.6 reveals that the best suited controller for linear-motion EHAS is SMIC contributing the lowest values of IAE and CE. The real time performances with SMIC have been depicted in next.

Table 3.6: Comparisons of IAE and CE for different controllers of 0.02m sinusoidal motion with frequency variation

Controller / Frequency (Hz)	FSMC		SMIC		SMC		IC		Fuzzy-tuned PI	
	IAE (ms)	CE (V^2s)	IAE (ms)	CE (V^2s)	IAE (ms)	CE (V^2s)	IAE (ms)	CE (V^2s)	IAE (ms)	CE (V^2s)
1	0.00114	3.082	0.00110	3.098	0.00112	3.054	0.00115	3.078	0.00113	3.069
2	0.00108	3.605	0.00109	3.585	0.00110	3.594	0.00112	3.652	0.00109	3.584
3	0.00075	4.343	0.00073	4.165	0.00076	4.316	0.00078	4.363	0.00074	4.266
4	0.00138	4.525	0.00137	4.482	0.00140	4.577	0.00142	4.506	0.00139	4.493
5	0.00143	5.855	0.00142	5.587	0.00147	5.953	0.00149	5.868	0.00144	5.952
6	0.00228	6.034	0.00222	5.599	0.00230	6.048	0.00238	6.488	0.00229	6.098
7	0.00233	9.119	0.00231	8.921	0.00239	9.199	0.00249	9.305	0.00234	9.163

3.5.3 Real time performances with SMIC

This section presents the time-domain variations of response, error and voltage for the real time experimentations with SMIC for the linear-motion EHAS. The real time performances with SMIC have been done with tracking and regulatory motions. The sinusoidal motion has been considered here as tracking motion and the step motion has been taken as regulatory motion. The effect of the different spring pre-compression has been studied here with help of the step response. The combination of the tracking and regulatory motion as saw-tooth response has been performed in this work. The robustness of SMIC has been tested here with the arbitrary type of motion. In the time-domain variation of Figs 3.16 to 3.27, the corresponding demand and response of the different motion have been indicated as x_d and x respectively.

(I) ***Real time performances of SMIC with tracking motion: sinusoidal response***

The sinusoidal demands in Figs. 3.16 to 3.21 can be envisaged as a displacement demand with periodic in time t in s given in terms of the amplitude a, frequency f and initial piston position x_0 as

$$x_d = x_0 + a\sin(2\pi f t), \tag{3.15}$$

The real time performances of SMIC for sinusoidal motion have been obtained with different frequency demands with 0.02m amplitude in Figs. 3.16 to 3.18. Responses for some other amplitude have been given in Figs. 3.19 to 3.21. The results in Fig. 3.16 pertains the time-domain variation of SMIC responses of 0.02m sinusoidal motion (a, d, g) with corresponding errors (b, e, h) and voltages (c, f, i) for frequency demands of 3.0 to 5.0 Hz. Similarly the responses of 0.02m sinusoidal motion with frequency demands of 6.0 to 8.0Hz have been represented in Fig. 3.17. Figs. 3.16 and 3.17 reveal the tracking error to increase at higher rate beyond 4Hz and the control voltage has been saturated in ± 10V beyond 6Hz that additionally contributes to the errors. It can be interpreted from Figs. 3.16 and 3.17, with increase in frequency beyond 3Hz, the increase in IAE in Table 3.6 can be linked to the expected increase of phase lag between the demand and response. This characteristic has been attributed in Fig. 3.18 with the variation of gain-phase plot with frequency of the sinusoidal demand with 0.02m amplitude. The gain-phase plot has been considered here to determine the bandwidth on basis of 90^0 phase lag and -3dB loss of amplitude. The bandwidth has been determined about 6 to 7Hz for 0.02m sinusoidal response.

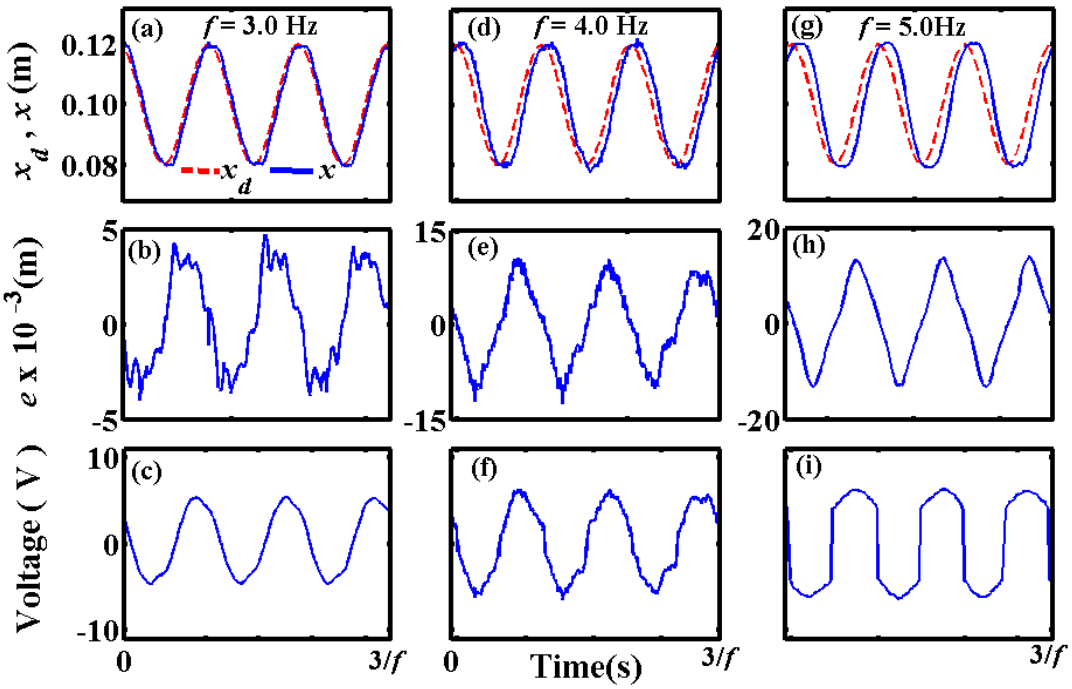

Figure 3.16: SMIC responses of 0.02m sinusoidal motion (a, d, g) with corresponding errors (b, e, h) and voltages (c, f, i) for frequency demands of 3.0 to 5.0 Hz.

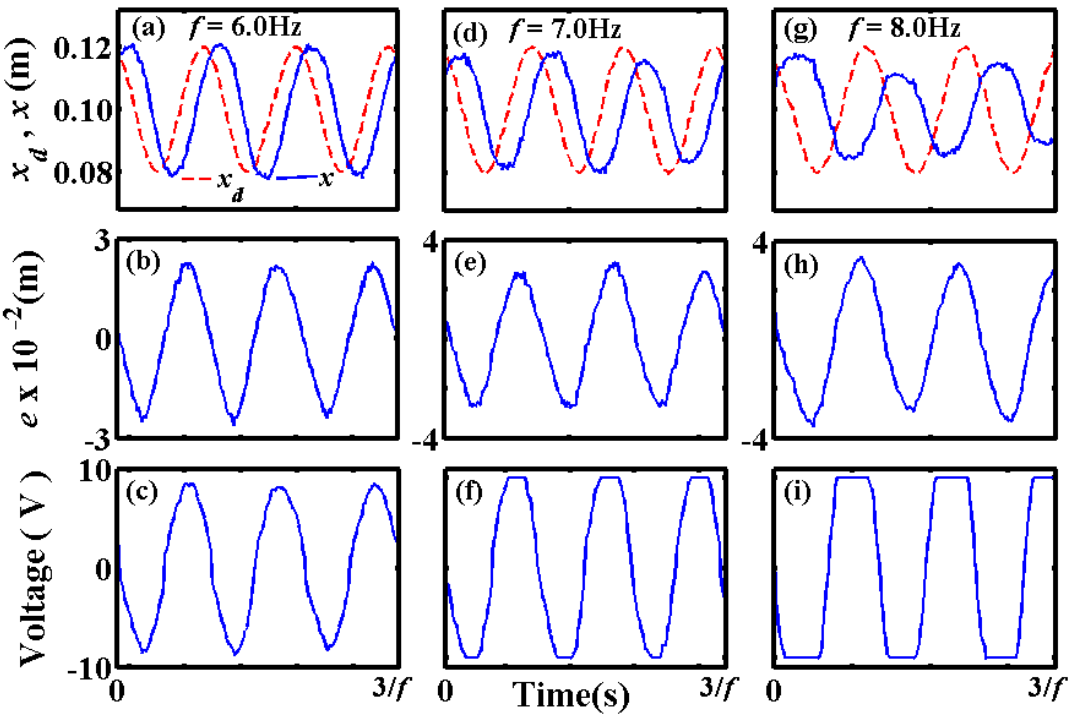

Figure 3.17: SMIC responses of 0.02m sinusoidal motion (a, d, g) with corresponding errors (b, e, h) and voltages (c, f, i) for frequency demands of 6.0 to 8.0 Hz.

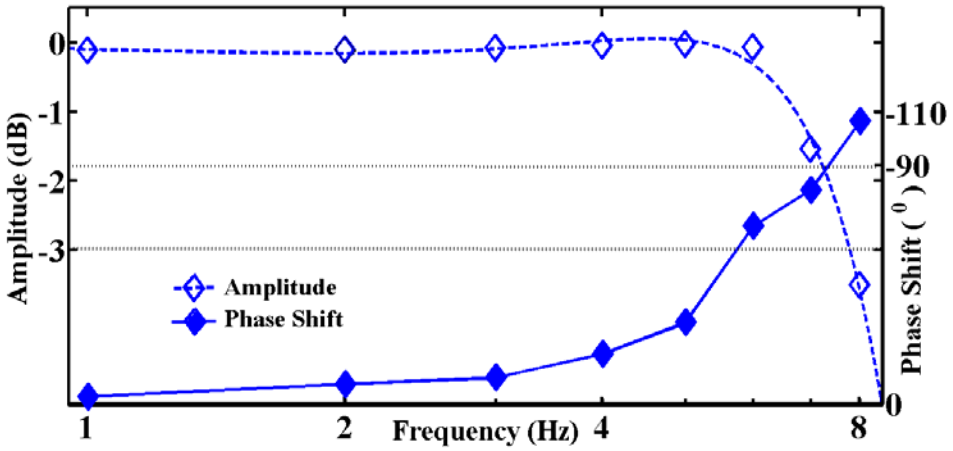

Figure 3.18: Variation of gain-phase plot with frequency of sinusoidal demand for SMIC with 0.02m amplitude.

In comparison to the responses of 0.02m sinusoidal amplitude, higher amplitude-lower frequency and lower amplitude-higher frequency sinusoidal responses have been investigated in Figs. 3.19 to 3.21. Figures show the satuaration of the control voltage to start at lower frequency and higher amplitude. It is understandable that Fig. 3.21 shows no voltage saturation problem at a lower amplitude demand of 0.01m for both 7 and 8Hz sinusoidal demands. The deterioration of the controller performances at high frequency in Fig. 3.21 can be attributed to the maximum bandwidth of 25Hz for PV rather than the limitation of the controller. Another very encouraging observation is complete elimination of chattering in both of control voltage and motion response of the piston.

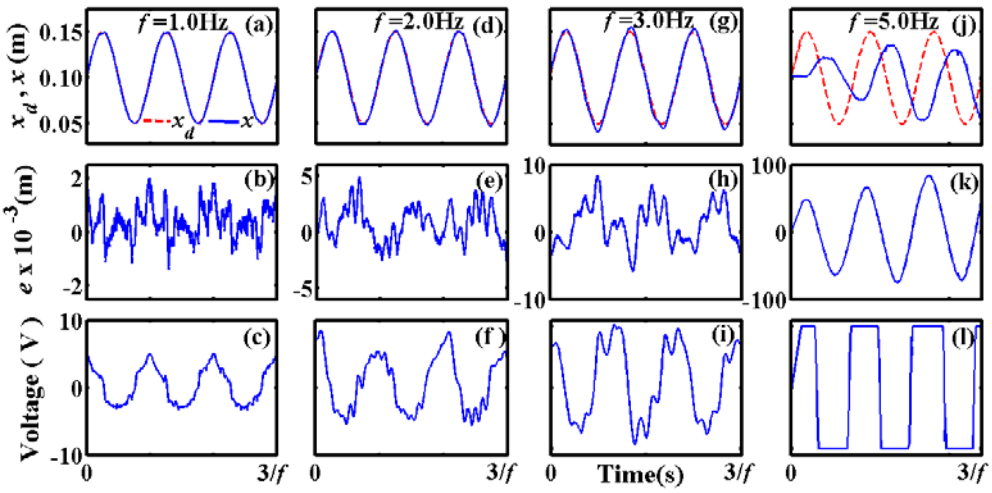

Figure 3.19: Different frequency demands and SMIC responses of 0.05m sinusoidal motion (a, d, g, j) with corresponding errors (b, e, h, k) and voltages (c, f, i, l).

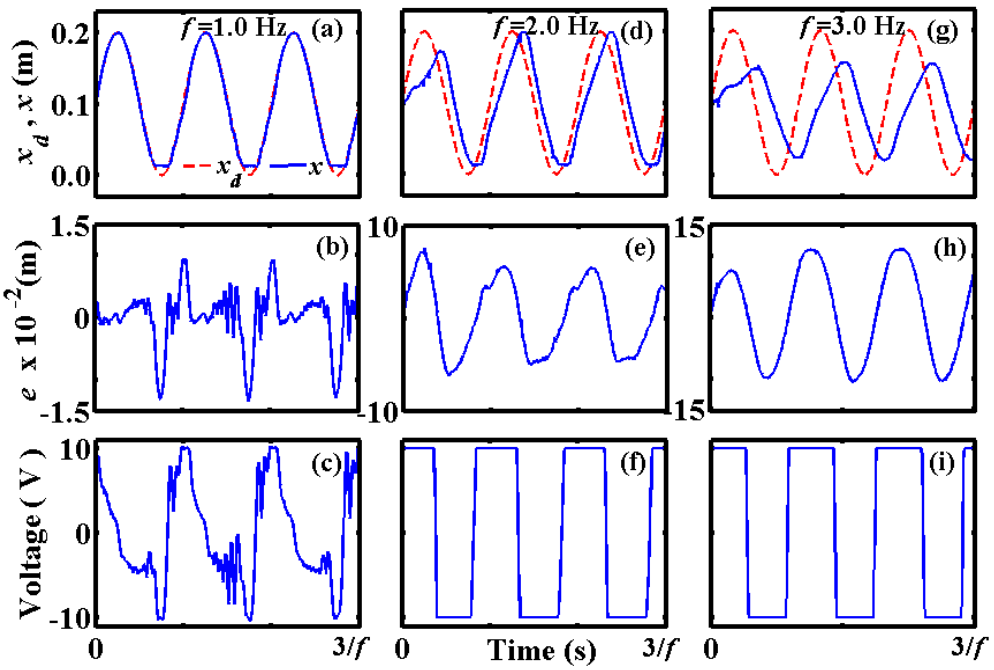

Figure 3.20: SMIC responses of 0.10m sinusoidal motion (a, d, g) with corresponding errors (b, e, h) and voltages (c, f, i) for frequency demands of 1.0 to 3.0 Hz.

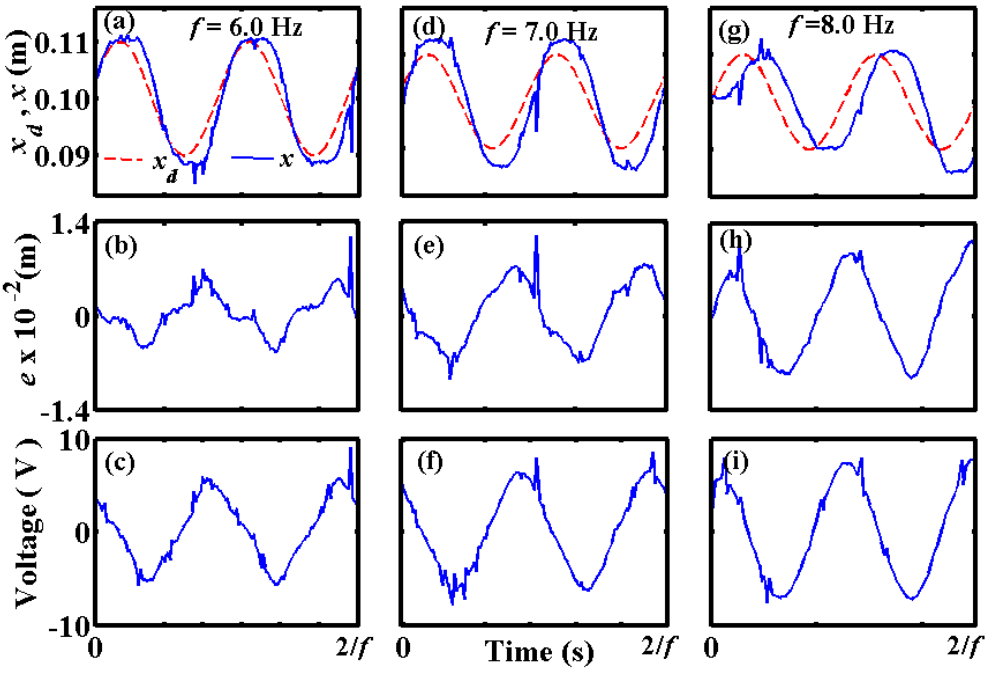

Figure 3.21: SMIC responses of 0.01m sinusoidal motion (a, d, g) with corresponding errors (b, e, h) and voltages (c, f, i) for frequency demands of 6.0 to 8.0 Hz.

(II) ***Real time performances of SMIC with regulatory motion: step response***

The performances of SMIC for step displacement of 0.1m against a compression spring have been studied in Figs. 3.22 and 3.23. Different initial positions x_0 have been considered, which correspond to different spring loading towards the cylinder. Fig. 3.22 represents the extension motion of piston opposed by the spring loading. The retraction motion of piston aided by the spring loading has been depicted in Fig. 3.23. It is physically understandable that for the similar error but higher initial compression due to higher x_0, the progress to zero error is slower during extension and faster during retraction. The maximum piston velocity for extension motion can be extracted from Fig. 3.22 as 0.30ms^{-1} which is less than that of formulated value as 0.64ms^{-1} by using area-flow relationship in (1.3a) for 50.0lpm flow and the corresponding area in (3.6b). Similarly maximum piston velocity for retraction motion extracted from Fig. 3.23 as 0.67ms^{-1} is also less than that of formulated value as 0.89ms^{-1} by using (1.3b) and (3.6c). These are also evident in the variations of IAE values given in Table 3.7. The effects of friction, spring loading and pressure drops at the metered ports are responsible for the lower values of the achieved velocities in comparison to that attainable had the full discharge from the pump occurred through PV. In other words, these effects lead to different variations of the voltage input to the valve resulting in the corresponding variations in CE observed in Table 3.7. Of course, CE values in Table 3.7 corresponding to Figs. 3.22 and 3.23 emerge from the requirement of higher voltage during extension than during retraction motion due to the compression loading of the spring. The most remarkable observation is absence of chattering achieved with SMIC.

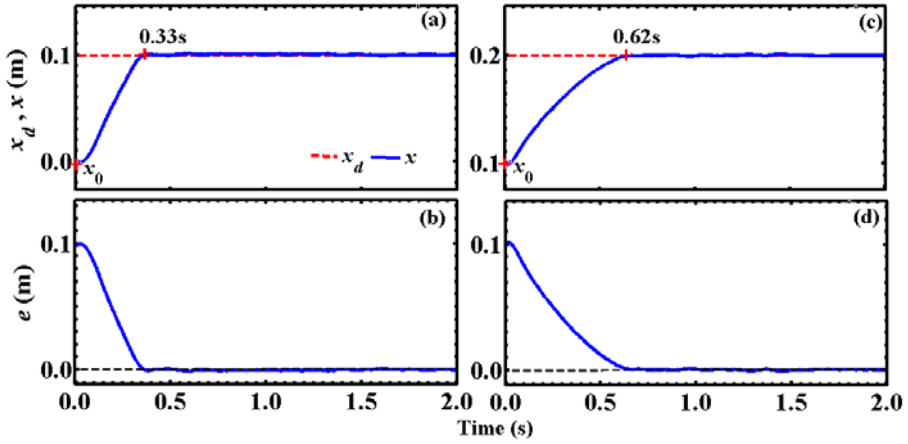

Figure 3.22: SMIC performances of 0.1m step responses (a, c) with their corresponding errors (b, d) for extension motion at different x_0.

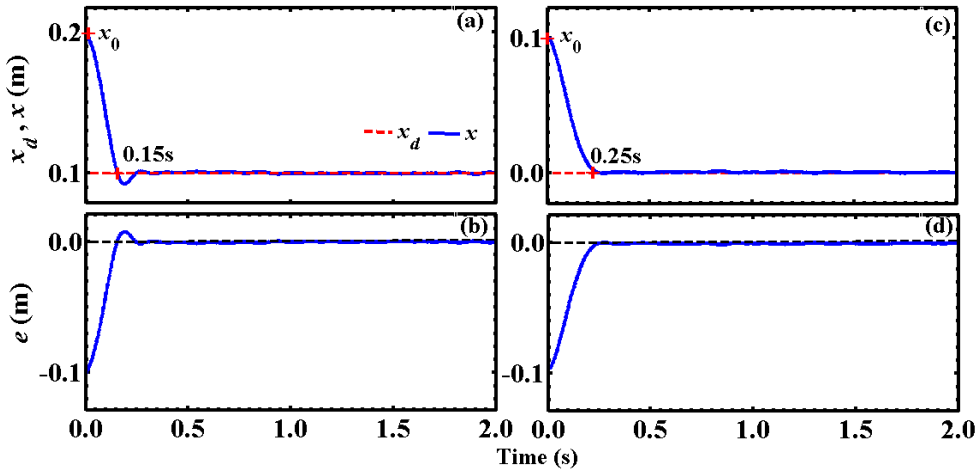

Figure 3.23: SMIC performances of 0.1m step responses (a, c) with their corresponding errors (b, d) for retraction motion at different x_0.

Table 3.7: SMIC performances interms of Rise time, IAE and CE for 0.1m step responses of extension and retarction at different x_0 depicted in Figs. 3.22 and 3.23

Type of Motion	x_0 (m)	Rise Time (s)	IAE (m-s)	CE (V^2 s)
Extension	0.0	0.33	0.017	32.26
Extension	0.1	0.62	0.024	54.71
Retraction	0.2	0.15	0.008	17.46
Retraction	0.1	0.25	0.009	20.09

(III) *Real time performances of SMIC with the combined motion of tracking and regulatory: saw-tooth response*

The saw-tooth demands studied in Figs. 3.24 and 3.25 for amplitude a respectively equal to 0.01m and 0.02m signify repeatative pairs of equal and opposite displacements put up in the form of constant velocity phase of retraction and a step displacement of extension. This demand form is mathemtically expressed as

$$x_d = x_0 + a(1 - \text{modulo}(2\pi f t, 2\pi)), \tag{3.16}$$

in terms of the initial position x_0 and the frequency f in Hz for the time t in s.The modulo returns the remainder after division of first number involving time by the next number in the argument.

SMIC results in Figs. 3.24 and 3.25 pertain to demand-response pairs for frequencies of 1, 2 and 3Hz shown in parts (a, d, g), corresponding errors in parts (b, e, h) and voltages in parts (c, f, i). In Fig. 3.24 additional results of demand-response pair, error

and voltage at 4Hz are illustrated in parts (j, k and l). Very low error excepting near the instants of step displacement demands clearly indicates the acceptability of SMIC design. Another very encouraging observation is the voltage variation far from the saturation values of $\pm 10\text{V}$ in most of the constant-velocity demand phases. Each voltage spike, which is lower for lower amplitude demand, quickly dies with initial large peak of positive voltage followed by much lower negative voltage crest. Clearly, each transient phase involving the peaks and crests widens with increase in frequency, whereas both the maximum error and voltage are seen to be independent of the frequency.

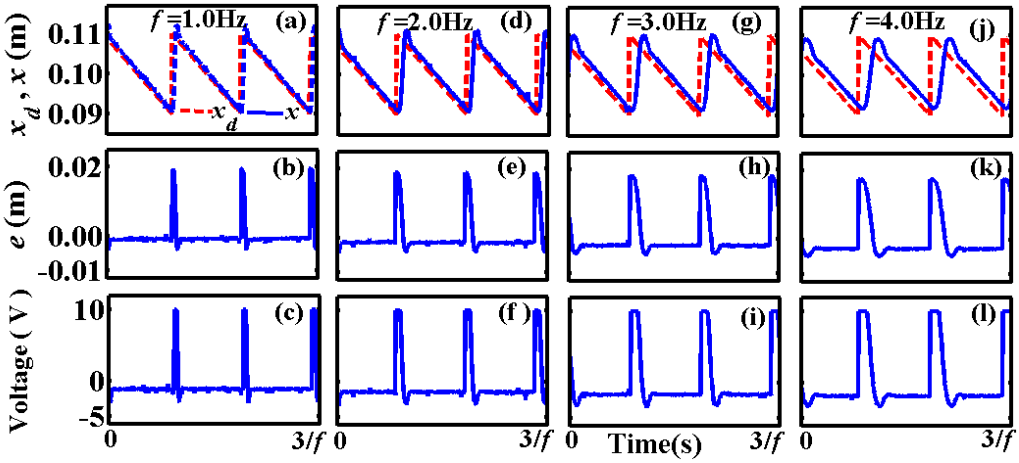

Figure 3.24: SMIC performance for 0.01m saw-tooth demands of 1.0 to 4.0 Hz.

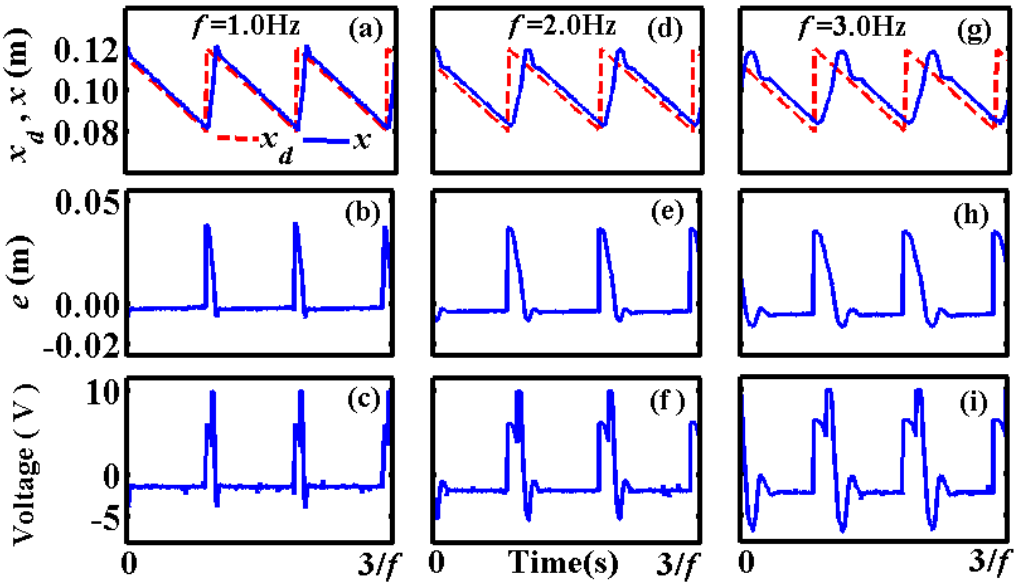

Figure 3.25: SMIC performance for 0.02m saw-tooth demands of 1.0 to 3.0 Hz.

(IV) *Real time performances of SMIC with arbitrary type of motion*

The usefulness of the designed SMIC for two very arbitrary tracking demands has been established by Figs. 3.26 and 3.27. The arbitary type of motion in the Fig. 3.26 has been made with the combination of the faster change of tracking demands. The faster tracks in Fig. 3.26 are applicable in a dynamic situation like path tracking by a robotic manipulator. The Fig. 3.27 involves large step changes and changeover among step, sinusoidal, and triangular patterns of position demands. The controller has been implemented acceptably even for the composite type of demand in Fig. 3.27. These demands are indeed more arbitrary than existing studies of Qiu et al. 2001. Figs. 3.26 and 3.27 indicate the absence of chattering, even for such complex demand tracks. Only the error spikes are apparent in the figures. Such performance in the face of a very arbitrary demand is a testimony of the controller robustness. The figures establish the controller SMIC to be very robust, even when applied for motion tracking of such a highly nonlinear system with a good deal of uncertainties.

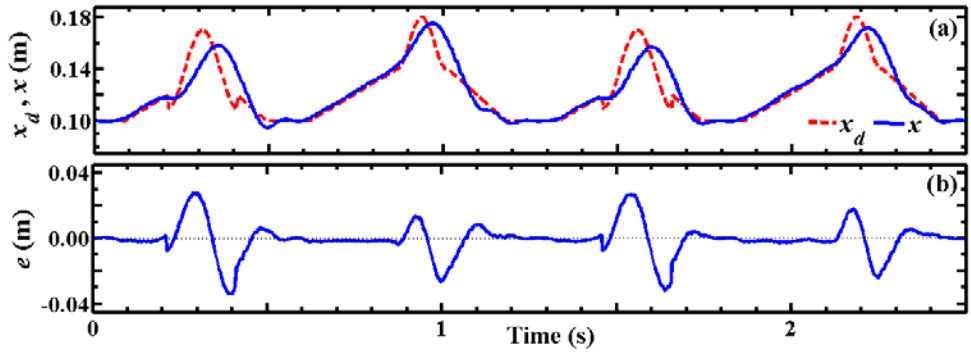

Figure 3.26: SMIC performance for arbitrary demand with higher speed of response.

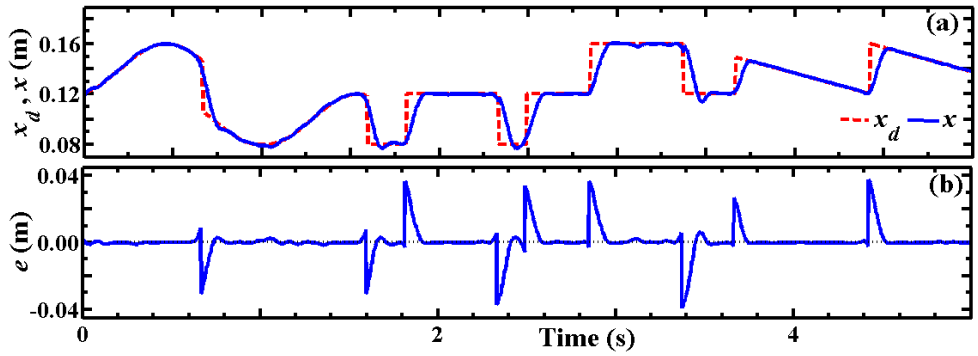

Figure 3.27: SMIC performance for arbitrary demand with lower speed of response.

3.6 Conclusion

In this chapter, the proposed FSMC and SMIC have been implemented in an electrohydraulic valve for tracking linear motion by the piston of a double-acting cylinder. For this purpose, the mathematical modeling and input linearization techniques specific for extracting the control voltage from the input of SMC corresponding to the nonlinear system model has been developed. Also, the offline parameter identification through RCGA has been accomplished prior to the real-time performance study. SMIC has yielded performance better than FSMC, Fuzzy-PI, SMC and IC. The benefits of lower steady state error of IC and higher disturbance rejection capability of SMC have led to the lowest IAE and CE in case of SMIC. In the region of near-zero error, chattering-free tracking has been realized for not imposing the discontinuous SMC involving sign function. The real time results have established the SMIC to be very robust, despite the uncertainties of deadband in the valve and stiction in the cylinder. The bandwidth has been determined to be about 6 to 7Hz with 0.02m amplitude sinusoidal response. The deterioration of the controller performances at high frequency can be attributed to the maximum bandwidth of 25Hz for the proportional valve rather than the limitation of the controller.

CHAPTER 4: REAL-TIME CONTROL OF ANGULAR MOTION BY EHAS

The real time control with the proposed controllers, namely FSMC and SMIC has been performed in this chapter with a laboratory scale EHAS producing angular rotation of link driven by an electrohydraulic cylinder. Similar to Chapter 3, this chapter describes the real time EHAS and its mathematical modeling to formulate the real time controller. The real coded GA has been implemented here to find out the optimum values of the system and control parameters for angular motion by EHAS. A comparison study of the controllers has been performed to investigate the suitable controller for this system. The real time performances of the suitable controller have been done with different types of tracking and regulatory motions.

4.1 Description and component specification of EHAS for Angular Motion

The real time experimental laboratory setup shown in Fig. 4.1 comprises of HPP, RTS, Host PC, LVDT, Electrohydraulic cylinder-valve arrangement. HPP, RTS and Host PC used for angular-motion EHAS in Fig 4.1 are same as that used for linear-motion EHAS mentioned in Section 3.1. However, the cylinder-valve arrangement and LVDT for angular-motion EHAS in Fig 4.1 are different than that of linear-motion EHAS in Fig. 3.1 of Section 3.1. PV used in angular-motion EHAS is servo type proportional valve or SPV, comprising of underlap spool valve, causing faster response and accurate control for the angular-motion EHAS. The sectional diagram of SPV adopted from the hydraulic catalogue of Bosch Rexroth 4WRPEH6 has been depicted in the inset of Fig. 4.1. Though there are some basic difference between PV used for the linear-motion EHAS in Section 3.1 and SPV used for the angular-motion EHAS in this section, the functional diagram and flow details of SPV have been considered as same as that of PV. The high pressured oil from pump flows through SPV and the cylinder C back to the tank at normal pressure.

In Fig 4.1, one end of the cylinder has been connected with a base platform by pin joint at S and another end has been linked by pin joint at Q with a link L. The link has been connected with the base platform by pin joint at P. The piston of the cylinder can produce the linear motion x which is responsible to make the angular motion θ of the link about the pin axis passing through the point P. LVDT attached to the piston in the

cylinder-valve arrangement measures x, which has been communicated to Host PC through IM of RTS. Host PC receives the user defined demand for the link as θ_d and calculates corresponding linear motion demand for piston-rod as x_d by using the kinematic modeling discussed in the next Section. The real time control voltage V has been developed in Lab View and communicated electronically through OM of RTS to ICE of SPV. There is a provision to attach different loads on a member fixed at the left-side of the top of the link. The component specifications of LVDT and electrohydraulic cylinder-valve arrangement have been taken from Hydraulics Catalogue of Actuator, Bosch Rexroth, CSH1MP5/40/28/250A3X and listed in Table 4.1. The detailing of link and load provision attachment has been given in Table 4.2.

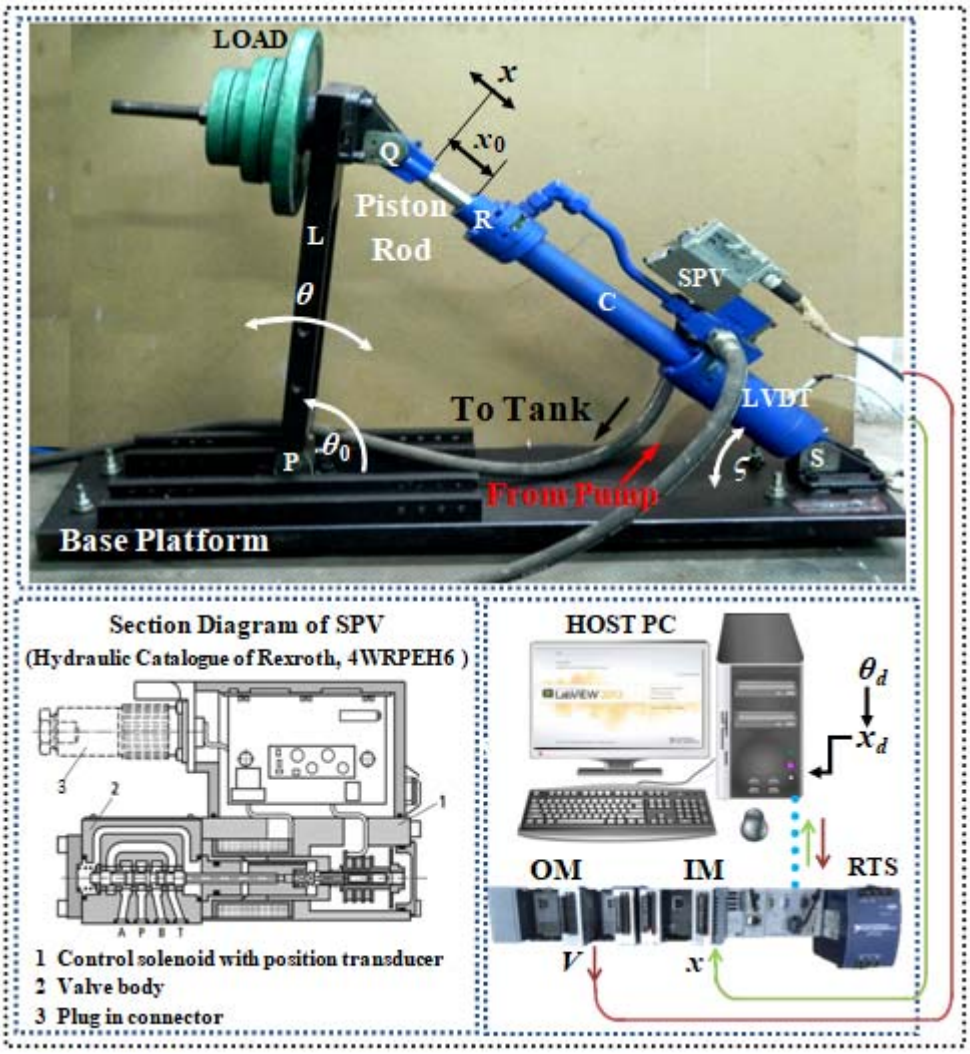

Figure 4.1: Laboratory set up for producing Angular motion of a link by an EHAS with sectional diagram of SPV adopted from hydraulic catalogue of Bosch Rexroth 4WRPEH6.

Table 4.1: Component specification of Electrohydraulic cylinder-valve arrangement with LVDT

Cylinder (C)	Manufacturer	Rexroth
	Serial No.	CSH1MP5/40/28/250A3X/P11CSUTZTFWWW
	Closed Length (RS)	0.732m
	Bore Diameter	ϕ 0.04m
	Rod Diameter	ϕ 0.028m
	Full Stroke	0.25m
	Piston mass	3kg
Servo Proportional Valve (SPV)	Manufacturer	Rexroth
	Serial No.	4WRPEH6C5B40L-20/G24K0/A1M
	Valve Type	4/4-way servo solenoid directional control valves, directly operated with electrical position feedback and on-board electronics(OBE)
	Bandwidth	60Hz
	Pressure rating	315bar (5000 psi)
	Spool Type	Hydraulic centre position by electrical valve closed loop control circuit Centre condition: Zero or underlap valve spool. Spring offset condition: P blocked, A, B, T connected
	Rated flow	40lpm at 1.0MPa total pressure drop at 2:1 area-ratio metered ports
	Command signal	$\pm$ 10volts
	Electrical power	24V DC amplifier supply
LVDT	Manufacturer	Rexroth
	Type	Magnetostrictive Position Sensor
	Range	0-250mm
	Input voltage	24V DC (-15/ +20 %)
	Output voltage	0-10V DC
	Linearity	$\leq \pm 0.02$ %, min $\pm$ 0.05(mm)

Table 4.2: Component specification of Link and load provision attachment

Link (L) and load provision attachment	Manufacturer	Locally Made
	Length (PQ)	0.572m
	Link Mass	12.2Kg
	Length and diameter of the load provision attachment rod	0.25m and 0.025m

4.2 Mathematical modeling of system

The mathematical modeling for EHAS in Fig. 4.1 has been dealt with kinematic modeling of experimental setup, dynamic of piston motion and modeling for chamber pressures of actuator.

4.2.1 Kinematic modeling of experimental set up

The kinematic modeling has been established here to calculate x_d from θ_d as well as θ from x. The angular motion by EHAS has been depicted with help of schematic representation of the link-mechanism setup in Fig 4.2. In Figs. 4.1 or 4.2, the cylinder closed length has been defined as RS. The length of base and link has been defined as PS and PQ respectively. It can be stated that base, link and cylinder make a triangle PQS with constant lengths of sides PQ as 0.572m and PS as 0.692m and variable length of side QS. The piston-rod motion x in the triangle PQS develops link motion θ about pin joint P. Of course, the angle made by the axis of cylinder with base is ς.

Now kinematic modeling with reference to the triangle PQS in Fig. 4.2 can be established to calculate x_d from θ_d as

$$x_d = \sqrt{(\mathrm{PQ})^2 + (\mathrm{PS})^2 - 2\,\mathrm{PQ.PS}\cos(\theta_0 + \theta_d)} - (\mathrm{RS} + x_0), \tag{4.1a}$$

where θ_0 is an initial angle made by link to the base for corresponding initial actuated motion by piston-rod x_0. Similarly the calculation θ can be obtained from x as

$$\theta = \cos^{-1}[\{\mathrm{PQ}^2 + \mathrm{PS}^2 - (\mathrm{RS} + x + x_0)^2\}/2\,\mathrm{PQ.PS}] - \theta_0. \tag{4.1b}$$

The calculations of the equations (4.1a) and (4.1b) have been processed in Lab View for the real time execution. Though calculated value of θ is only required to compare with θ_d but the value of x_d has been implemented in real time control to compare it with x so that the tracking error e can be established to produce the corresponding control voltage V.

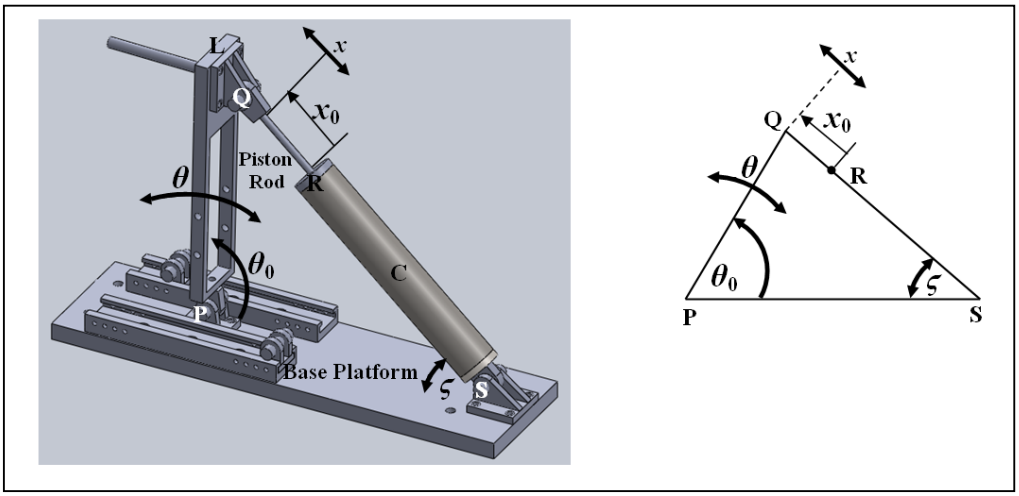

Figure 4.2: Schematic representation of the link-mechanism setup for Fig. 4.1.

4.2.2 Dynamic modeling of piston motion

Similar to the dynamic modeling of linear-motion EHAS in Section 3.2.1, the dynamic modeling of piston for angular-motion EHAS in Figs. 4.1 and 4.2 can represented as

$$\ddot{x} = \{P_1 A_{a1} - P_2 A_{a2} - m_a g \sin\varsigma - F_T\}/m_p \text{ for } V \geq V_0, \quad (4.2a)$$

and $$\ddot{x} = \{P_2 A_{a2} - P_1 A_{a1} - m_a g \sin\varsigma - F_T\}/m_p \text{ for } V < -V_0, \quad (4.2b)$$

where m_p is the mass of piston and m_a is the actuation-system mass between S and Q in Fig. 4.1 having the piston, cylinder, valve, LVDT and piping. The corresponding chamber pressure has been considered here as P_1 and P_2 with respective area A_{a1} and A_{a2} formulated in (1.1d) and (1.1e). The effect of gravitational acceleration g on m_a has been considered as $m_a g \sin\varsigma$ in the dynamic modeling of (4.2a-b). The effect of friction has not been considered here due to less frictional effect in the contact surface of cylinder-piston of actuator.

The external force F_T due to effect of torque along piston axis can be formulated as

$$F_T = [I_L\ddot{\theta} + \{(m_l/2) + m_w\} gl\cos(\theta + \theta_0)]/[l\sin(\theta + \theta_0 + \varsigma)], \quad (4.2c)$$

for dead load m_w, the centroidal mass moment of inertia I_L of the link of mass m_L and length l. Of course, the angle ς made by the cylinder with the base can be obtained as

$$\varsigma = \cos^{-1}[\{(\text{RS} + x + x_0)^2 + \text{PS}^2 - \text{PQ}^2\}/\{2(\text{RS} + x + x_0)\text{PS}\}]. \quad (4.2d)$$

4.2.3 Modeling for chamber pressures of actuator

The real time experiments have been performed with SPV depicted in the inset of Fig. 4.1. Though there are some differences between PV used for linear-motion EHAS and SPV used in the angular-motion EHAS, the corresponding flow details of SPV and the pressure equations have been considered as same as that of PV of Section 3.2.2. So the simplified pressure equations in (3.3a) to (3.3d) have been rewritten as

$P_1 = P_P - [(A_{a1}\dot{x})/\{C_v(V - V_0)\}]^2$ and $P_2 = P_T + [(A_{a2}\dot{x})/\{0.5C_v(V - V_0)\}]^2$

for $V \geq V_0$, (4.3a)

or $P_1 = P_T + [(A_{a1}\dot{x})/\{C_v(V + V_0)\}]^2$ and $P_2 = P_P - [(A_{a2}\dot{x})/\{0.5C_v(V + V_0)\}]^2$

for $V < -V_0$, (4.3b)

with the corresponding terms used as same that of linear-motion EHAS of Section 3.2.2. The real time control voltage V in (4.3a-b) has been extracted in the next section by implementing the same procedures as linear-motion EHAS mentioned in Section 3.3.

4.3 Input Linearization technique for Voltage Extraction model

By using the input linearization technique and other procedures adopted in Section 3.3, it can be stated that the existing set up is 2nd order system. The corresponding 2nd order dynamic equation in (4.2a-b) can be reframed with help of (4.3a-b) as

$$\ddot{x} = [P_P A_{a1} - \{A_{a1}^3 \dot{x}^2 / C_v^2 (V - V_0)^2\} - P_T A_{a2} - \{4A_{a2}^3 \dot{x}^2 / C_v^2 (V - V_0)^2\} - m_a g \sin\varsigma - F_T]/m_p \text{ for } V \geq V_0, \quad (4.4a)$$

$$\text{or } \ddot{x} = [P_P A_{a2} - \{4A_{a2}^3 \dot{x}^2 / C_v^2 (V + V_0)^2\} - P_T A_{a1} - \{A_{a1}^3 \dot{x}^2 / C_v^2 (V + V_0)^2\} - m_a g \sin\varsigma - F_T]/m_p \text{ for } V < -V_0. \quad (4.4b)$$

Similar to that of linear-motion EHAS, the nonlinear system dynamic equations in (4.4a-b) can be reorganized to represent d, u and V in the form consistent with (2.9a) to (2.9c) as

$$d = \ddot{x}_d + \lambda_1 \dot{x}_d + \lambda_0 x_d - \{(P_P A_{a1} - P_T A_{a2})/m_p\} - \lambda_1 \dot{x} + \lambda_0 x \text{ for } V \geq V_0, \quad (4.5a)$$

$$\text{or } d = \ddot{x}_d + \lambda_1 \dot{x}_d + \lambda_0 x_d - \{(P_P A_{a2} - P_T A_{a1})/m_p\} - \lambda_1 \dot{x} + \lambda_0 x \text{ for } V < -V_0, \quad (4.5b)$$

$$u = [\{\dot{x}^2/(V \pm V_0)^2\}\{(A_{a1}^3/C_v^2) + (4A_{a2}^3/C_v^2)\} + m_a g \sin\varsigma + F_T]/m_p, \quad (4.5c)$$

$$\text{and } V = \dot{x}\sqrt{[\{(A_{a1}^3/C_v^2) + (4A_{a2}^3/C_v^2)\}/\{(m_p u - m_a g \sin\varsigma - F_T)\}]} + V_0 \operatorname{sgn}(\dot{x}). \quad (4.5d)$$

The disturbance formulation (4.5a) or (4.5b) involves the output x and its derivative along with disturbances parameters in the form of pump pressure, tank pressure, actuated mass, the demand, its first and second derivatives. The linearized input (4.5c) involves the system parameter vector containing the valve coefficient and some of the disturbance parameters. This justifies the use of compensation through (2.15a) and (2.15c) or (2.15b) and (2.15d). The linearized input involves the extracted voltage in an explicit form together with the control vector containing the parameters mentioned in (2.17a) or (2.17b) in an implicit form.

The parameters required to find out the input linearized extracted voltage V from (4.5d) have been mentioned as

(a) ***Constant parameters,*** $\mathrm{C}_{\text{angular}}$ **:** The constant parameters A_{a1}, A_{a2}, m_p, m_a and g are directly involved to construct V whereas m_w, m_L and l are required to formulate F_T which is again required to extract V. The value of x_0, θ_0 and each side of the triangle PQS have been used to find out the angle ς which is again used to extract V. These constant parameters have been represented as

$$\mathrm{C}_{\text{angular}} = (A_{a1}\ \ A_{a2}\ \ m_p\ \ m_a\ \ g\ \ m_w\ \ m_L\ \ l\ \ \mathrm{PQ}\ \ \mathrm{RS}\ \ \mathrm{PS}\ \ x_0\ \ \theta_0)\,. \tag{4.6a}$$

where A_{a1} and A_{a2} can be extracted from the specifications of cylinder given in Table 4.1 and using their corresponding formulations used in (1.1d) and (1.1e) as

$$A_{a1} = \pi(0.04)^2/4 = 0.0013\mathrm{m}^2\,, \tag{4.6b}$$

and $$A_{a2} = \pi\{(0.04)^2 - (0.028)^2\}/4 = 0.00064\mathrm{m}^2\,. \tag{4.6c}$$

Tables 4.1 and 4.2 provide m_p as 3kg, m_L as 12.2kg, l as 0.572m, PQ as 0.572m and RS as 0.732m. The mass of actuation-system m_a has been measured as 20kg. The value of m_w has been provided in the corresponding real time execution and g has been taken as $10\mathrm{ms}^{-2}$. Table 4.1 reveals that stroke length of the piston is 0.25m. All the experiments for angular-motion EHAS have been stared from mid span of the stroke length which is in term of x_0 as 0.125m and the corresponding θ_0 as 85^0. The motion of link from θ_0 has been considered here as its zero position and any anticlockwise rotation from its zero position has been defined as its positive rotation and vice versa. From the kinematic equation, it can be revealed that the link can rotate maximum $\pm 14^0$ with respect to θ_0 by employing full stroke of the piston.

(b) *System parameters,* $\mathrm{q}_{\text{angular}}$ **:** The value of I_L is required to construct F_T which is again used to extract V. The other system parameters are C_v and V_0 used in the voltage extraction model. So the system parameters have been represented as

$$\mathrm{q}_{\text{angular}} = (I_L \;\; C_v \;\; V_0)\,. \tag{4.7}$$

(c) *Control parameter,* $\hat{\psi}_{\text{FSMC}}$ ***or*** $\hat{\psi}_{\text{SMIC}}$**:** Similar to the linear-motion EHAS, the corresponding control parameters in $\hat{\psi}_{\text{FSMC}}$ and $\hat{\psi}_{\text{SMIC}}$ have been required to construct u which is again used to formulate V.

The system parameters $\mathrm{q}_{\text{angular}}$ and the corresponding control parameters $\hat{\psi}_{\text{FSMC}}$ or $\hat{\psi}_{\text{SMIC}}$ together can make the parameter vector **p** mentioned in Fig. 1.13. These system and control parameters have been optimized in next section similar to the identification of the parameters for the linear-motion EHAS described in Section 3.4.

4.4 Identification of System and Control Parameters

Similar to Section 3.4, RCGA (Sarkar et al., 2013b) has been implemented to identify the optimum values of the corresponding parameters of $\mathrm{q}_{\text{angular}}$, $\hat{\psi}_{\text{FSMC}}$ and $\hat{\psi}_{\text{SMIC}}$. In each case of the identification process the first generation is created as a random distribution of ten sets of parameter values over a specified bound for each. For the next generations, another ten sets are obtained by aiming a minimization composed as a difference between a model prediction and its experimental variation with a set PID controller for 1Hz sinusoidal motion of 1^0 amplitude for link motion starting from zero position of the link.

4.4.1 Identification of System Parameters

To estimate the system parameters, the index to be minimized is taken as

$$\text{IAE} = \int_0^T |\,\theta_d - \theta\,|\,dt\,, \tag{4.8}$$

where θ is the link angle for the corresponding piston motion x predicted by the open-loop model (4.4a) and (4.4b) for each set of parameters in a generation and θ_d is taken as the experimental response of PID for a sinusoidal demand over a cycle time T. The experimental value of angle θ_d has been obtained here by using the kinematic equation (4.1b) corresponding to LVDT reading of PID performance. The constant parameters and the experimental variation of the voltage V have been fed in (4.4a) and (4.4b) as excitation input in each prediction run.

Implementing the optimization process involving the minimization of (4.8), the convergence of IAE, as shown in Fig. 4.3, is obtained for all 10 sets of parameter values after every 5 generations. The optimizer yielded the system parameters as

$$q_{angular} = (0.542 \;\; 0.5 * 10^{-7} \;\; 0.5), \tag{4.9a}$$

with their respective unit as kg-m^2, m^3/(s.V.√Pa) and V extracted from the set yielding the lowest IAE after 20 generations.

The corresponding $\mathbf{b}_l$ and $\mathbf{b}_u$ for $q_{angular}$ have been chosen respectively as

$$q_{angular}(\text{lower}) = (0.200 \;\; 0.2 * 10^{-8} \;\; 0.2), \tag{4.9b}$$

and $$q_{angular}(\text{upper}) = (0.900 \;\; 0.9 * 10^{-7} \;\; 1.0). \tag{4.9c}$$

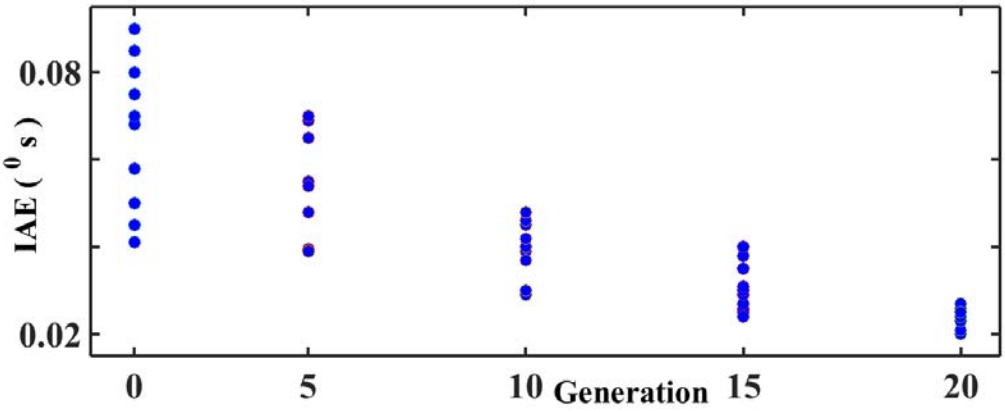

Figure 4.3: Identification of system parameters for angular-motion EHAS through optimization.

4.4.2 Identification of Control Parameters

The estimation of the control parameters has been performed by using the CE indexes formulated in (3.10a) and (3.10b) of Section 3.4.2. The identification process has been done here by minimizing

$$|\text{CE} - \text{CE}_p| = \int_0^T |V^2 - V_p^2| \, dt. \tag{4.10}$$

with V_p predicted from (4.5d). In (4.5d), sequential use has been made of F_T, variation of LVDT reading, constant parameters $C_{angular}$, optimized $q_{angular}$ and corresponding u.

The identification process of control parameters for FSMC and SMIC have been done in next similar to that of linear-motion EHAS in Section 3.4.2.

(I) ***Identification of control parameters of FSMC***

Similar to the linear-motion EHAS, the set (2.32d), (2.13), (2.14a) and (2.15a) has been used in FSMC input (2.12a) with chosen values of Hurwirtz coefficient as

$$\lambda = (2 \;\; 0.5). \tag{4.11a}$$

The parameters in f_{FSMC} have been chosen here as

$$f_{FSMC} = (1000\;\; 1000\;\; 1000\;\; 1000\;\; 1000\;\; 2000). \tag{4.11b}$$

The corresponding $\mathbf{b}_l$ and $\mathbf{b}_u$ for ψ_{FSMC} have been chosen respectively as

$$\psi_{FSMC}(\text{lower}) = (1000\;\; 1000\;\; 1000\;\; 1000\;\; 1000\;\; 1000\;\; 0\;\; 0\;\; 0\;\; 0\;\; 0$$
$$-4\;\; -3\;\; -2\;\; -1\;\; 0\;\; 5000), \tag{4.11c}$$

and $\psi_{FSMC}(\text{upper}) = (10000\;\; 5000\;\; 5000\;\; 5000\;\; 5000\;\; 5000\;\; 2\;\; 3\;\; 4\;\; 5\;\; 6$

$$4\;\; 5\;\; 6\;\; 8\;\; 10\;\; 10000). \tag{4.11d}$$

Fig. 4.4 shows the convergence of $|\,CE - CE_p\,|$ for all 10 sets of parameter values after every 5 generations by using the corresponding values in (4.11a-d). The optimizer yields the corresponding optimized parameters of $\psi_{FSMC}(\text{initial})$ as

$$\psi_{FSMC}(\text{initial}) = (5000\;\; 2000\;\; 2000\;\; 2000\;\; 2000\;\; 2000\;\; 0.7\;\; 0.4\;\; 0.3\;\; 0.1\;\; 0.01$$
$$0\;\; 1\;\; 2\;\; 3\;\; 4\;\; 5000), \tag{4.11e}$$

extracted from the set yielding the lowest value of $|\,CE - CE_p\,|$ after 20 generations.

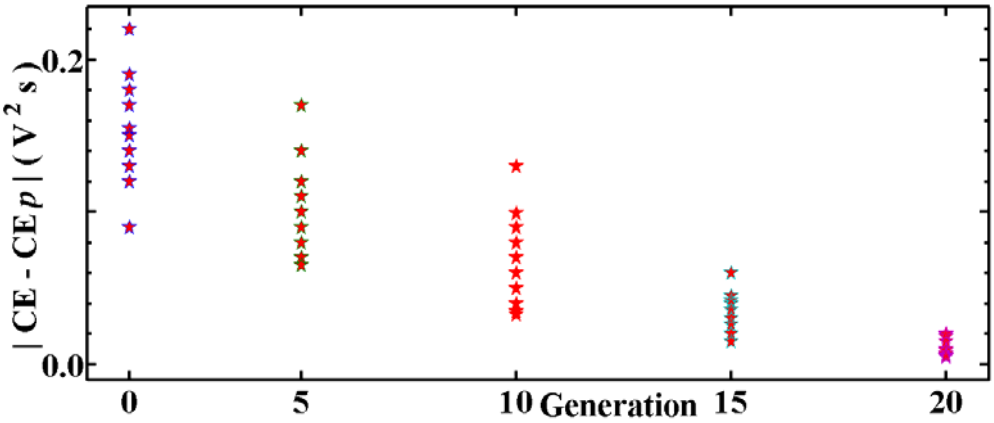

Figure 4.4: Identification of control parameters of FSMC for angular-motion EHAS through optimization.

(II) ***Identification of control parameters of SMIC***

The set (2.32d), (2.16) and (2.15b) has been used in SMIC input (2.12b) for identification of control parameters of SMIC. The values of Hurwirtz coefficient have been chosen as

$$\lambda = (2 \;\; 0.5)\,. \tag{4.12a}$$

The parameters in f_{SMIC} have been chosen here as

$$f_{SMIC} = (1000 \;\; 1000 \;\; 2000)\,. \tag{4.12b}$$

The corresponding $\mathbf{b}_l$ and $\mathbf{b}_u$ for ψ_{SMIC} have been chosen respectively as

$$\psi_{SMIC}(\text{lower}) = (1000 \;\; 5000)\,, \tag{4.12c}$$

$$\text{and } \psi_{SMIC}(\text{upper}) = (10000 \;\; 10000)\,. \tag{4.12d}$$

Fig. 4.5 shows the convergence of $|\,CE - CE_p\,|$ for all 10 sets of parameter values after every 5 generations by using the corresponding values in (4.12a-d). The optimizer yields the corresponding parameters in $\psi_{SMIC}(\text{initial})$ as

$$\psi_{SMIC}(\text{initial}) = (5000 \;\; 5000)\,, \tag{4.12e}$$

extracted from the set yielding the lowest value of $|\,CE - CE_p\,|$ after 20 generations.

The real time execution of FSMC and SMIC for angular motion by EHAS has been performed in the next section with the optimized values of system and control parameters.

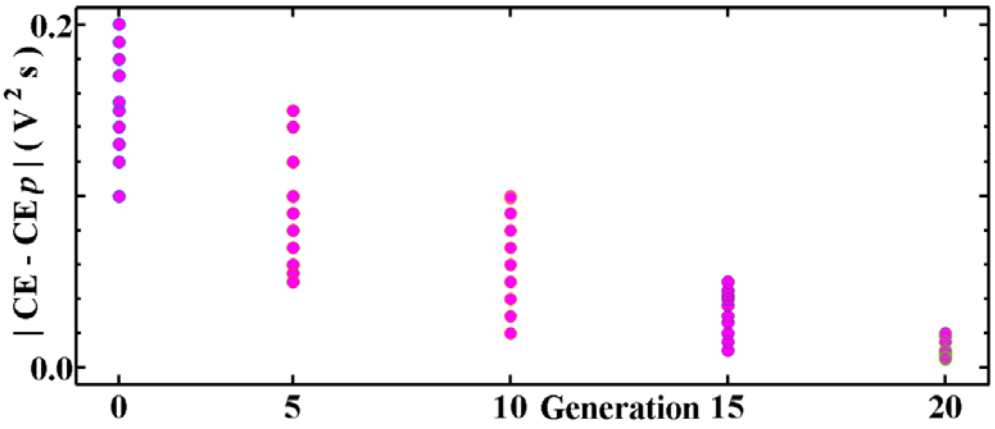

Figure 4.5: Identification of control parameters of SMIC for angular-motion EHAS through optimization.

4.5 Results and Discussion

The real time results for angular-motion EHAS with the proposed adaptive controllers FSMC and SMIC have been depicted in this section. For conducting the real time experiments, NI LabView13.0.1 Professional has been used in the Host PC to develop the motion control software and interfacing it with the real-time system. The user defined demand θ_d has been fed to Labview and the corresponding x_d has been calculated by using the kinematic modeling formulated in (4.1a). The real time system response x measured by LVDT has been communicated to Labview through IM of RTS and the corresponding θ has been formulated in Labview through the kinematic modeling of (4.1b). The tracking error e has been formulated by using x_d together with LVDT response x at the same sampling rate as of linear-motion EHAS. The input linearized control voltage V has been extracted in Labview and this extracted control voltage has been communicated through OM of RTS to the control card of SPV to get the desired motion. The control voltage V has been formulated with help of the constant parameters, the optimized system and control parameters.

The corresponding steps for adaptation process have been discussed in the next section along with the individual controller architecture followed by the controller selection process and the real time results. The real time experiments for the angular-motion EHAS have been performed with the setup described by Fig. 4.1 at 8MPa PRV setting with 50lpm flow rate. An external mass m_w of 80Kg has been used here for the real time experimentations. The experimental plan for this system has been organized as

(a) Controller Architecture for adaptation of FSMC.

(b) Real time adaption of FSMC control parameters for 1Hz sinusoidal motion with 0.02m amplitude demand.

(c) Controller Architecture for adaptation of SMIC.

(d) Real time adaptation of SMIC control parameters for 1Hz sinusoidal motion with 0.02m amplitude demand.

(e) Selection of suitable Controller for real time performances

(f) Real time performances with suitable controller for different types of tracking, regulatory and their combined motions.

4.5.1 Controller Architecture for Adaptive Control

The construction of the corresponding controller architecture for angular-motion EHAS is similar to that of linear-motion EHAS mentioned in Section 3.5.1.There are additional blocks are required in the controller architecture to represent the kinematic modeling for the angular-motion EHAS. The corresponding adaptive formulation steps along with an experimental result showing adaption of the control parameter for each case have been performed in next.

(I) ***Controller Architecture for real time adaptation of FSMC***

The controller architecture for FSMC with the angular-motion EHAS has been depicted in Fig. 4.6 which involves the corresponding adaption steps as similar as that of FSMC for linear-motion EHAS in Section 3.5.1. The adaptation steps (a) to (d) of FSMC for the linear-motion EHAS have been adopted for angular-motion EHAS. The succeeding steps for the angular-motion EHAS are

e) Extract the control voltage from (4.5d) by using the input-linearizing control $\hat{u}_{\text{FSMC}}$, constant parameters in $\text{C}_{\text{angular}}$, optimized system parameters in $\text{q}_{\text{angular}}$

f) Execute the real time system with the extracted control voltage V.

g) Implement the kinematic modeling (4.1a) and (4.1b) to formulate x_d and θ.

h) Formulate the error e by using the user defined demand x_d and the system response x measured by LVDT feedback.

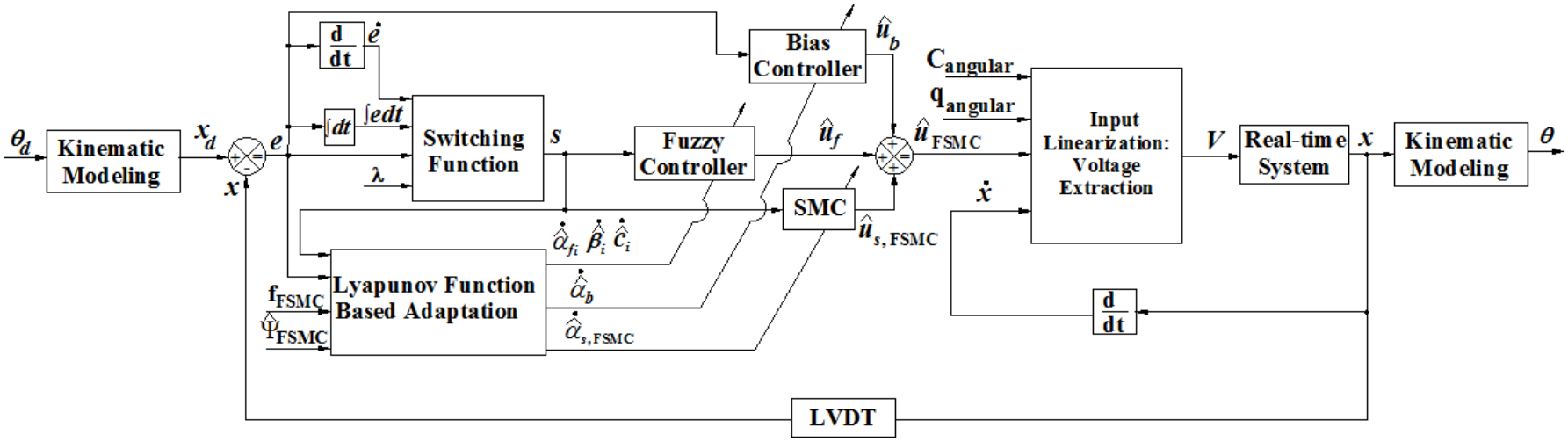

Figure 4.6: Schematic architecture of proposed adaptive FSMC for angular- motion EHAS.

The real time adaptations of the control parameters of FSMC with 1Hz sinusoidal motion of 1^0 amplitude for angular-motion EHAS have been depicted in Figs. 4.7 and 4.8. The adaptations of $\hat{\alpha}_b$ and $\hat{\alpha}_{s,\text{FSMC}}$ have been illustrated in Figs. 4.7(d, e) and adaptations of $\hat{\alpha}_{fi}$, $\hat{\beta}_i$ and $\hat{c}_i$ have been mentioned in Fig. 4.8(b-p). Fig. 4.7(a) shows the real time responses of link motion and Fig. 4.7(b) reveals the corresponding piston motion. For the same link demand in Fig. 4.7(a), the corresponding error has been reflected in both of Figs. 4.7(c) and 4.8(a). Figs. 4.7(d, e) and 4.8(b-p) reveal that the corresponding adaptions for FSMC with angular- motion EHAS follow the similar type of trends observed for the adaptation of FSMC with linear-motion EHAS in Section 3.5.1. The observed trends of increase in $\hat{\alpha}_{s,\text{FSMC}}$ and non-monotonic changes in $\hat{\alpha}_b$, $\hat{\alpha}_{fi}$, $\hat{\beta}_i$ and $\hat{c}_i$ are consistent with the findings of Figs. 4.7(d, e) and Figs. 4.8(b-p). Few activation points with green color and few deactivation points with red color have been pointed out in Figs. 4.7(c-e) and Figs. 4.8(a-p).

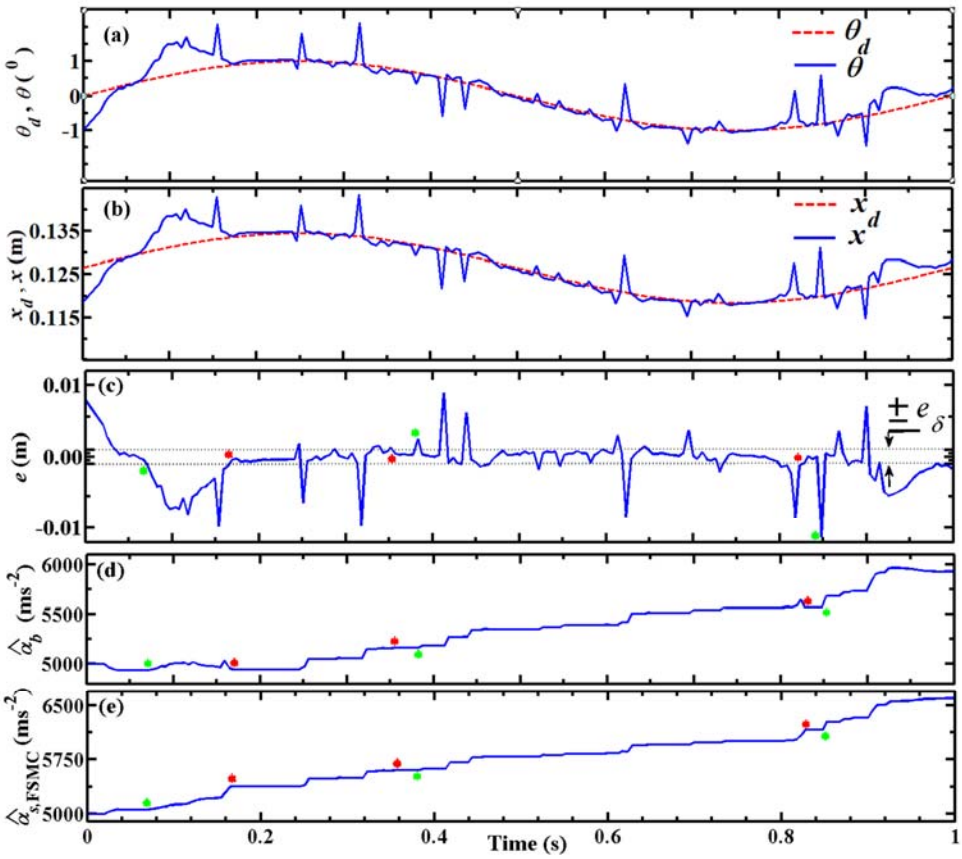

Figure 4.7: Real-time adaptation of $\hat{\alpha}_b$ and $\hat{\alpha}_{s,\text{FSMC}}$ for 1Hz sinusoidal motion with 1^0 amplitude demand.

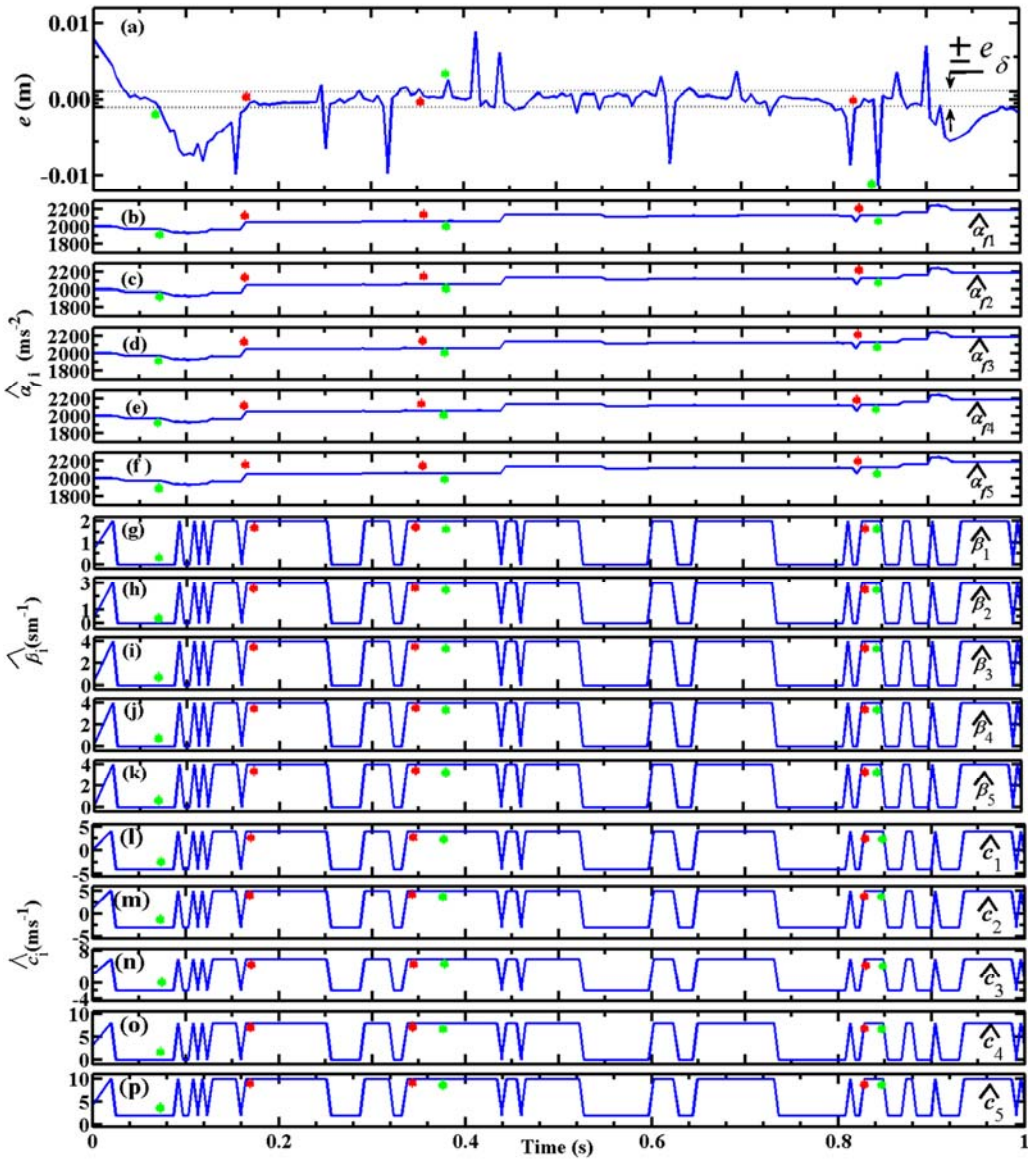

Figure 4.8: Real-time adaptation of $\hat{\alpha}_{fi}$, $\hat{\beta}_i$ and $\hat{c}_i$ for 1Hz sinusoidal motion with 1^0 amplitude demand.

(II) ***Controller Architecture for real time adaptation of SMIC***

The controller architecture for the real time adaptation of SMIC with angular-motion EHAS has been represented in Fig. 4.9 adopting the adaptive steps (a) to (c) of SMIC with linear-motion EHAS mentioned in Section 3.5.1. The succeeding steps for SMIC have been listed as

d) Extract the control voltage from (4.5d) by using the input-linearizing control $\hat{u}_{\text{SMIC}}$, constant parameters in $\text{C}_{\text{angular}}$, optimized system parameters in $\text{q}_{\text{angular}}$

e) Execute the real time system with the extracted control voltage V.

f) Implement the kinematic modeling (4.1a) and (4.1b) to formulate x_d and θ.

g) Formulate the error e by using the user defined demand x_d and the system response x measured by LVDT feedback.

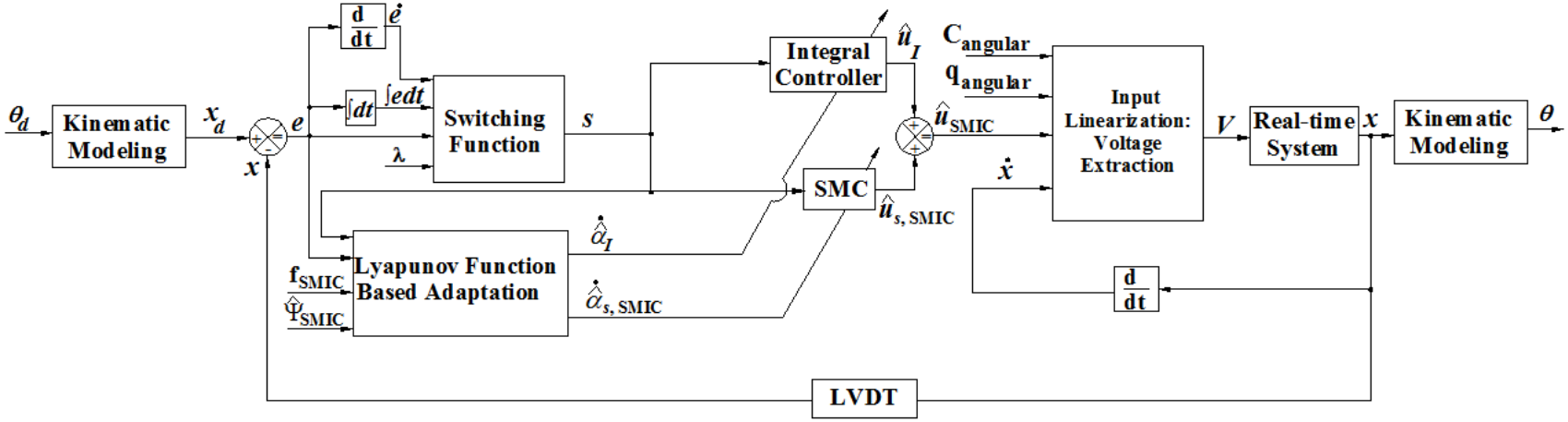

Figure 4.9: Schematic architecture of proposed adaptive SMIC for angular- motion EHAS.

Implementing the adaptation steps for SMIC, the corresponding adaptions of the control parameters have been represented in Fig. 4.10 with 1Hz sinusoidal motion of 1^0 amplitude. The real time adaptions of $\hat{\alpha}_I$ and $\hat{\alpha}_{s,\text{SMIC}}$ have been reflected respectively in Fig. 4.10(d) and Fig. 4.10(e) for the corresponding link motion in Fig. 4.10(a), piston motion in Fig. 4.10(b) and the error dynamic of piston motion in Fig. 4.10(c). The corresponding adaptions for SMIC with angular-motion EHAS follow the similar type of trends observed for adaptation of SMIC with linear-motion EHAS in Section 3.5.1. It can be observed from Fig. 4.10 that the adaptions have been started from the corresponding initial values and continue before reaching to the e_δ of ±2mm where the adaptation remains suspended and the control parameters sustain their last updated values. The increasing trends of $\hat{\alpha}_{s,\text{SMIC}}$ and non-monotonic adaptation of $\hat{\alpha}_I$ have been also depicted in Fig. 4.10.

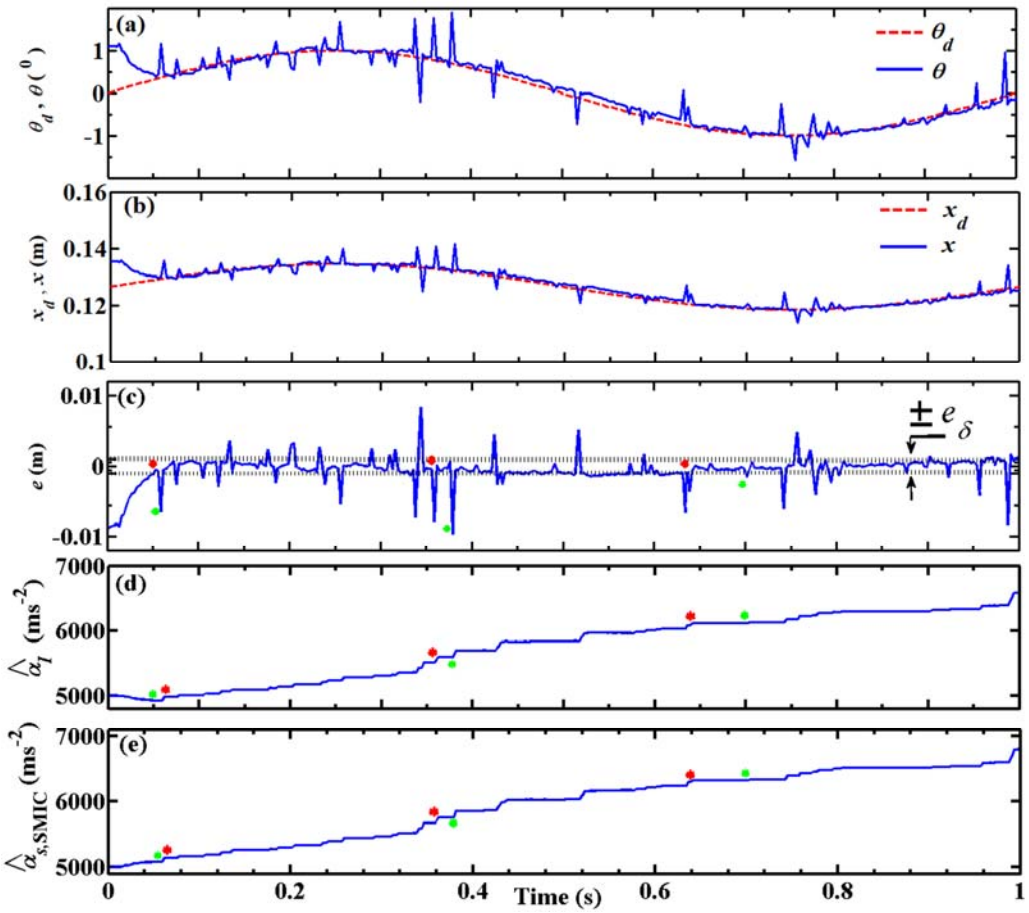

Figure 4.10: Real-time adaptation of SMIC parameters for 1Hz sinusoidal motion with 1^0 amplitude demand.

4.5.2 Selection of suitable Controller for real time performances

The selection of suitable controller for the real time performances with angular-motion EHAS has been done by the same procedures followed by the linear-motion EHAS in Section 3.5.2. The comparison study has been performed with FSMC, SMIC, SMC, IC and Fuzzy-tuned PI (Dasmahapatra et al., 2015). Similar to the linear-motion EHAS, the corresponding parameters of FSMC and SMIC for angular-motion EHAS have been taken from their corresponding optimized values identified in Section 4.4. The optimized parameters correspond to the initial value of $\hat{\alpha}_s$ for SMC and $\hat{\alpha}_I$ for IC are respectively as 6000ms^{-2} and 5000ms^{-2}.

The comparison study of the controller has been depicted in Fig. 4.11 representing the corresponding value of IAE and CE for different controllers with 1^0 sinusoidal motion with frequency variation. The controller selection has been done with help of the defined indexes IAE in (4.8) and CE in (3.10a). The corresponding formulation of IAE has been attained through the user defined link demand θ_d and the actual link position θ calculated by (4.1b). The calculation of CE has been performed with the control voltage V formulated by using (4.5d). The criterion for the best controller is the one with the lowest value of these indexes.

Fig. 4.11 shows higher IAE and CE variations for IC compare to SMC and lower values of IAE for FSMC compare to SMC, IC and Fuzzy-tuned PI. This establishes that SMC can tackle with different types of approximation and uncertainties associated with the system and controller modeling. The benefits of lower steady error of IC and higher disturbance rejection capability of SMC have yielded the lowest IAE and CE in case of SMIC for the angular-motion EHAS similar to that of linear-motion EHAS in Section 3.5.2. Fig 4.11 reveals that there is an increasing tendency of CE with increase of frequency for each controller. The observed increase in IAE with lowering of frequency between 3 and 4Hz could be due to the effect of Stribeck friction (Rahmat et al., 2011). Fig. 4.11 clearly reveals that the most suitable controller for the real time performances of the angular-motion EHAS is SMIC. The next section has been dealt with the real time performances of SMIC for angular-motion EHAS.

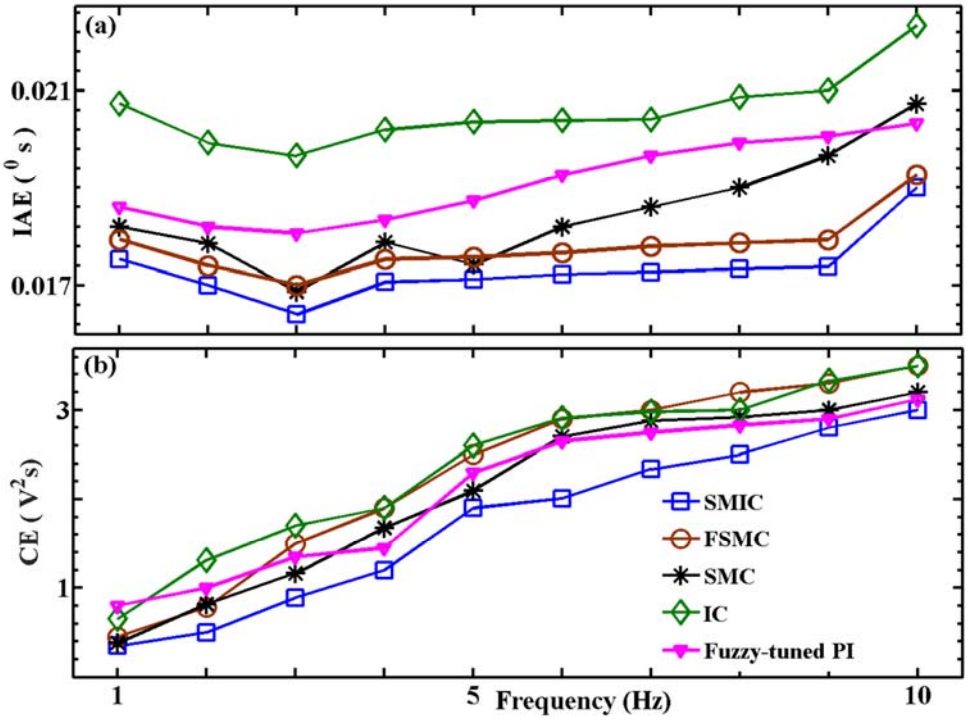

Figure 4.11: Comparison of IAE and CE for different controllers of 1^0 sinusoidal motion with frequency variation.

4.5.3 Real time performances with SMIC

The real time performances of SMIC have been discussed in this section with the time domain variations of link response, its error and the corresponding control voltage. The effect of different dead load on the control voltage has been studied with the sinusoidal motion. The step and saw-tooth displacement demands have been studied to capture controller performance for more challenging demands. The controller robustness has been verified with arbitrary motions. In the time domain variation of Figs. 4.12 to 4.25, the link demand has been indicated as θ_d and the corresponding link response has been mentioned as θ .

(I) ***Real time performances of SMIC with tracking motion: sinusoidal response***

The sinusoidal motion has been defined here as

$$\theta_d = \theta_0 + a\sin(2\pi f t), \tag{4.13}$$

in terms θ_0, amplitude a in degree (^{0}) and frequency f in Hz for time t in s.

The controller performances of sinusoidal motion for different frequency responses have been illustrated in Figs. 4.12 to 4.18. SMIC responses of 1^0 sinusoidal motions

have been depicted in Figs. 4.12 and 4.13 with the demand-response pairs in parts (a, d, g), corresponding errors in parts (b, e, h) and the voltages in parts (c, f, i) for frequency demands of 3.0Hz to 11.0 Hz. The link motion with 1^0 is typically useful for the aircraft grade application for the aileron movement when the flight is in high altitude. The sinusoidal responses in Figs. 4.12 and 4.13 indicate that the control voltage has been saturated in ± 10V with 9Hz response and the corresponding error has been increased with higher rate. Higher error for the 11Hz sinusoidal demand in comparison to those for 9 and 10Hz demands evident in Figs. 4.13 can be attributed to longer periods of saturation of the control voltage.

As shown in Figs. 4.12 and 4.13, the increase of phase lag between demand and response with increase in frequency could be the reason for increase in IAE in Fig. 4.11. This feature is evident in Fig. 4.14 showing the gain-phase plot with variation in frequency of the sinusoidal demand with 1^0 of amplitude. Fig. 4.14 reveals the bandwidth to be about 10Hz which is more than that of linear-motion EHAS. This can be attributed for the higher-grade servo proportional valve with the angular-motion EHAS.

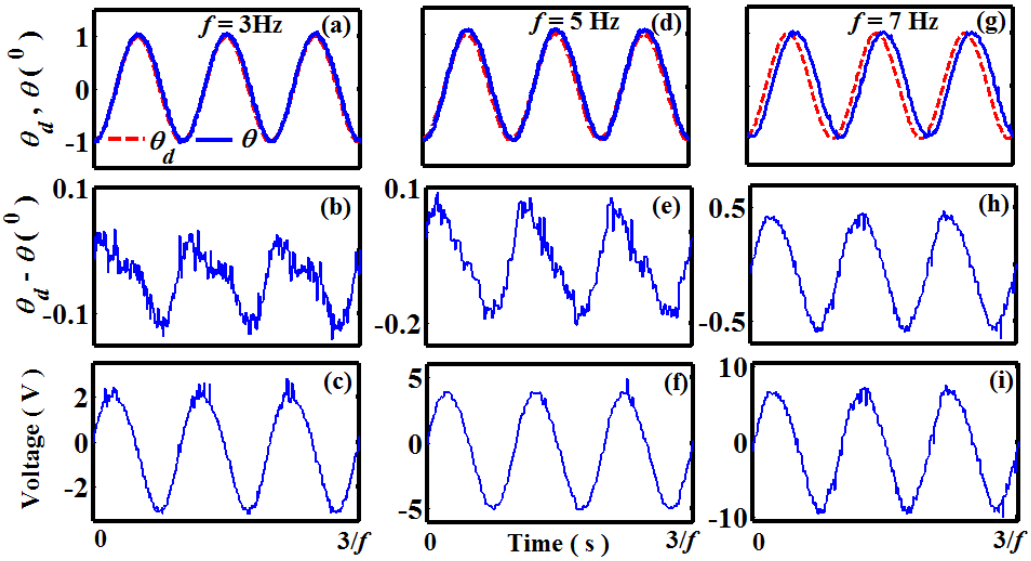

Figure 4.12: SMIC responses for 1^0 sinusoidal motions (a, d, g) with corresponding errors (b, e, h) and voltages (c, f, i) with frequency demands of 3.0, 5.0 and 7.0 Hz.

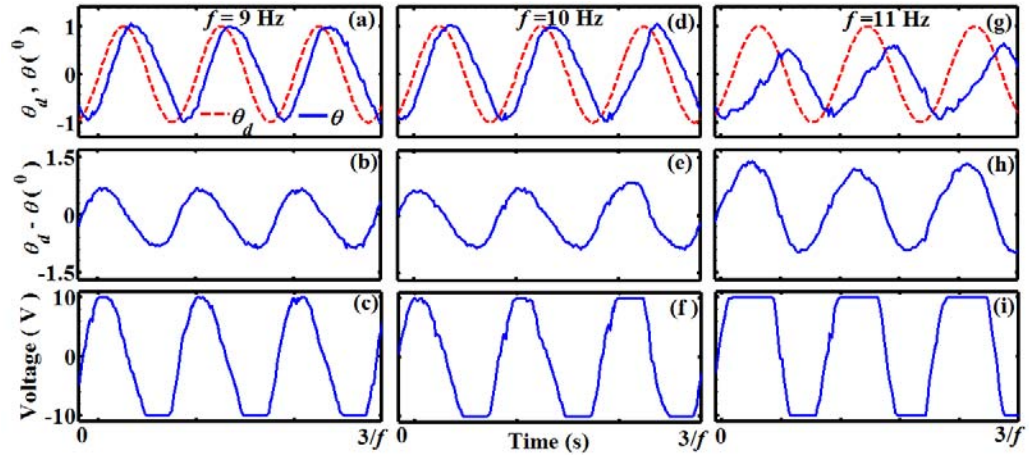

Figure 4.13: SMIC responses for 1^0 sinusoidal motions (a, d, g) with corresponding errors (b, e, h) and voltages (c, f, i) with frequency demands of 9.0, 10.0, 11.0 Hz.

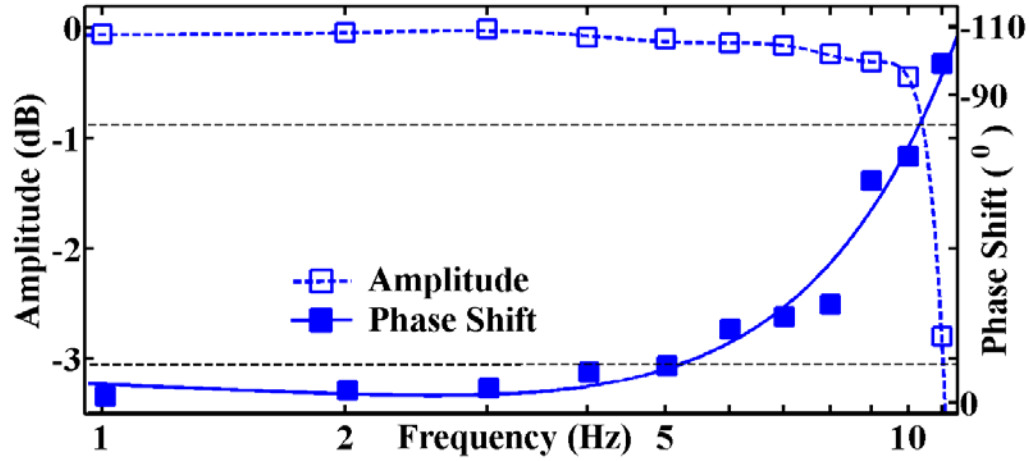

Figure 4.14: Variation of gain-phase plot with frequency for SMIC controller for 1^0 sinusoidal demand.

In Fig. 4.15, SMIC performances have been depicted interms of IAE, CE (a) and $|V|_{max}$ (b) for different dead loads with 1^0 sinusoidal motions at 10Hz. Longer periods of voltage saturation over each cycle of 10Hz excitation have been reflected for dead load increasing beyond 75kg leading to the associated sharp increase in IAE. Prior to the saturation, the increase in IAE and the peak voltage with increase in dead load has presumably arisen from higher joint friction and load inertia respectively.

The controller performances have been portrayed for high-amplitude-low-frequency sinusoidal motions in Figs. 4.16 and 4.17. The low-amplitude-high-frequency sinusoidal motions have been shown in Fig. 4.18. High-amplitude-low-frequency tracking near the ground and low-amplitude-high-frequency tracking during high-altitude maneuvering are typical of aircraft flight control. The higher amplitude

responses, as shown in Figs. 4.16 and 4.17, reveal that the error has been increased at higher rate beyond the frequency of 0.5Hz. Though the chattering has been eliminated in the responses observed in Figs. 4.16 to 4.18, the deterioration of the controller performances at high frequency in Figs. 4.18(e,f) can be attributed to the voltage saturation problem, as explained in the context of Fig. 4.13.

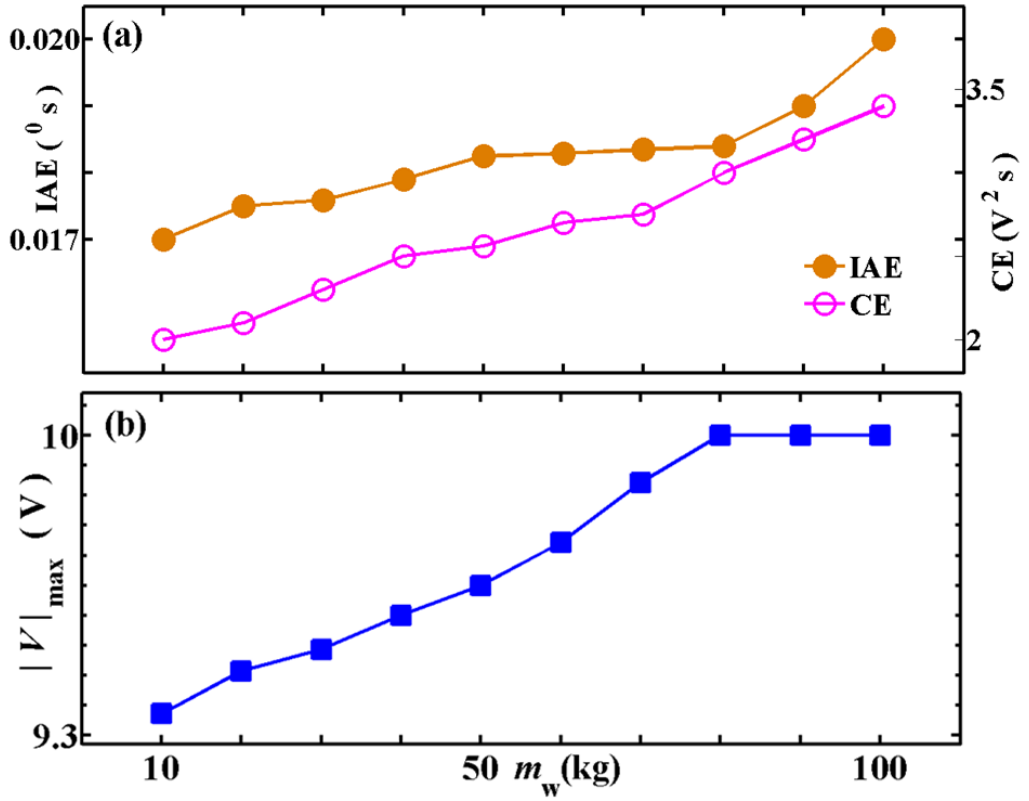

Figure 4.15: SMIC performances interms of IAE, CE (a) and $|V|_{max}$ (b) for different dead loads with 1^0 sinusoidal motions at 10Hz.

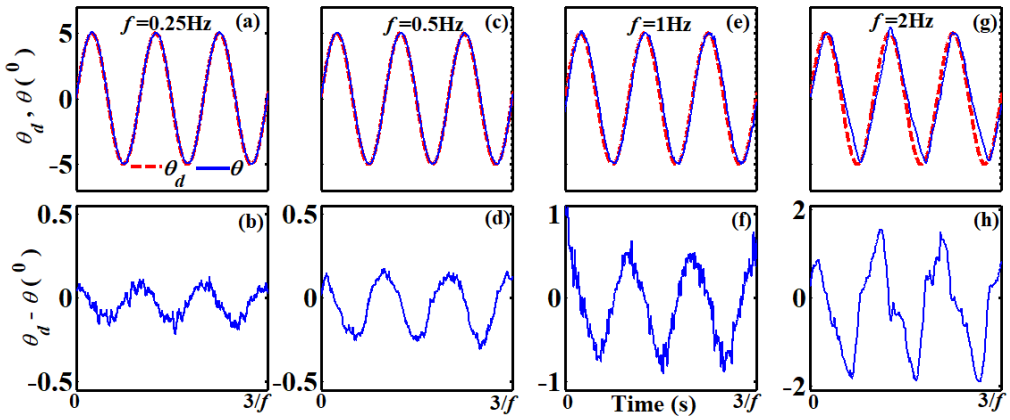

Figure 4.16: Different frequency demands and SMIC responses for 5^0 sinusoidal motions (a, c, e, g) with corresponding errors (b, d, f, h).

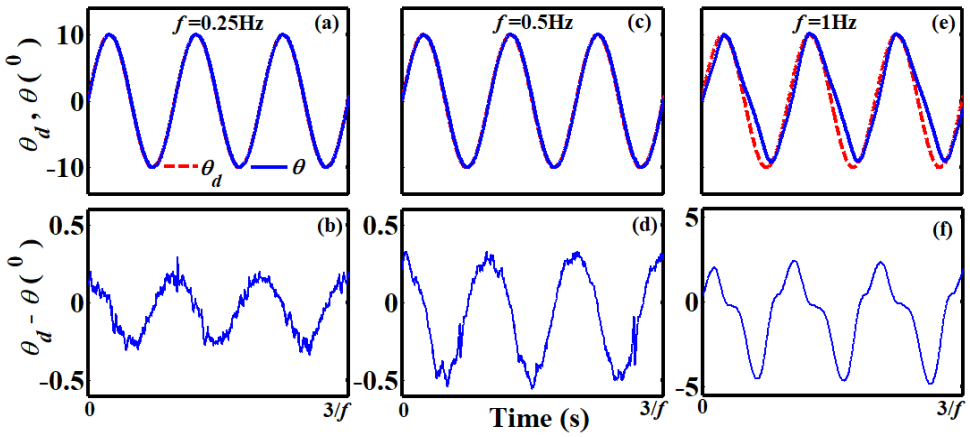

Figure 4.17: Different frequency demands and SMIC responses for 10^0 sinusoidal motions (a, c, e) with corresponding errors (b, d, f).

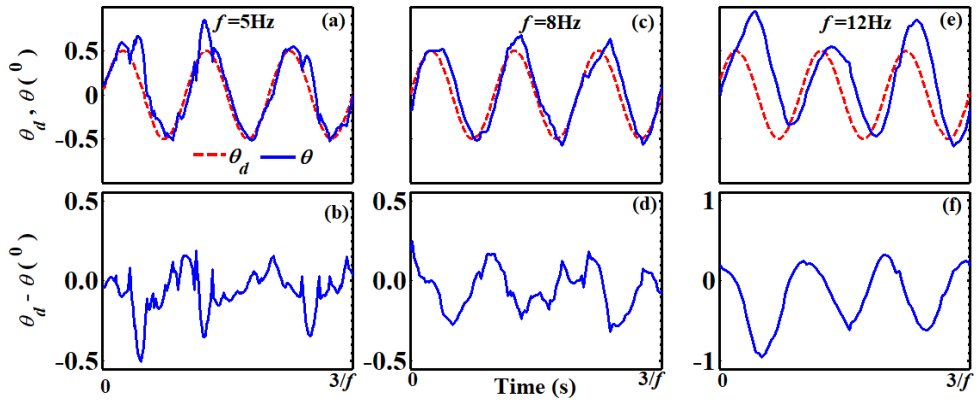

Figure 4.18: Different frequency demands and SMIC responses for 0.5^0 sinusoidal motions (a, c, e) with corresponding errors (b, d, f).

(II) ***Real time performances of SMIC with regulatory motion: step response***

SMIC responses to step demand for the target position θ_d from an initial link position θ_0 have been illustrated in Figs. 4.19 and 4.20 respectively for 14^0 and 28^0 steps. Results are shown for extension (a) and retraction (c) along with corresponding errors in (b, d). Figs. 4.19 and 4.20 reveal that the speed of the extension even for same amplitude to be faster than that of the retaction motion. This can be explained due to the high pressure acting on the larger cap-end area (4.6b) and smaller rod-end area (4.6c) during piston extension and retraction respectively. It is interesting to note that the similar study for the linear-motion EHAS presented in Figs. 3.22 and 3.23 revealed the domination of the external loading that was due to spring in that system. Though the angular-motion EHAS studied here does not have a spring, the effect of the dead load is expected to aid the retraction and oppose the extension. However, the

effect of area asymmetry on the pressure is seen to dominate over the opposite effect due to the deadload in this system.

The maximum piston velocity for extension and retraction can be extracted from Figs. 4.19 and 4.20 as $0.47ms^{-1}$ and $0.37ms^{-1}$ respectively. These velocities, as a result of flow bypass through the relief valve, are understandably lower than their respective velocity as $0.64ms^{-1}$ and $1.3ms^{-1}$ which are calculated from area-flow relations (1.3a-b) for 50lpm flow. These figures also show SMIC to resolve the chattering problem that could have been encountered during the prolonged zero error phase achieved corresponding to the constant demand phase, also referred as the regulatory demand phase. The observed error transients are clearly triggered at the instant of the step changeover in all the demands that should also be accompanied by transients in the control voltages. These transients impact both IAE and CE, shown in Table 4.3.

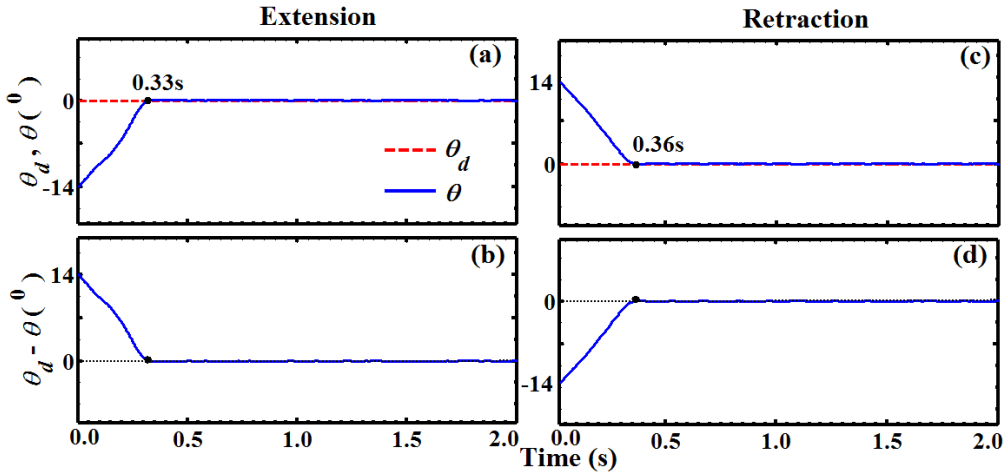

Figure 4.19: SMIC performances of 14^0 step responses for extension (a) and retraction (c) with their corresponding error (b) and (d).

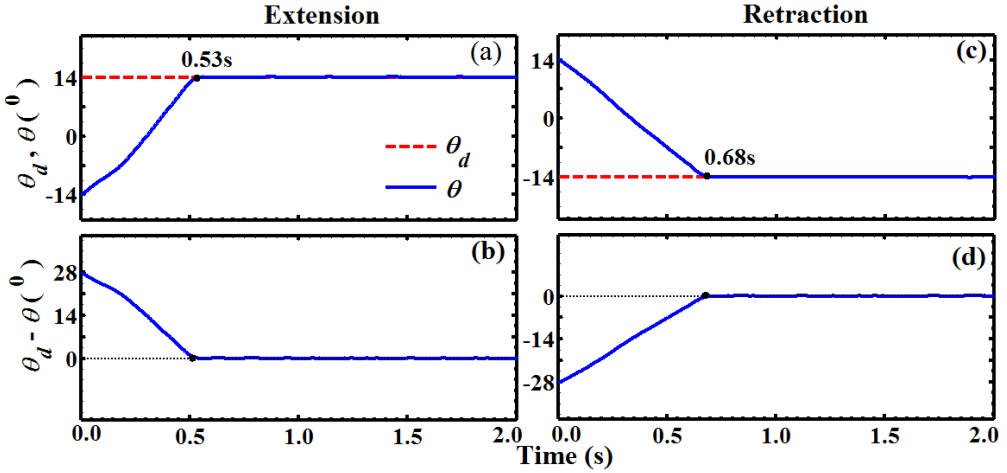

Figure 4.20: SMIC performances of 28^0 step responses for extension (a) and retraction (c) with their corresponding error (b) and (d).

Table 4.3: SMIC performances interms of Rise time, IAE and CE for 14^0 and 28^0 step responses of extension and retarction depicted in Figs. 4.19 and 4.20

Type of Motion	θ_0 (^{0})	Demand (^{0})	Rise Time (s)	IAE (^{0}-s)	CE (V^2 s)
Extension	-14	14	0.33	2.48	30.60
Retraction	14	14	0.36	2.60	34.15
Extension	-14	28	0.53	8.23	52.37
Retraction	14	28	0.68	9.68	66.85

(III) ***Real time performances of SMIC with combined motion of tracking and regulatory: saw- tooth response***

The saw-tooth demands for the angular-motion EHAS have been studied in Figs. 4.21 and 4.22. The corresponding demand has been defined as

$$\theta_d = \theta_0 + a(1 - \text{modulo}(2\pi f t, 2\pi)), \tag{4.14}$$

in terms of amplitude a , initial position θ_0 and frequency f in Hz for time t in s. Different frequency demands and SMIC responses for 1^0 amplitude of saw-tooth demand have been depicted in Fig. 4.21 with the corresponding responses (a, d, g), errors (b, e, h) and voltages (c, f, i). SMIC performances for 10^0 amplitude of saw-tooth demand have been depicted in Fig. 4.22.

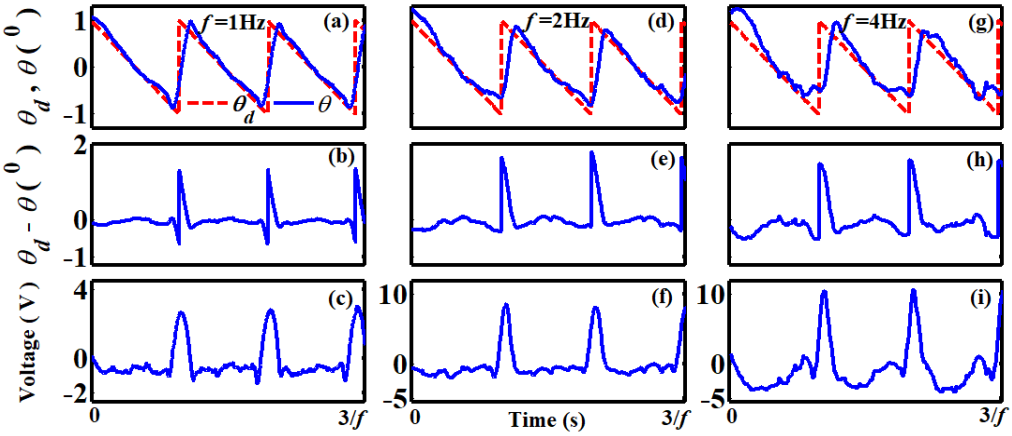

Figure 4.21: Different frequency demands and SMIC responses for 1^0 saw-tooth motions (a, d, g) with corresponding errors (b, e, h) and voltages (c, f, i).

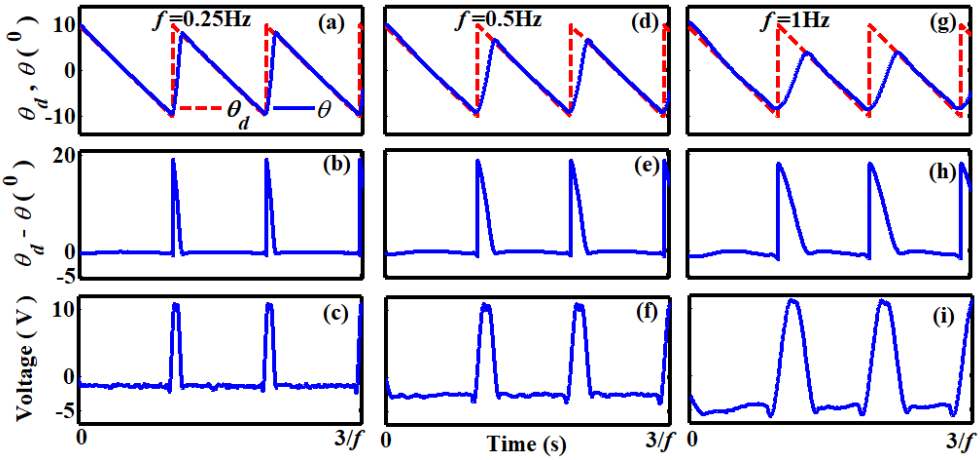

Figure 4.22: Different frequency demands and SMIC responses for 10^0 saw-tooth motions (a, d, g) with corresponding errors (b, e, h) and voltages (c, f, i).

The chattering effect has been eliminated in the regulatory zone of each saw-tooth motion in Figs. 4.21 and 4.22. The corresponding tracking error in Fig 4.21 and 4.22 is approximately zero in the tracking zone of constant velocity demand. These attributes prove the effectiveness of the controller through the real-time performance investigations for such nonlinear systems. The rise time for the step responses of saw-tooth motion shown in Figs. 4.21 and 4.22 have been found to increase also with the increase in frequency. Though there is a peak overshot in the step response of the saw-tooth motion for the linear- motion EHAS in Section 3.5.3, no overshoot has been observed for the angular- motion EHAS in Figs. 4.21 and 4.22. This could be due to effect of the compression spring for linear-motion EHAS. It is also observed from Figs. 4.22(d, g) that the step response of 10^0 saw-tooth motion could not be reached to its peak value beyond 0.25Hz. Of course, this is due to saturation of the control voltage driving the proportional valve solenoids.

(IV) ***Real time performances of SMIC with arbitrary type of motion***

The controller robustness has been studied in Figs. 4.23 to 4.25 involving aperiodic regulatory and tracking demand patterns. SMIC performance have been presented in Fig 4.23 in terms of link motion (a), piston motion (b), error in the piston motion (c) and corresponding adaptation of control paramaters (d). Points *m*, *n*, *o* and *p* in Fig. 4.23 correspond to activation of the adaptation of the control parameters due to error *e* growing beyond the layer $\pm e_\delta$ within which the adaptation remains suspended. Fig. 4.23(d) clearly shows that the adaptive laws and formulations have been successfully implemented for such response. Even for a composite demand in Fig. 4.24 involving

large step changes and changeover among step, sinusoidal, and triangular patterns of position demands, only the error spikes are apparent. Clearly, no chattering is observed even for such demand tracks. The controller is demonstrated as robust in Fig. 4.25 in terms of the response (a) and the error (b) for 1Hz sinusoidal demands of different amplitudes. The tracking error value in Fig. 4.25(b) is noticeably low even for 10^0 sinusoidal motion.

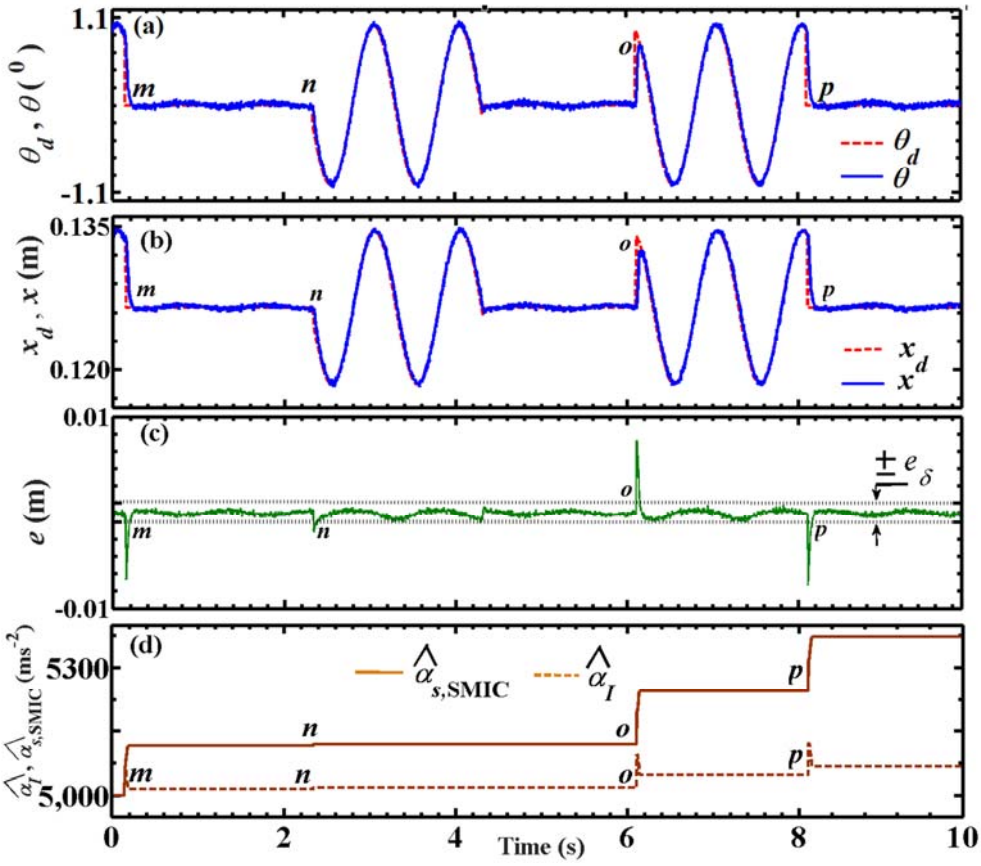

Figure 4.23: SMIC performance for arbitrary response with link motion (a), piston motion (b), error in piston motion (c) and corresponding adaptation of control paramaters (d).

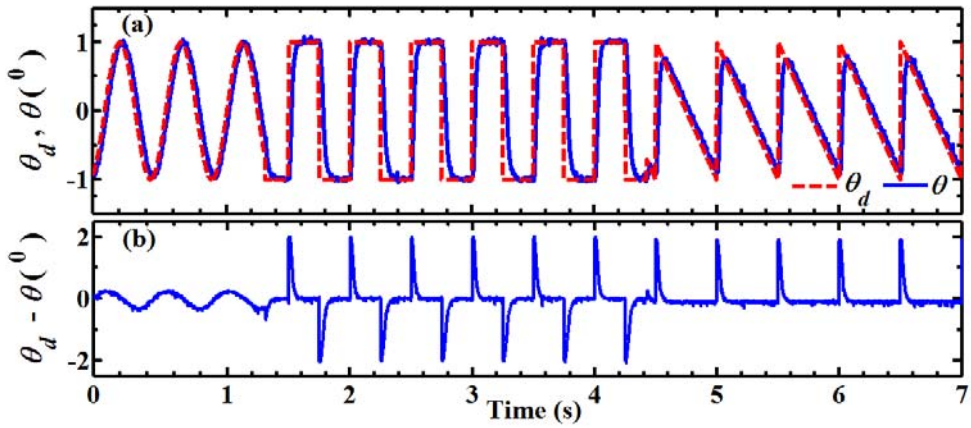

Figure 4.24: SMIC performances for the combined demand with 0.5Hz and 1^0 motion of different types of motions (a) and their corresponding error (b).

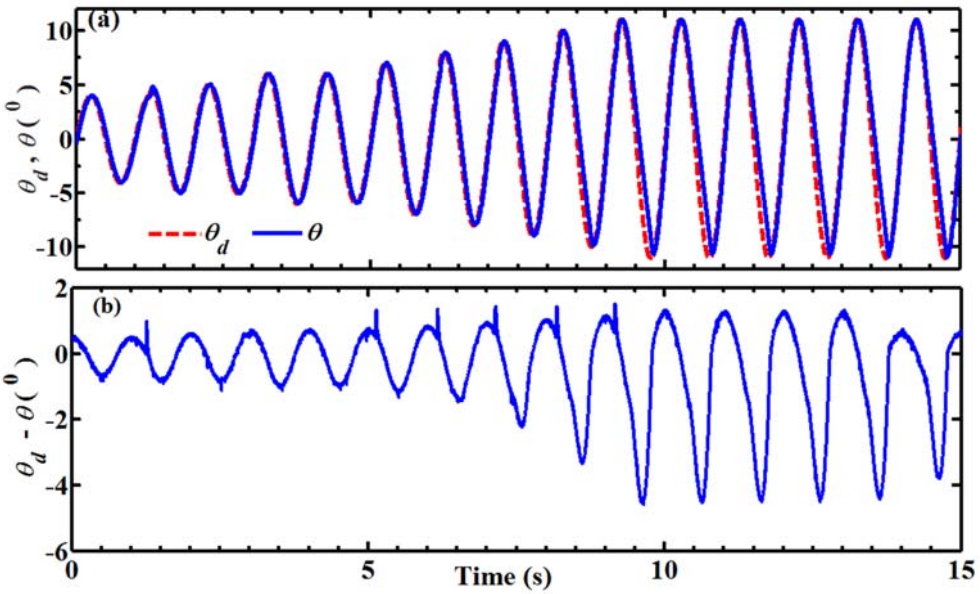

Figure 4.25: SMIC performances with 1Hz sinusoidal motions for different amplitude response (a) and their corresponding error (b).

4.6 Conclusion

This chapter deals with real-time motion tracking experiments in a laboratory-scale set up producing angular rotation of link driven by an electrohydraulic cylinder. Similar to the linear-motion EHAS, the proposed FSMC and SMIC have been implemented for ascertaining their performance. The corresponding mathematical modeling and input linearization techniques have been developed to extract the control voltage from the input of nonlinear SMC. The parameters have been identified through RCGA prior to the real-time experiments. SMIC has been verified to yield performance better than FSMC, Fuzzy-PI, SMC and IC. As concluded in the earlier chapter, the reasons for such good performance and robustness without chattering can

be attributed to combined outcome of low steady state error of IC, high disturbance rejection capability of SMC and suspended updating of SMC component in a small neighborhood of zero tracking or regulation error. Results have demonstrated aircraft-grade fast and high-precision tracking responses. High-amplitude-low-frequency tracking near the ground and low-amplitude-high-frequency tracking during high-altitude maneuvering are typical of aircraft flight control. The bandwidth of angular-motion EHAS for 1^0 sinusoidal motion has been determined to be about 10Hz which is more than that of linear-motion EHAS. This can be attributed to use of high-grade servo proportional valve and servo-cylinder pair for the angular-motion EHAS instead of industry-grade proportional valve and cylinder pair used in linear-motion EHAS.

CHAPTER 5: CONCLUSIONS AND FUTURE SCOPE

5.1 Conclusions

A detailed study on designing adaptive controllers has been accomplished here through simulation of representative dynamic systems and real-time experiments on corresponding laboratory-scale linear and angular-motion EHAS. For the proposed FSMC and SMIC, an adaptive formulation based on minimization of a Lyapunov functional involving projection operators constraining unbound growth of controller parameters has been shown to be convergent both theoretically and by a simulation example. SMIC performance has been found to be better than FSMC, Fuzzy-PI, SMC and IC for both the single degree-of-freedom systems. The benefits of lower steady-state error of IC and higher disturbance rejection capability of SMC together have yielded the lowest IAE and CE in case of SMIC. This controller has been shown to carry the trajectory close to zero of the sliding variable. In this region of near-zero error, chattering has been eliminated by not imposing the discontinuous SMC involving sign function. Resolving the problem of chattering that is usual with SMC is a notable contribution of this controller.

Prior experiments coupled with model-based optimization by RCGA have yielded the estimations of the controller and system parameters. The real-time results on a laboratory set up have demonstrated the designed SMIC to provide aircraft-grade fast and high-precision tracking responses. High-amplitude-low-frequency tracking near the ground and low-amplitude-high-frequency tracking during high-altitude maneuvering are typical of aircraft flight control. The bandwidth of the linear-motion EHAS with 0.02m sinusoidal response has been determined about 6 to 7Hz. The bandwidth of the angular-motion EHAS is 10Hz with 1^0 link motion. Of course, the higher bandwidth of the angular-motion EHAS can be attributed to the higher-grade servo proportional valve and servo-cylinder instead of a large deadband proportional valve and industry-grade cylinder in the liner-motion EHAS.

SMIC has been found to be very robust against complex demand forms for motion tracking despite strong nonlinear and uncertain features of friction in the cylinders, orifice pressure drops at the metered ports of the valves and valve deadband in the linear-motion EHAS. Experimental studies reveled clear evidence of stability and robustness of the proposed controller for both the systems. Experimental results show

the proposed scheme to have potential for high-speed applications so far kept outside the realm of low-cost electrohydraulic systems that could be designed with proportional valves.

5.2 Contributions

One of the main contributions of the work is the development of laboratory-scale EHAS producing linear and angular motions. Other major contribution is establishing the design methodology and real time implementation of the proposed FSMC and SMIC srructures. Establishing chattering-free SMIC response with near-zero tracking error is a significant achievement of this study. Use of optimizer for the identification of system parameters and the initial values of the controller parameters is also a ploy that was not used often in earlier EHAS research. Also, the use of projection operators for constraining the unbound growth of controller parameters adapted through Lyapunov function formulation was not often used for real-time systems. The simplest form of a quadratic form of the sliding function for the Lyapunov function has been chosen for the simplicity it offers towards obtaining the adaptation rules. Hence, the coeffcicients of the state variables involved in the definition of the sliding function has to be kept out of the ambit of adaptation. The Hurwitz form for these coefficients indeed emerges from the stability requirement of the sliding dynamics. However, their selection have been made through a systematic optimization study of minimizing the IAE defined in terms of responses obtained experimentally and through simulation study for the same variation of the excitation voltage. The form of sliding mode controller coupled with the proposed nonlinear integral controller is recommended for its robustness.

5.3 Scope of Future Studies

More rigorous validation of the proposed controller could be attempted in future with multiple cylinder arrangements in serial and parallel manipulators. Of course, a large number of joints in such systems are sources of much greater uncertainties. The aim should be to support more complex motion and loading patterns in such systems. Of course, higher potential for energy savings in pump-controlled system is another area of study involving design, system realization and real-time motion-control studies.

REFERENCES

Bartolini G, Pisano A, Punta E and Usai E (2003) A survey of applications of second-order sliding mode control to mechanical systems. *Int. J. Control* (76): 875-892.

Bessa WM, Dutra MS and Kreuzer E (2010) Sliding mode control with adaptive fuzzy dead-zone compensation of an electro-hydraulic servo-system. *J Intell Robot Syst* (58): 3-16.

Bosch Rexroth AG - Hydraulics Catalogue, 4/2 and 4/3 proportional directional valves direct operated, with electrical position feedback, without/with integrated electronics (OBE), 4WREE, RE 29061/10.05.

Bosch Rexroth AG - Hydraulics Catalogue, 4/4-way servo solenoid directional control valves, directly operated, with electrical position feedback and on-board electronics (OBE), 4WRPEH 6 , RE 29035/10.10.

Cetinkunt S, Pinsopon U, Chen C, Egelja A and Anwar S (2004) Positive flow control of closed-center electrohydraulic implement-by-wire systems for mobile equipment applications. *Mechatronics* (14): 403–420.

Chen Z, Yuan Y, Yuan X, Huang Y, Li X and Li W (2014) Application of multi-objective controller to optimal tuning of PID gains for a hydraulic turbine regulating system using adaptive grid particle swam optimization. *ISA Transactions* (56): 01–15.

Cheng Y, Ren G, Dai S (2004) The multi-body system modeling of the Gough–Stewart platform for vibration control. *Journal of Sound and Vibration* (271): 599–614.

Chern TL and Wu YC (1992) An optimal variable structure control with integral compensation for electrohydraulic position servo control system. *IEEE Trans. Industrial Electronics* (39): 460-463.

Daher N and Ivantysynova M (2015) Yaw stability control of articulated frame off-highway vehicles via displacement controlled steer-by-wire. *Control Engineering Practice* (45): 46–53.

Dasmahapatra S, Chaudhuri S, Mandal P, Mookherjee S and Saha R (2016) Fuzzy-PI control of motion tracking by an electrohydraulic system with multiple nonlinearities. In: *Michael Faraday IET International Summit*, Kolkata, India, Sept. 12–13, 2015, pp. 89-92.

Ding S, Wang J and Zheng WX (2015) Second-Order Sliding Mode Control for Nonlinear Uncertain Systems Bounded by Positive Functions. *IEEE Trans. Ind. Electronics* (62): 5899-5909.

Eryilmaz B and Wilson BH (2006) Unified modeling and analysis of a proportional valve. *J Franklin Institute* (343): 48–68.

Eshelman LJ and Schaffer JD (1993) Real coded genetic algorithms and interval schemata. *Foundation of Genetic Algorithms* (2): 187–202.

Feng Y, Yu XH and Han FL (2013) High-order terminal sliding-mode observer for parameter estimation of a permanent-magnet synchronous motor. *IEEE Trans. Ind. Electronics* (60): 4272-4280.

Ha QP, Nguyen QH, Rye DC and Durrant-White HF (2001) Fuzzy sliding mode controller with applications. *IEEE Trans. on Industrial Electronics* (48): 38-46.

Herrera F, Lozano M and Verdegay J. L (1998) Tackling real coded genetic algorithms: operators and tools for behavioural analysis. *Artificial Intelligence Review* (12): 265–319.

Herreros A, Baeyens E and Peran JR (2002) Design of PID-type controllers using multiobjective genetic algorithm. *ISA Transactions* (41): 457–472.

Hu C, Yao B and Wang Q (2011) Adaptive robust precision motion control of systems with unknown input dead-zones: a case study with comparative experiments. *IEEE Trans. Ind. Electronics* (58): 2454-2464.

Huayong Y, Hu S, Guofang G and Guoliang H (2009) Electro-hydraulic proportional control of thrust system for shield tunneling machine. *Automation in Construction* (18): 950–956.

Hwang CL (1996) Sliding mode control using time-varying switching gain and boundary layer for electro-hydraulic position and differential pressure control. *IEE Proceedings Control Theory Applications* (143): 325-332.

Karaboga D and Basturk B (2007) A powerful and efficient algorithm for numerical function optimization: artificial bee colony (ABC) algorithm. *Journal of Global Optimization* (39): 459–471.

Kemmetmuller W, Muller S and Kugi A (2007) Mathematical Modeling and Nonlinear Controller Design for a Novel Electrohydraulic Power-Steering System. *IEEE/ASME Trans. on Mechatronics* (12): 85-97.

Laghrouche S, Liu J, Ahmed F, Harmouche M and Wack M (2015) Adaptive second-order sliding mode observer-based fault reconstruction for PEM fuel cell air-feed system. *IEEE Trans. Control Syst. Technology* (23): 1089-1109.

Lazic DV and Ristanovic MR (2007) Electrohydraulic thrust vector control of twin rocket engines with position feedback via angular transducers. *Control Engineering Practice* (15): 583-594.

Lee J, Yoo C, Park YS, Park B, Lee SJ, Gweon DG and Chang PH (2012) An experimental study on time delay control of actuation system of tilt rotor unmanned aerial vehicle. *Mechatronics* (22): 184-194.

Levant A (1993) Sliding order and sliding accuracy in sliding mode control. *Int. J. Control* (580): 1247-1263.

Levant A (2005) Homogeneity approach to high-order sliding mode design. *Automatica* (41): 823–830.

Levant A (2007) Principles of 2-sliding mode design. *Automatica* (43): 576-586.

Lin CL, Jan HY, and Shieh NC (2003) GA-based multi objective PID control for a linear brushless DC motor. *IEEE/ASME Trans. Mechatronics* (8): 56–65.

Loukianov AG, Rivera J, Orlov YV and Teraoka EYM (2009) Robust trajectory tracking for an electrohydraulic actuator. *IEEE Trans. Industrial Electronics* (56): 3523-3531.

Mandal P, Sarkar BK, Saha R, Mookherjee S, Acharyya SK and Sanyal D (2015a) GA-optimized fuzzy-feedforward-bias control of motion by a rugged electrohydraulic system. *IEEE/ASME Trans. Mechatronics* (20): 1734-1742.

Mandal P, Sarkar BK, Saha R, Chatterjee A, Mookherjee S, and Sanyal D (2015b) Real-time fuzzy-feedforward controller design by bacterial foraging optimization for an electrohydraulic system. *Engineering Applications of Artificial Intelligence* (45): 168-179.

Mandal P, Sarkar BK, Saha R, Mookherjee S, Chatterjee A and Sanyal D (2016) Lessons learned from using some bio-inspired optimizers for real-time controller design for a low cost electrohydraulic system. *Applied Soft Computing* (48): 638-649.

Merritt HE (1967) *Hydraulic Control Systems*. Wiley.

Michalewicz Z (1992) *Genetic Algorithms + Data Structures = Evolution Programs*. New York: Springer Verlag.

Passino KM (2002) Biomimicry of bacterial foraging for distributed optimization and control. *IEEE Control System Magazine* (22): 52-67.

Precup R, David R, Petriu EM, Radac M and Preitl S (2014) Adaptive GSA-based optimal tuning of PI controlled servo systems with reduced process parametric sensitivity, robust stability and controller robustness. *IEEE Trans. on Cybernetics* (44): 1997–2009.

Qiu H, Zhang Q and Reid JF (2001) Fuzzy control of electrohydraulic steering systems for agricultural vehicles. *Trans. ASAE* (44): 1397-1402.

Rahmat MF, Zulfatman, Husain AR, Ishaque K, Sam YM, Ghazali R and MdRozali S (2011) Modeling and controller design of an industrial hydraulic actuator system in the presence of friction and internal leakage. *International Journal of Physical Sciences* (6): 3502-3517.

Sarkar BK, Das J, Saha R, Mookherjee S and Sanyal D (2013a) Approaching servoclass tracking performance by a proportional valve-controlled system. *IEEE/ASME Trans. on Mechatronics* (18): 1425–1430.

Sarkar BK, Mandal P, Saha R, Mookherjee S and Sanyal D (2013b) GA-optimized feedforward-PID tracking control for a rugged electrohydraulic system design. *ISA Transactions* (52): 853-861.

Savaresi SM, Taroni FL, Previdi F and Bittanti S (2004) Control system design on a power-split CVT for high-power agricultural tractors. *IEEE/ASME Trans. on Mechatronics* (9): 569-579.

Shahnazi R, Shanechi HM and Pariz N (2008) Position control of induction and DC servomotors: A novel adaptive fuzzy PI sliding mode control. *IEEE Trans. Energy Conversion* (23): 138–147.

Song X, Wu C and Sun Z (2012) Design modeling and control of a novel automotive transmission clutch actuation system. *IEEE/ASME Trans. on Mechatronics* (17): 582-587.

Su YX, Duan BY (2000) The application of the Stewart platform in large spherical radio telescopes. *J Robotic Systems* (17): 375–383.

Su CY, Stepanenko Y, Svoboda J and Leung TP (2000) Robust adaptive control of a class of nonlinear systemswith unknown backlash-like hysteresis. *IEEE Trans. Automatic Control* (45): 2427-32.

Truong DQ and Ahn KK (2011) Force control for press machines using an online smart tuning fuzzy PID based on a robust extended Kalman filter. *Expert Systems with Applications* (38): 5879–5894.

Wang YJ (2010) Characterization and quenching of friction-induced limit cycles of electro-hydraulic servovalve control systems with transport delay. *ISA Transactions* (49): 489-500.

Wang S, Habibi S and Burton R (2008) Sliding mode control for an electrohydraulic actuator system with discontinuous non-linear friction. *Proc.IMechE Part I: Journal of Systems and Control Engineering* (222): 799-815.

Wang F, Liang C, Tian Y, Zhao X and Zhang D (2016) Design and control of a compliant microgripper with a large amplification ratio for high-speed micro manipulation. *IEEE/ASME Trans. Mechatronics* (21): 1261-1271.

Watton J (2009) *Fundamentals of Fluid Power Control*. New York: Cambridge University Press.

Xu Q (2017) Precision motion control of piezoelectric nanopositioning stage with chattering-free adaptive sliding mode control. *IEEE Trans. Automation Sc. and Engineering* (14): 238-248.

Yang J, Li SH and Yu XH (2014) Sliding-mode control for systems with mismatched uncertainties via a disturbance observer. *IEEE Trans. Ind. Electronics* (60): 160-169.

Yao L and Wen H (2013) Design of observer based adaptive PID controller for nonlinear systems. *Int J Innovative Computing, Information Control* (9): 667-677.

Zadeh LA (1965) Fuzzy Sets. *Information and Control* (8): 338-353.

Zhang D (2010) Parallel robotic machine tools. *Springer Science+Business Media LLC*.

Zhao ZY, Tomizuka M, and Isaka S (1993) Fuzzy gain scheduling of PID controllers. *IEEE Transactions on Systems, Man, and Cybernetics* (23): 1392 – 1398.

Zhen Z, Jiang J, Wang X and Gao C (2015) Information fusion based optimal control for large civil aircraft system. *ISA Transactions* (55): 81-91.